THÈSE

Pour obtenir le grade de

DOCTEUR DE L'UNIVERSITÉ GRENOBLE ALPES

École doctorale : PHYS - Physique
Spécialité : Physique Théorique
Unité de recherche : PHotonique, ELectronique et Ingéniérie QuantiqueS

Vers des bits quantiques volants dans l'effet Hall quantique: une étude théorique

Towards flying quantum bits within the quantum Hall regime: a theoretical study

Présentée par :

Prasoon KUMAR

Direction de thèse :

Xavier WAINTAL DIRECTEUR DE RECHERCHE, CEA CENTRE DE GRENOBLE	Directeur de thèse
Kyrylo SNIZHKO INGENIEUR DOCTEUR, CEA CENTRE DE GRENOBLE	Co-encadrant de thèse

Rapporteurs :

Christophe MORA
PROFESSEUR DES UNIVERSITES, UNIVERSITÉ PARIS DIDEROT
François PARMENTIER
CHARGE DE RECHERCHE HDR, LABORATOIRE DE PHYSIQUE DE L'ENS

Thèse soutenue publiquement le **12 décembre 2025**, devant le jury composé de :

Christophe MORA, PROFESSEUR DES UNIVERSITES, UNIVERSITÉ PARIS DIDEROT	Rapporteur
François PARMENTIER, CHARGE DE RECHERCHE HDR, LABORATOIRE DE PHYSIQUE DE L'ENS	Rapporteur
Mair CHSHIEV, PROFESSEUR DES UNIVERSITES, UNIVERSITÉ GRENOBLE ALPES	Président
Christopher BÄUERLE, DIRECTEUR DE RECHERCHE, CNRS DELEGATION ALPES	Examinateur
Michał HORODECKI, FULL PROFESSOR, UNIVERSITY OF GDAŃSK	Examinateur
Janine SPLETTSTÖSSER, FULL PROFESSOR, CHALMERS UNIVERSITY OF TECHNOLOGY	Examinatrice

Contents

I INTRODUCTION

1 QUANTUM HALL EFFECT 11
- 1.1 Foundations 11
- 1.2 Landau levels 13
- 1.3 Landau level calculations 14
  - 1.3.1 Landau gauge 15
  - 1.3.2 Symmetric gauge 16
  - 1.3.3 Landau levels – gauge-independent calculations 16
  - 1.3.4 Relevant energy scales 18
    - 1.3.4.1 Energy level in quantum well 18
    - 1.3.4.2 Cyclotron gap 18
    - 1.3.4.3 Coulomb interaction 18
- 1.4 Fractional quantum Hall effect 19
  - 1.4.1 Laughlin wavefunction 20
  - 1.4.2 Composite fermions 21
- 1.5 Topology in quantum Hall effect 23
- 1.6 Overview of concepts covered 25

2 INTRODUCTION TO DEVICES AND PROBES 26
- 2.1 2D gas heterostructures 26
- 2.2 Quantum point contacts 27
- 2.3 Mach-Zehnder interferometer 29
- 2.4 Short pulses experiments 31
- 2.5 Overview of concepts covered 32

3 THEORETICAL AND NUMERICAL METHODS 34
- 3.1 Brief: Scattering formalism 34
  - 3.1.1 Introduction 34
  - 3.1.2 Scattering matrix 34
  - 3.1.3 Generalized relations for transport quantities 35
    - 3.1.3.1 Landauer formula 38
    - 3.1.3.2 Current noise 39
    - 3.1.3.3 Fano factor 41
  - 3.1.4 Illustration: Rectangular barrier potential 41
- 3.2 Numerical tools 43

II MODELLING OF A QUANTUM POINT CONTACT

4 QUANTUM HALL EDGE MODES: KWANT 46
- 4.1 Closed sample 47
- 4.2 Open sample 47

5 MODELS 49
- 5.1 Analytical models of QPC 51

5.1.1 Point model 52
5.1.2 Wide model 53
5.1.3 Long model 55
5.2 Point-QPC limit 57
5.3 Model predictions 58
5.3.1 Model comparison with realistic parameters 58
5.3.2 Transport predictions 60
5.3.2.1 Typical experimental regime 61
5.3.2.2 High voltages 64
5.4 Conclusion 64
6 NUMERICAL INVESTIGATION 65
6.1 Transmission function 66
6.2 Transmission function: Key takeaways 68
6.3 Velocity analysis 69
6.3.1 Edge velocity: Comparison between band and cut 70
6.4 Velocity analysis: Key takeaways 71
6.5 LDOS analysis 71
6.6 LDOS analysis: Key takeaways 72
6.7 Conclusion 72
III EFFECT OF INTERACTION IN ELECTRONIC INTERFEROMETERS
7 INTRODUCTION 77
7.1 Setting the tone 77
7.2 Review of the non-interacting theory 78
7.2.1 Voltage pulse excitation 80
7.2.2 Dynamic interference 81
7.3 Outlook 82
8 MODEL AND TECHNIQUES 84
8.1 Microscopic model 84
8.1.1 Model with mean-field interaction: 85
8.1.2 Numerical technique: Self-consistent TKWANT 87
8.2 Current conservation and gauge invariance 87
8.3 Simulation parameters 89
8.4 Conclusion 90
9 CHARACTERIZATION OF INTERFEROMETER SUB-COMPONENTS 91
9.1 1D wire 91
9.1.1 DC characterization 91
9.1.2 Sending pulses in 1D wire 93
9.1.2.1 Adiabatic switching of interaction 93
9.1.2.2 Interaction induced re-normalization of velocity 95
9.2 QPC 96
9.2.1 DC characterization 97
9.2.2 Sending pulses on a QPC 98
9.3 Conclusion 99
10 SIMULATIONS OF THE FULL INTERFEROMETER 100
10.1 DC characterization 100
10.2 Interferometric pulses 101

10.2.1 Adiabatic switching of interaction 102
10.2.2 Interaction induced effects 103
10.3 Conclusion 104

IV CONCLUSION AND PERSPECTIVES

V APPENDICES

A SCATTERING MATRIX COEFFICIENTS IN TERMS OF TRANSMISSION FUNCTION 109

B TRANSMISSION FUNCTION FOR POINT QPC 110

C TRANSMISSION FUNCTION FOR WIDE QPC 113

D POINT LIMIT OF TRANSMISSION FUNCTION IN CONVENTIONAL QUANTUM MECHANICS 117

E THE ROLE OF EDGE VELOCITY 119

F NOISE CALCULATIONS FOR FOUR-TERMINAL DEVICE 121

G DC MACH-ZEHNDER INTERFEROMETER 124

VI BIBLIOGRAPHY

BIBLIOGRAPHY 127

Acknowledgement

I would like to begin by expressing my sincere gratitude to the members of my thesis committee: Christopher Mora, François Parmentier, Mair Chshiev, Christopher Bäuerle, Janine Splettstoesser, and Michał Horodecki. I am deeply thankful for the time, attention, and intellectual generosity they have devoted to reading and evaluating this work.

I am especially indebted to my supervisors, Xavier Waintal and Kyrylo Snizhko. Their guidance, patience, and trust have shaped not only this thesis but also the way I think about science. I owe them far more than can be expressed in words. Their constant encouragement, good humor, and unwavering support taught me how to approach difficult problems with patience and perspective. If I can carry forward even a fraction of what they have taught me, I will consider myself incredibly fortunate. I feel truly privileged to have worked under their supervision; this thesis would not have been possible without them by any stretch of the imagination.

In a sense, the story of this thesis began long before I wrote its first line. Nearly twenty-five years ago, my father was himself writing his thesis. Around that same time, I had just been born. By the time he completed the preface and mentioned my name in it, I was already two years old. I carry a faint but enduring memory of those days: my father sitting quietly for hours, absorbed in writing. As a child I could not comprehend what that meant. Only now, while writing my own thesis, do I begin to understand the patience, solitude, and perseverance that such a task demands.

The feeling I experienced then watching him with a mixture of wonder and curiosity — finds its closest expression in the words of Tagore [Tagore]. With time, however, admiration was enveloped by a deeper realization: how difficult those years must have been for both my parents. In the midst of uncertainties and struggles, they continued to build a life while raising a child who understood none of those burdens.

Today, as this journey reaches its conclusion, I dedicate this thesis to them. It is a small tribute to the sacrifices they made and the quiet strength with which they carried them. Whatever little I have been able to accomplish rests upon the foundation they built with patience, care, and love.

In a way, the story continues. My brother, Priyanshu Kumar Pant, is now pursuing his own PhD. Although, he is younger than me, I have often learned a great deal from him than the other way around. I wish him every success in his research.

Research is often imagined as a solitary endeavor, yet in truth it unfolds within a community. I have been fortunate to share these years with wonderful office mates: Thomas Bernet, Matthieu Jeannin, Miha Srdinsek, Adrien Moulinas, and Anas-El-Mendili and Surajit Sarkar. Anas and Adrien deserve special thanks for the many lively conversations, mathematical puzzles, and the ever-present chocolate counter that brightened long days. Such exchanges often reminded me that the joy of science lies as much in questioning as in answering.

I am equally thankful for the presence of friends who accompanied me along this path. Aditya Gaur and Abhishek Sharma have always shown a genuine concern for my progress

and well-being. I thank Pradeep Purohit for answering my calls even at the most unlikely hours. Pulkit Agroiya reminds me of the beauty of dedication. Lukas Cvitkovich has shown the art of composure can endure even the most difficult circumstances during his stay in Grenoble (especially with the lost car key incident). Esteban Rodríguez has always insisted on how one should never lose one's sense of joy. Camille Lassalle has been a constant reminder to remain curious and to keep trying something new. All of that is close to me.

Finally, there is someone special without whom this acknowledgement would feel incomplete. During all those uncountable moments when I felt lost, exhausted, or uncertain of myself, she stood firmly by my side. Across distance and time differences, her patience, understanding, and unwavering support never faltered. In moments when motivation faded and doubt grew louder than reason, she offered encouragement, warmth, and perspective.

Thank you, Jayanti Rawat, for being such a blessing to me, and for all the countless ways in which you contributed to carrying me through this journey. Your presence has been a source of light during my most difficult days.

A thesis may bear a single author's name, but it is never the work of one person alone. It is shaped by the care, generosity, and companionship of many people whose influence runs quietly through its pages. Today, as I write these final lines, I realize that this work too carries the imprint of many lives and many kindnesses. I dedicate it with gratitude to all those who walked this path with me.

Thesis in a Nutshell

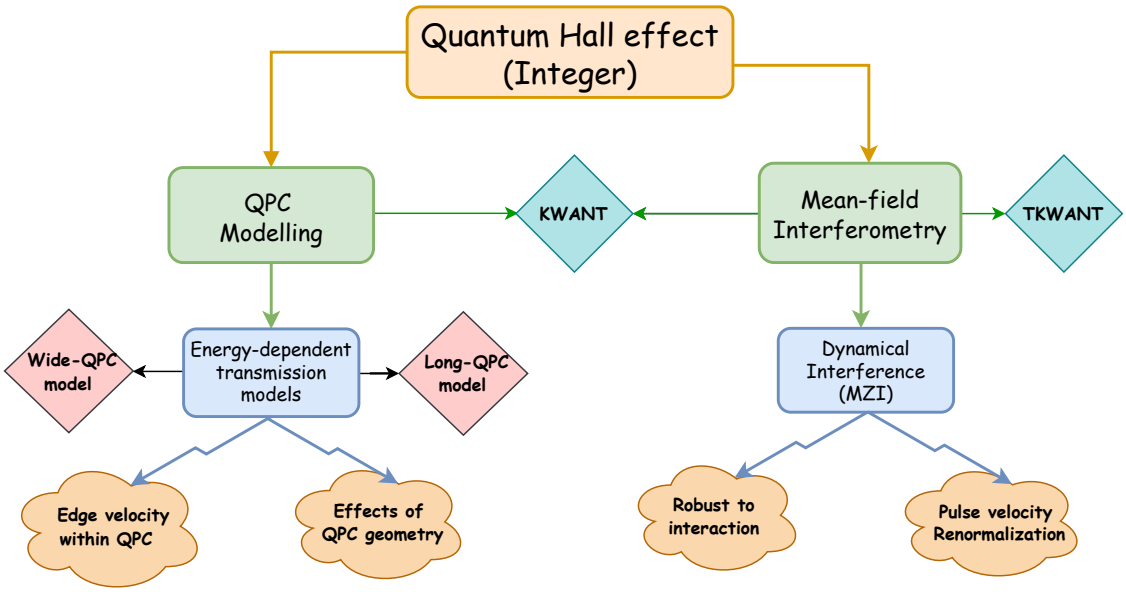

The quantum Hall (QH) effect is among the most remarkable and extensively studied phenomena in condensed matter physics. It has served as a platform for exploring a variety of exotic effects, such as the quantization of conductance arising from the formation of chiral edge channels. These edge channels remain central to both theoretical and experimental investigations of quantum Hall physics.

A significant fraction of quantum Hall experiments involves tunnelling contacts, known as quantum point contacts (QPCs), where quasiparticles can transfer between different edges. QPCs are essential tools for probing the physics of edge excitations, and they have enabled the experimental verification of predictions such as fractional quasiparticle charges. However, experiments with a single QPC often show discrepancies with theoretical predictions. While theory and experiment agree at small bias voltages, noticeable deviations appear at higher biases—specifically when the bias exceeds the system temperature but remains below the bulk energy gap. These discrepancies manifest both in the integer and, more prominently, in the fractional quantum Hall regimes.

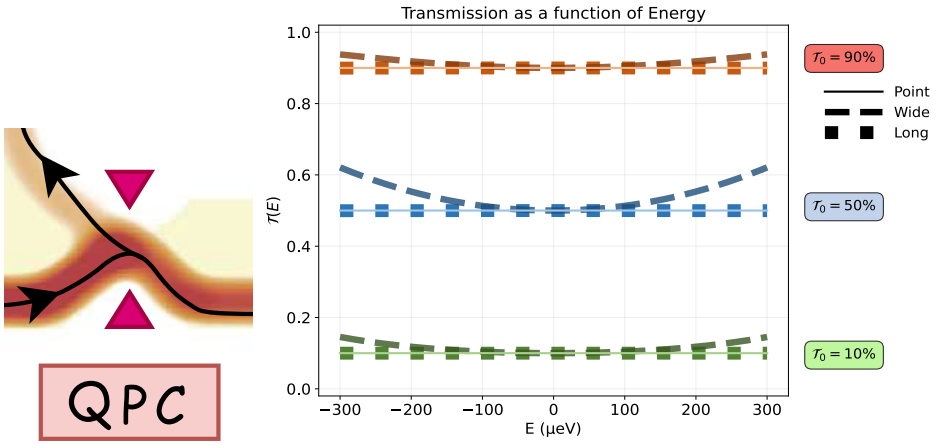

Figure 1: **Left panel:** Illustration of a single QPC. **Right panel:** Transmission $\mathcal{T}(E)$ for various models for experimentally realistic parameters. Comparison of the dependence of QPC transmission on energy that point-, wide-, and long-QPC models predict for realistic experimental parameters. The effects of the long-QPC model are negligible in the experimentally relevant regime. Whereas the width of the QPC does have a noticeable effect.

In the first part of the project, we focus on addressing this discrepancy in the integer quantum Hall regime. One potential explanation is the energy dependence of the tunnelling amplitude, an effect absent in conventional models. In this work, we focus on the integer quantum Hall regime and introduce two models that account for the spatial extension of QPCs. The wide-QPC model incorporates the finite distance over which edges interact, while the long-QPC model considers the tunneling amplitude arising from a finite bulk gap and separation between edges.

Our analysis shows a significant variation in the transmission function (see Fig. 1): the wide-QPC model exhibits the strongest, whereas the long-QPC model shows weaker variation. However, within the conventional experimental parameter range, these differences do not manifest significantly in the observable transport quantities (see Fig. 3).

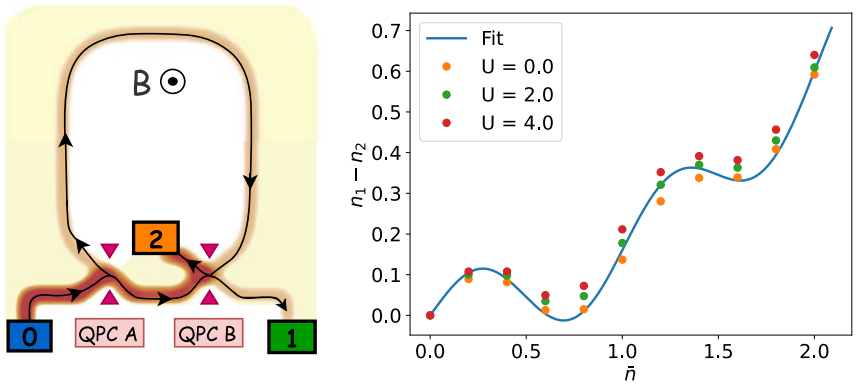

Figure 2: **Left panel:** Illustration of a Mach-Zehnder interferometer device. **Right panel**: Transmitted charge difference $(n_1 - n_2)$ plotted as a function of total injected charge $\bar{n}$ in the presence of different strength of mean-field interaction U.

In the second part of the thesis, we investigate ultrafast pulses in interferometers in the terahertz regime. Electronic interferometers have been identified as potential platforms for realizing flying qubits, where pulses shorter than the device's time of flight are required. Understanding the resulting dynamics necessitates accounting for electron-electron interactions. We perform time-resolved simulations of a Mach-Zehnder interferometer using a time-dependent mean-field treatment of interactions.

Our analysis shows that the interference phenomenon remains remarkably robust against mean-field interactions. This robustness is reflected in the oscillations observed in the transmitted charge as a function of the injected charge $\bar{n}$, (see Fig. 2). Overall, our results indicate that electron–electron interactions primarily lead to a renormalization of the pulse velocity, while the interference pattern itself remains largely unaffected—highlighting the persistence of quantum coherence even under interacting conditions.

Although these two investigations address distinct systems, they collectively advance our understanding of quantum transport in mesoscopic systems. The insights gained here provide a foundation for the development of next-generation quantum devices.

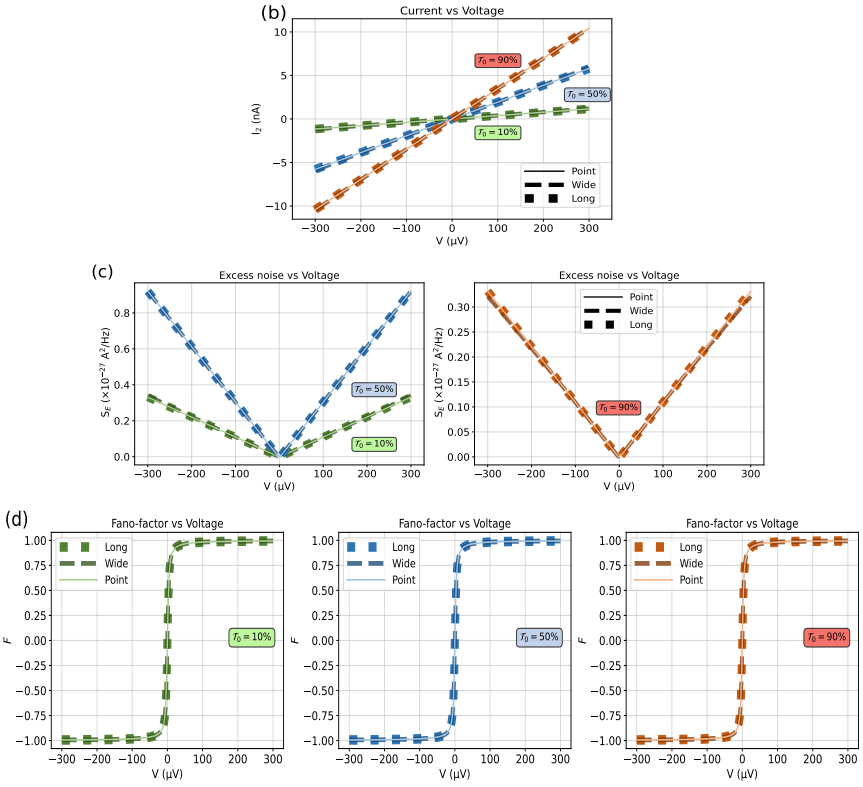

Figure 3: Transport observables for different QPC models for experimentally realistic parameters. (a) Comparison of the current dependence on the applied bias voltage for point, wide and long QPC model. All the models prediction lie on top of each other with no significant variation. (b) Comparison of the shot dependence on the applied bias voltage for point, wide and long QPC model. The long-model show no variation as the probed energy scale is significantly smaller than the tunneling amplitude (Δ). While the wide-model show increment and suppression of noise for strong and weak tunneling. (c) Comparison of the Fano factor for three models at $\mathcal{T}_0 = 10\%$. No significant variation has been observed in the transport quantities away from the point QPC scenario.

Part I

INTRODUCTION

1

Quantum Hall Effect

"Nothing in life is to be feared, it is only to be understood. Now is the time to understand more, so that we may fear less."

Marie Curie

1.1 Foundations

Throughout human history, there has been a persistent fascination for understanding the natural world. This curiosity has been central to human civilization, particularly in the exploration to the fundamental laws of physics. The idea was not only to discover the mechanism behind the workings but rather to come up with the minimum number of laws that spans the wide variety of observed phenomena. This was a leading essence behind reductionism, a philosophical approach that seeks to understand complex phenomena by breaking them down into simpler, fundamental components. However, the universe composed of discrete elements, eventually presents exceptions that prove more intriguing than the rules themselves.

Condensed matter systems are conventional examples that demonstrate the limitations of reductionism. For these systems, which consist of periodically arranged atoms bonded together to form crystals with vast numbers of itinerant electrons, it is possible to formulate a microscopically accurate Hamiltonian. One might even dream of solving the equations of motion for electrons in a crystal. However, the sheer scale and complexity of the problem make this impractical. In other words, the vast number of resulting equations makes it difficult to construct phenomena from microscopic fundamentals.

To overcome such challenges, researchers often abandon the reductionism in favor of emergence, a principle that truncate the hierarchy and search for new organizational principles within (and emerging from) a more complex level, often without reference to fundamental constituents. Robert Laughlin, in his book *A Different Universe*, argued that applying the fundamental equations of quantum mechanics to any system with more than 100 particles results in a problem that can only be solved with an unimaginably powerful computer (i.e., it is practically unsolvable). Based on this reasoning, he argued that higher levels of organization cannot be fully explained by simply analyzing their lower-level components; rather, higher-order, emergent principles are essential for understanding the natural world. The phrase “more is different” succinctly captures this idea [Anderson, 1972] .

This concept has gained increasing prominence in condensed matter physics. One of the most remarkable demonstrations of emergence in this field is the quantum Hall (QH) effect. In this phenomenon, a two-dimensional electron gas (2DEG) subjected to strong magnetic fields and low temperatures exhibits an exotic, quantized state of matter known as the quantum Hall effect. The 2DEG at a high magnetic field is a marvelous playground to study interaction effects in electron liquids. The physical properties of 2DEG under such a high magnetic field lead to a limit where Landau level mixing due to disorder or electron-electron interaction may be considered as a weak perturbation. Qualitatively, physical properties then depend only on the ratio of the disorder potential to electron-electron interaction potential. Such a limit is referred to as the **Quantum Hall regime**. Under such a regime, both disorder and interaction needed to be addressed using non-perturbative approaches. The limit where the disorder potential is stronger generates an *integer* quantum Hall regime, whereas the limit where the interaction potential is stronger generates a *fractional* quantum Hall regime.

Below we define the setup of the hall bar and Hall conductivity:

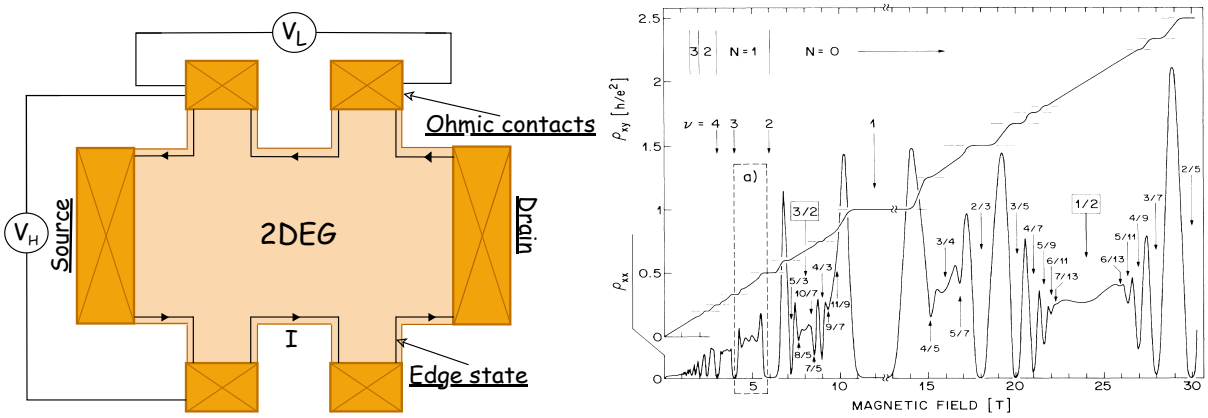

(a) (b)

Figure 1.1: (a) Hall bar. (b) Entire landscape of Quantum Hall states. Figure adapted from Willett et al.[Willett et al., 1987].

QHE display incredibly accurate quantization of the Hall conductance for 2DEG at integral and special fractional multiples of $\frac{e^2}{h} = \frac{1}{25{,}812.807572\,\Omega}$, regarded as one of the most remarkable discoveries of 20th century. The experimental data reported by [Willett et al., 1987] is shown in Fig. 1.1. Each fraction of the form p/q refer a fractional Hall state. Until so far, more than 70 different FQH states have been observed.

The discovery led to two Nobel Prizes: one awarded to Klaus von Klitzing in 1985 for the integer quantum Hall effect, and another to Robert B. Laughlin, Horst L. Störmer, and Daniel C. Tsui in 1998 for the fractional quantum Hall effect. Furthermore, a third recognition came in 2016, when the Nobel Prize was awarded to David J. Thouless, F. Duncan M. Haldane, and J. Michael Kosterlitz for establishing the theoretical foundations of the topological classification of matter.

1.2 Landau levels

The fundamental reason for the rich behavior advertised above is the *quenching* of the kinetic energy at high magnetic field. This effect occurs in both classical as well as in quantum version of Hall effect.

In classical mechanics, a magnetic field $\vec{B}$ dictates electrons to move on a circular orbit at the cyclotron frequency:

$$\omega_c = \frac{eB}{m^*}, \tag{1}$$

where, m^* is the electron's effective band mass ($m^* = 0.067m_e$ in GaAs). The center of the circular orbit "drift" in accordance to the additional forces due to external potentials, interactions with other electrons etc., with a velocity $v_D = \frac{F}{eB}$ in a direction perpendicular to both $\vec{B}$ and applied external force $\vec{F}$. As the magnitude of the magnetic field increases, the frequency of the rotational motion of the electron increases while the drift velocity tends to zero. In the limit $B \to \infty$, the slow drift motion of the center of the orbit becomes the only physically meaningful motion. External forces affect only the slow motion of the center of the orbit, while the large kinetic energy associated with the fast rotational motion remains unchanged. This results in *quenching* of the kinetic energy in an electronic system at high magnetic field.

In quantum mechanics, the kinetic energy of an electron in a magnetic field is quantized in units of $\hbar\omega_c$, so that its permissible values are,

$$\epsilon_n = \left(n + \frac{1}{2}\right)\hbar\omega_c \tag{2}$$

where, n is a non-negative integer. These energy levels are known as **Landau levels**. The Landau levels were actually first derived by Fock and Darwin (also called Fock-Darwin levels) who solved the more general problem of an electron subjected to both a uniform magnetic field and a harmonic oscillator potential.

The number of degenerate states in each Landau level is proportional to the magnetic field and to the area of the system, and is given by

$$N_L = \frac{eBA}{h} \tag{3}$$

Such enormously large degeneracy corresponds to localization of the cyclotron orbit anywhere in the plane. The gap between two consecutive Landau levels $\hbar\omega_c$ increases with increasing magnetic field, and so does the *capacity*, N_L, of each Landau level. Thus, in the limit of $B \to \infty$, all the electrons fall in the lowest Landau level[1](LLL), with negligible higher Landau levels mixing. Once again, we can conclude that the kinetic energy, in this limit, is essentially a constant equal to the number of electrons times $\frac{\hbar\omega_c}{2}$.

[1] The condition for the quenching of the kinetic energy is $\hbar\omega_c \gg 1$, where V is the energy scale of Landau-level-mixing interactions such as external potentials, electron-electron interactions, etc. This condition does not require that all the electrons reside in the LLL.

The quenching of the kinetic energy in a 2DEG at high magnetic field has far-reaching consequences. The key parameter that controls the properties of the system is the filling factor ν:

$$\nu = \frac{N}{N_L} \tag{4}$$

Its integer part, $[\nu]$, (the largest integer smaller than ν) is the number of completely occupied Landau levels in the non-interacting ground-state, while the remainder, $\nu - [\nu]$, determines the population of the highest occupied Landau level, which is only partially occupied by electrons.

Surprisingly enough, disorder is a crucial ingredient for astonishing Hall plateau quantization. This is because the disorder facilitates Anderson localization for electrons. When electrons occupy these localized energy states, they don't contribute in the electronic conductance. This broadens out the density of states of each Landau level as shown in Fig. 1.2.

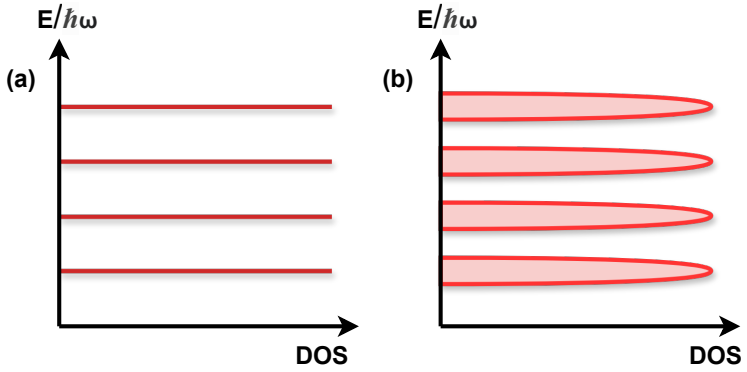

Figure 1.2: (a) Landau levels in a perfectly clean system (b) The broadening of Landau levels in a system with disorder The tails of the broadened Landau levels are contributed by Anderson localized states.

As a result, a constant Hall conductance is maintained for a finite range of filling factor. Alternatively, varying the magnetic field for a finite range yields the same Hall conductance. Thus, quantized plateaus in Hall conductance are realized. Note that, however, a very strong disorder potential leads to overlapping of the smeared Landau levels, which ultimately will destroy the QH effect.

1.3 Landau level calculations

The concept of Landau levels is crucial to understand the integer QH effect. Let us consider an electronic charge e residing in the magnetic field pointing towards the negative z-direction $\vec{B} = -B\hat{z}$. Such convention ensures the holomorphicity of the wavefunctions in the LLL. By coupling to a vector potential $\mathbf{A}$, the corresponding time-independent Schrödinger's equation is:

$$\frac{1}{2m^*}\left(\mathbf{p} - e\mathbf{A}\right)^2 \psi\left(x, y\right) = E\psi\left(x, y\right) \tag{5}$$

We adopt the SI units here. The magnetic field is related to the vector potential $\mathbf{A}$ by $\nabla\times\ \mathbf{A} = \mathrm{B}$. The gauge freedom allows arbitrary choice for definition of $\mathbf{A}$, respecting $\nabla\times$

$\mathbf{A}$ = B. The conventional gauge choices are Landau gauge and the symmetric gauge. The former gauge facilitates the explanation of integer QH effect using the concept of Landau levels and filling factors. The latter displays the holomorphicity of a wavefunction in the LLL.

1.3.1 *Landau gauge*

Let's consider the Landau gauge: $\boldsymbol{A} = (0, Bx, 0)$. The Hamiltonian commutes with the translational operator in the y-direction, the linear momentum in the y-direction is the good quantum number. Therefore, one can write the following ansatz $\Psi(x, y) = \psi(x) e^{ik_y y}$. A direct substitution in Eq.(5):

$$-\frac{\hbar^2}{2m}\frac{d^2\psi}{dx^2} + \frac{m}{2}\left(\frac{eB}{m}\right)^2\left(\boldsymbol{x} - \frac{\hbar k_y}{eB}\right)^2\psi = E\psi \tag{6}$$

This equation describes a set of harmonic oscillators centered around $x_0 = \frac{\hbar k_y}{eB} = k_y l_B^2$. The associated cyclotron frequency ω_c and eigen energy E_n are

$$\omega_c = \frac{eB}{m},\ E_n = \left(n + \frac{1}{2}\right)\hbar\omega_c \tag{7}$$

The corresponding eigenfunctions are determined as

$$\psi_n(x) = \frac{1}{\sqrt{2^n n!}}\left(\frac{m\omega_c}{\pi\hbar}\right)^{1/4}\exp\left[-\frac{1}{2l_B^2}(x - x_0)^2\right]H_n\left(\frac{x - x_0}{l_B}\right) \tag{8}$$

where, $H_n(x)$ denotes the nth order Hermite polynomial in x.

The natural length scale of the wavefunction is identified as:

$$l_B = \sqrt{\frac{\hbar}{eB}} \approx \frac{26}{\sqrt{B[\text{Tesla}]}}\text{nm} \tag{9}$$

This length is called the magnetic length. One can have the intuition about this length scale by thinking about an electron in a magnetic field. Classically, the Larmor radius is given as $R = \frac{mv}{eB}$. According to the uncertainty relation, the product of Larmor radius and the electron's velocity is bounded by $(mv)(R) \sim \hbar$. Hence, the minimum possible radius of the cyclotron orbit is $R_{\min} = \left(\frac{\hbar}{eB}\right)^{\frac{1}{2}}$. Therefore, the magnetic length characterizes the minimum radius of the cyclotron orbit of an electron moving in the QH sample. For instance, a magnetic field of 25 T corresponds to a magnetic length $l_B \sim 5\,\text{nm}$.

From Eq.(7), we see that E_n is independent of k_y , implies each Landau levels being highly degenerate. Consider the system with dimension $L_x \times L_y$, then $k_y \in \left[0, \frac{L_x}{l_B^2}\right]$. In the y-direction, after employing the periodic boundary condition. The degeneracy of each Landau level is determined as:

$$N = \frac{L_y}{2\pi}\int^{\frac{L_x}{l_B^2}} dk_y = \frac{L_x L_y}{2\pi l_B^2} = \frac{\Phi}{\Phi_0} = N_\Phi \tag{10}$$

Note that $\Phi_0 = \frac{h}{e}$ is the magnetic flux quanta. Therefore, the degeneracy of each Landau level is the ratio of the total number of magnetic flux quanta piercing through the sample. The filling factor is defined as:

$$\nu = \frac{N_e}{N_\Phi} = \frac{n\Phi_0}{B} \tag{11}$$

where, N_e is the total number of electrons in the sample. Since Φ_0 is the universal constant, the filling factor (ν) can only be changed by either varying the electron density or / and the magnetic field. For an integer number of filled Landau levels, the system displays the integer QH state. The energy difference between the two closest Landau levels is called cyclotron energy $E_c = \hbar\omega_c$. This makes the system gapped and insulating.

1.3.2 *Symmetric gauge*

Apart from the Landau gauge, the symmetric gauge is another chosen gauge to solve the problem[Girvin and Yang, 2019]. The gauge,

$$\boldsymbol{A} = -r \times \frac{\boldsymbol{B}}{2} = (By/2, -Bx/2, 0)\,. \tag{12}$$

known as the symmetric gauge. This choice of gauge breaks translational symmetry in both the x and y directions; however, the rotational symmetry of the system remains intact. As a consequence, the angular momentum quantum number serves as a good quantum number. In other words, the eigenstates of the Hamiltonian are simultaneously eigenstates of the angular momentum operator.

For simplicity, we restrict our discussion to the lowest Landau level (LLL). We define the complex coordinates and corresponding derivatives as,

$$\begin{gathered} z = x - iy \;;\; \bar{z} = x + iy \\ \frac{\partial}{\partial z} = \frac{1}{2}\left(\frac{\partial}{\partial x} - i\frac{\partial}{\partial y}\right) \;;\; \frac{\partial}{\partial \bar{z}} = \frac{1}{2}\left(\frac{\partial}{\partial x} + i\frac{\partial}{\partial y}\right) \end{gathered} \tag{13}$$

Then the ground state wavefunction $\Psi(z, \bar{z})$ must satisfy, in holomorphic coordinates:

$$\left[\frac{\partial}{\partial \bar{z}} + \frac{eB}{4\hbar c}\right]\Psi(z, \bar{z}) = 0 \tag{14}$$

$$\implies \Psi(z, \bar{z}) = f(z)\exp\left(-\frac{|z|^2}{4l_B^2}\right) \tag{15}$$

where, $f(z)$ is the holomorphic function. Since only $\frac{\partial}{\partial \bar{z}}$ is acting on the wavefunction, any holomorphic function $f(z)$ provides a valid wavefunction solution for the LLL.

1.3.3 *Landau levels – gauge-independent calculations*

In this section, we present the gauge-independent calculations to obtain Landau level spectrum[Girvin and Yang, 2019]. Consider the 2D single-electron Hamiltonian:

$$H = \frac{1}{2m}\left(\vec{p} + e\vec{\boldsymbol{A}}\right)^2 = \frac{1}{2m}\left(\vec{\Pi}\right)^2 = \frac{1}{2m}\left(\Pi_x^2 + \Pi_y^2\right) \tag{16}$$

where,

$$\vec{\Pi} = \vec{p} + e\vec{\boldsymbol{A}} \tag{17}$$

Due to coupling to the magnetic field, canonical momenta in different directions do not commute:

$$[\Pi_x, \Pi_y] = -i\hbar e\left(\partial_x A_y - \partial_y A_x\right) = i\hbar\left(eB\right) = \frac{i\hbar^2}{l_B^2} \tag{18}$$

Furthermore, we define the raising and lowering operators from Π:

$$a = \frac{l_B}{\sqrt{2}\hbar}\left(\Pi_x + i\Pi_y\right); a^\dagger = \frac{l_B}{\sqrt{2}\hbar}\left(\Pi_x - i\Pi_y\right) \tag{19}$$

The above defined conjugate operators satisfy $\left[a, a^\dagger\right] = 1$. Using a and $a^\dagger$, the Hamiltonian can be written in the second quantized form for a harmonic oscillator:

$$H = \hbar\omega_c\left(a^\dagger a + \frac{1}{2}\right). \tag{20}$$

One thus immediately gets the Landau-level spectrum

$$E_n = \hbar\omega_c\left(n + \frac{1}{2}\right), \tag{21}$$

without specifying the gauge. The ground state is annihilated by a, condition valid in any gauge.

Let's now investigate the reason behind the massive degeneracy of Landau levels. Let $\hat{z}$ be the unit vector in the direction of magnetic field. To understand this, we introduce another set of conjugate variables, known as **guiding center coordinates:**

$$\vec{R} = (R_x, R_y) = \vec{r} - l_B^2\left(\hat{z} \times \vec{\Pi}\right)/\hbar \tag{22}$$

from which one gets,

$$[R_x, R_y] = -il_B^2 \tag{23}$$

We can thus introduce new set of harmonic oscillator operators,

$$b = \frac{1}{\sqrt{2}l_B}\left(R_x - iR_y\right); b^\dagger = \frac{1}{\sqrt{2}l_B}\left(R_x + iR_y\right)$$

with $\left[b, b^\dagger\right] = 1$. More importantly,

$$[R_i, \Pi_j] = [R_i, H] = [a, b] = \left[a, b^\dagger\right] = 0 \tag{24}$$

Thus we have two harmonic oscillators, defined by operators a and b, but operator b doesn't appear in the Hamiltonian expression(20). The operators b and $b^\dagger$ are associated with the guiding center coordinates R_x and R_y. They represent another degree of freedom related to the position of the center of the cyclotron orbit. The absence of b and $b^\dagger$ in the Hamiltonian implies that there are multiple states with the same energy. These states are distinguished by different quantum numbers associated with b and $b^\dagger$, but they all have the same Landau level index n. This leads to high degree of degeneracy for each Landau level.

All the discussion above is independent of the choice of gauge.

1.3.4 *Relevant energy scales*

Before the discussion of any theoretical framework of FQHE, it is crucial to analyze different energy scales in the system. This allows us to analyze the conditions to observe FQHE state.

1.3.4.1 *Energy level in quantum well*

The semiconductor heterostructure used in experiments is a three-dimensional system. A quantum well is formed by applying a confining potential in the z-direction. Let's consider the sample to be W units wide, then the potential profile in the z-direction can be approximated as an infinite potential well with a depth W. The energy is confined due to this confinement:

$$\epsilon_n = \frac{\pi^2 \hbar^2 n^2}{2m^* W^2},\ n = 1, 2, \cdots. \tag{25}$$

The effective mass of the electron, denoted as m^*. In GaAs, $m^* \approx 0.067\, m_e$, meanwhile the depth W of the quantum well in the typical experiment is $W \approx (20 - 30)$ nm. Therefore,

$$\Delta\epsilon = \epsilon_2 - \epsilon_1 \approx (20 - 30)\ \text{meV} \tag{26}$$

which corresponds to be an effective temperature around 300 K. When the temperature of the system in sufficiently lower than 300 K, the transverse degree of freedom of electrons is frozen out. This leads to a system of two-dimensional electron liquid.

1.3.4.2 *Cyclotron gap*

The Landau level quantization of energy levels responsible for QH effect:

$$E_c = \hbar\omega_c = \frac{\hbar e B}{m^*} \tag{27}$$

The strength of the applied magnetic field to observe a QH state depends on the number density of the electrons in the sample (see Eq.(11)). In a typical experiment, $B \approx 12.5\,\text{T}$ is applied to observe $\nu = 1$ integer QH state. This leads to $E_c \approx 20\,\text{meV}$ or an effective temperature of about 250 K. When the temperature of the system is lower than the 250 K, electrons occupy the LLL while all higher Landau levels are empty. This states the importance of the low temperature to observe QH effect in semiconductor heterostructures.

1.3.4.3 *Coulomb interaction*

The electronic Coulomb interaction plays a vital role in understanding the FQHE. If one assumes the typical length difference between the two electrons of the order of magnetic length, the corresponding potential energy is given by:

$$E_C = \frac{e^2}{\epsilon l_B} \tag{28}$$

For the GaAs sample, the dielectric constant is approximately 12.9. At $B = 12.5\,\mathrm{T}$, the Coulomb repulsion energy corresponds to an effective temperature of about 175 K.

The Landau level mixing arises from the competition between Coulomb interaction of electrons and energy gap between Landau levels. Quantitatively, a dimensionless parameter called Landau-level mixing is defined as the ratio of the Coulomb interaction to cyclotron energy as:

$$\kappa = \frac{E_C}{E_c} = \frac{ke^2/\left(l_B\right)}{\hbar\omega_c} \propto \frac{1}{\sqrt{B}}. \tag{29}$$

A large κ indicates that the interaction between electrons is so large that the electrons are not confined in a single Landau level. For example, the effective mass of electrons in ZnO is about five times larger than the ones in GaAs. The result is that the gap between Landau levels in ZnO is smaller than GaAs, which may provide a platform to study the physical effect from large Landau-level mixing [Falson et al., 2018]. At the same time, it is challenging to numerically simulate system with a large κ.

1.4 Fractional quantum Hall effect

In this section, we briefly introduce the fractional quantum Hall effect for the sake of completeness. Although the subsequent parts of this thesis do not explicitly address the fractional quantum Hall effect and are restricted to the integer case, its discussion provides important motivation for the studies presented in this work.

So, we start with the fractional quantum Hall effect. In the presence of a very strong external magnetic field (typically $B > 10\,\mathrm{T}$), the degeneracy N_L of the Landau levels can exceed the total number of charge carriers. As a consequence, the filling factor satisfies $\nu < 1$. In 1982, experiments found the Hall quantization of conductance at rational values of the filling factor, $\nu = \frac{p}{q}$, where p and q are integers and q is odd. Such occurrence of rational number quantized conductivity,

$$\sigma_{xy} = \nu\frac{e^2}{h}, \quad \nu = \frac{p}{q} \tag{30}$$

is known as fractional quantum Hall effect (FQHE). Unlike the integer quantum Hall effect, where localization of electronic states plays a central role in producing quantized Hall plateaus, the fractional quantum Hall effect arises from strong electron–electron interactions that open an energy gap in the many-body spectrum. The formation of these correlated states requires extremely clean (low-disorder) samples. However, a small amount of disorder remains essential to create localized states that pin the Fermi energy between extended states, thereby ensuring the stability of quantized Hall plateaus and the vanishing of the longitudinal resistivity.

Although the underlying physics of FQHE is governed by strong electron-electron interaction, the role of disorder in the IQHE and FQHE is qualitatively similar: it produces localized states that are essential for the formation of quantized Hall plateaus.

Nevertheless, the origin of the energy gap that protects the quantized Hall phase differs — *single-particle Landau level spacing* for the IQHE and *many-body correlation energy* for the FQHE. As a result, the FQHE is much more sensitive to disorder: while

weak disorder helps to stabilize plateaus, stronger disorder destroys the correlated state altogether.

This particularly poses the FQHE as a challenging problem, since the application of conventional many-body methods is limited: there is no small parameter in the system that would allow for an effective use of perturbation theory.

1.4.1 *Laughlin wavefunction*

From the previous section, we learn that the problem of FQHE cannot be understood without taking interaction into account. Because such many body problem cannot be solved exactly, a possible way to approach a solution is by using variational wavefunctions. The first attempt in this direction was made by Robert Laughlin who proposed the first trial wavefunction [Laughlin, 1983]. Laughlin suggested a variational ground state wavefunction for interacting electrons projected on the LLL, for the case $\nu = \frac{1}{m}$, which of the form,

$$\Psi_0\left(\{z_i\}\right) = \prod_{i<j=1}^{N} \left(z_i - z_j\right)^m e^{-\sum_{k=1}^{N} |z_k|^2/4l_B^2} \tag{31}$$

Here, $z_i = x_i + iy_i$, where (x_i, y_i) are the coordinates of the ith electron in the plane perpendicular to the magnetic field. In order for this to remain analytic, m must be integer. When m is an odd integer, the wavefunction is anti-symmetric upon the exchange of the electrons, i.e., $z_i \longleftrightarrow z_j$.

The Laughlin wavefunction naturally builds in good correlations among other electrons because each particle sees an m-fold zero at the positions of all the other particles. The wavefunction vanishes extremely rapidly if any two particles approach each other, and this helps minimize the expectation value of the Coulomb energy. Numerical simulations carried out for few electrons displayed an astonishing overlap of the Laughlin wave-function with the exact wave function at $\nu = \frac{1}{3}, \frac{1}{5}$ and $\frac{1}{7}$ [Fano et al., 1986]. Below $\nu < \frac{1}{7}$, a crystal is formed [Lam and Girvin, 1984]. By particle-hole conjugation in the LLL, Laughlin's theory also explains the plateau observed at fractions $\nu = 1 - \frac{1}{m}$, which can be understood as a $\frac{1}{m}$ Laughlin state of "holes".

Charged excitation

Laughlin also constructed wavefunctions for the charged excitation in this system. Laughlin's wavefunctions for the positively charged excitation, referred as a quasi-hole and a quasi-particle, located at a position η are:

$$\Psi_h\left(\{z_i\}, \eta\right) = N_h \Pi_i \left(z_i - \eta\right) \Psi_0 \tag{32}$$

$$\Psi_p\left(\{z_i\}, \eta\right) = N_p \Pi_i \left(\frac{\partial}{\partial z_i} - \frac{\eta}{l_B^2}\right) \Psi_0 \tag{33}$$

where $\mathrm{N_p}$ and $\mathrm{N_h}$ are the normalization constants. The derivative in Eq.(33), must only act on the polynomial part of the wavefunction and not on the Gaussian factor. One can have the intuition about the above quasi-hole/quasi-particle wavefunctions as follows: Consider the situation where $\eta = 0$. The polynomial factor $\prod_i z_i$ pushes electrons away from the origin (the wavefunction of Eq.(32) vanishes at $\eta = 0$), thereby depleting the electron density at the origin resulting in the formation of positively charged quasi-hole. The derivatives, on the other hand, pull electrons in towards the origin which leads to

a built-up of an excess charge at the origin, resulting in the formation of a negatively charged quasi-particle.

Using the plasma analogy [Laughlin, 1990], Laughlin showed that the quasi–hole excitation carries a fractional charge of $\frac{e}{m}$. Via, the PH (Particle-Hole) conjugation, one can readily see that the quasi-particle excitation also carries a fractional charge of value $-\frac{e}{m}$. Shot-noise experiments have verified the presence of $1/3$ charged quasi-particles in the $\nu = 1/3$ state [Dolev et al., 2008, de Picciotto et al., 1997, Saminadayar et al., 1997].

This construction further yields the statistics of the quasi particle and quasi-holes [Moore and Read, 1991]. Starting from the wavefunction describing excitation of, say two holes, an exchange operation presents a phase factor $e^{i\theta}$ that is not necessarily equal to ± 1, $(+)$ for bosons and $(-)$ for fermions. Thus,

$$\begin{aligned} \Psi_h\left(z_a, z_b\right) &= N_{ab} \prod_{i=1}^{N} \left(z_i - z_a\right)\left(z_i - z_b\right) \Psi_0 \\ \Psi_h\left(z_b, z_a\right) &= P_{ab} \Psi_h\left(z_a, z_b\right) = e^{i\theta} \Psi_h\left(z_a, z_b\right) \end{aligned} \tag{34}$$

where P_{ab} is the exchange operator. Recent experiments [Bartolomei et al., 2020, Nakamura et al., 2020] have confirmed that the quasi-hole and quasiparticle excitations of the Laughlin state are Abelian anyons with a statistical phase $\theta = \frac{2\pi}{3}$.

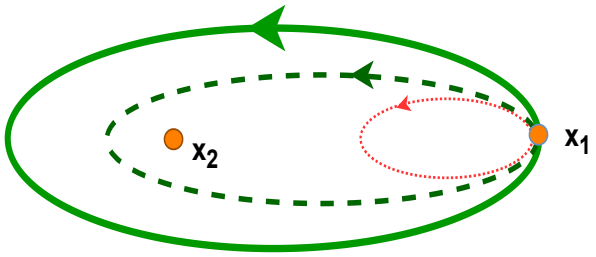

Figure 1.3: Braiding in two-dimensional world.

1.4.2 *Composite fermions*

The dichotomy between strong correlation in partially filled Landau levels and weak correlation in full Landau levels is turned to one's advantage in the composite fermion approach (for reviews, see [Jain and Kamilla, 1997, Heinonen, 1998]).

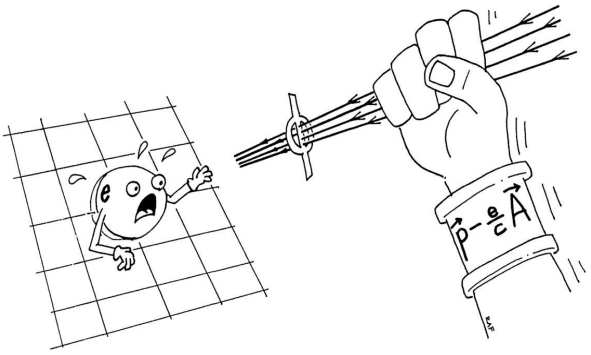

Figure 1.4: Illustration of a charged particle-flux composite. The resulting composite object is known as Composite fermion. Figure adopted from [Wilczek and Shapere, 1989].

This approach considers attaching to each electron an infinitely thin, massless magnetic solenoid carrying an even number of flux quanta. Such a conversion preserves the minus sign related with the swapping operation of two fermions, as bound state of an electron and the flux quanta is itself a fermion. Hence, the name *composite fermions*. Furthermore, the Aharonov-Bohm phase factors associated with the closed loops remains unaffected, as the additional phase factor due to the attached flux $\phi_{\text{attach}} = 2p\phi_0$ is $e^{2\pi i \phi_{\text{attach}}/\phi_0} = 1$. Thus, the attached flux remains unobservable, leaving this new formulation of composite fermions, identical to the original problem of interacting electrons.

The real advantage of this description appears only under mean-field approximation. Under such approximation, the fictitious magnetic flux attached to the particles is replaced by an average magnetic flux proportional to the particle density. This average magnetic flux combines with the external applied magnetic field to yield an effective magnetic field

$$B^* = B - 2p\rho\phi_0 \tag{35}$$

, where the flux tubes have been assumed to be anti-parallel to the external field for $p > 0$ and parallel for $p < 0$. Thus, the net effect is that each electron has absorbed $2p$ flux quanta from the external field to become a composite fermion. Note that the transformation of $B \to B^*$ is not linear in B, i.e, as fraction $\nu = \frac{1}{3}$ maps to integer $\nu^* = 1$, however fraction $\nu = \frac{1}{4}$ maps to $\nu^* = \frac{1}{4}$. The composite fermions, in this approximation, feel the effective field B^* and their effective filling factor ν^* is therefore given by:

$$\nu = \frac{\nu^*}{2p\nu^* \pm 1} \tag{36}$$

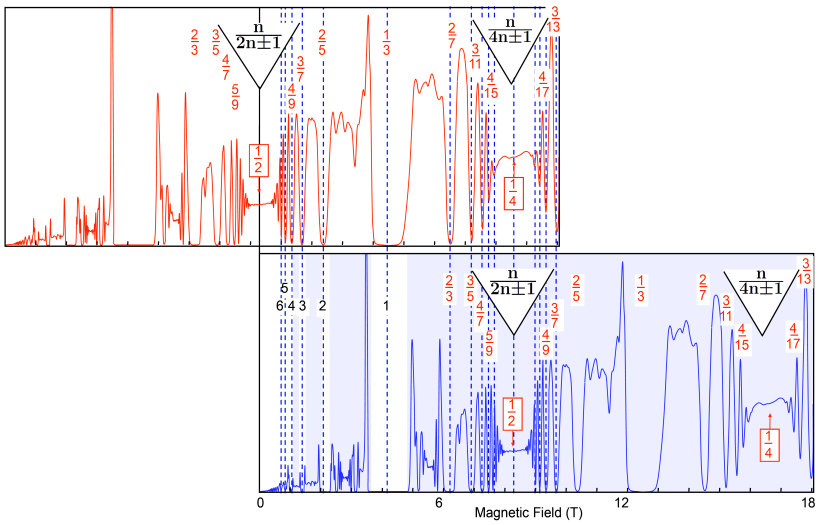

Figure 1.5: In the upper panel, the FQHE trace is plotted as a function of $B^* = B - 2\rho\phi_0$, which is effective magnetic field seen by the composite fermions carrying two vortices. A correspondence of the FQHE around $\nu = \frac{1}{3}$ can be seen with the IQHE of the electrons in the lower panel. Figure adapted from [Halperin and Jain, 2020].

The composite fermion picture also establishes a beautiful connection between the integral and the fractional QH effects. Under such mapping, the FQHE of electrons is nothing but the integral QH effect of composite fermions (Fig. 1.5).

1.5 Topology in quantum Hall effect

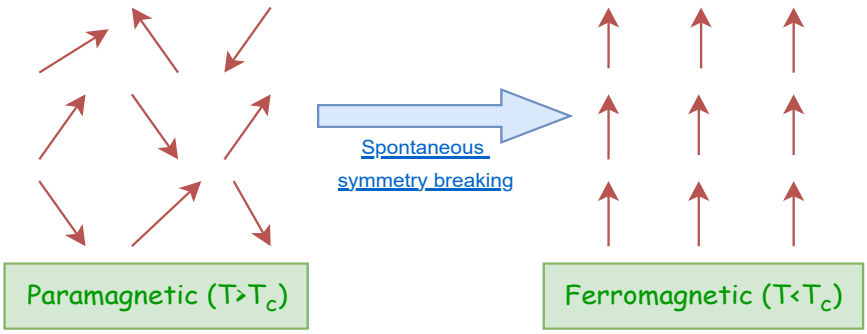

Figure 1.6: Illustration of spontaneous symmetry in Landau's theory of phase transition: Paramagnetic to ferromagnetic state. T_c is the critical temperature.

One of the crucial aspects addressed in the field of condensed matter is the understanding and classification of the phases of matter. The first light in this direction came from the Landau's 1930 phenomenological theory of continuous phase transition [L., 1965]. According to it, the occurrence of the phase transition associated with certain type of symmetry breaking. For example: the ferromagnetic phase transition breaks the original SO(3) symmetry and reduce to SO(2) symmetry (see Fig. 1.6). Moreover, an order parameter can be assigned to characterize various phases. For a disorder phase configuration, the ordered parameter is zero while it becomes non-zero when the transition

to ordered phases occurs. For above example, magnetization serve as a relevant order parameter. However, the Landau theory doesn't encompasses all the possible phase transitions.

In the groundbreaking work, Kosterlitz–Thouless (KT) demonstrated the possibility of new kind of phase transitions which doesn't undergo any spontaneous symmetry breaking [Kosterlitz and Thouless, 1973]. Infact, KT transitions have a topological origin.

By introducing the periodic potential, Thouless, Kohmoto, Nightingale and den Nijs (TKNN) showed that each Landau energy band have a certain non-trivial topology [Thouless et al., 1982]. Different number of filled Landau levels corresponds to different integer QH states which are associated with different topological states. In addition, TKNN successfully formulated the electrical Hall conductance as an integral over the Berry curvature of the wave function. This integral turns out to be a topological invariant, which is called the Chern number. Without closing the gap in the energy bands, no continuous transformation in the Hamiltonian can connect two topologically distinct phases. Therefore, the Hall conductance is topologically protected and being robust against small perturbations.

- **Lattice model for integer QH effect:**

Let's consider an example of electron moving in a constant magnetic field, under the influence of a periodic potential from the crystalline background. The simplest model to incorporate the orbital effect of a magnetic field in a model of a crystal is Hofstadter model. The model exhibit rich behavior , but we restrict ourselves to weak magnetic field, thus recovering Landau level physics.

First, lets take free electrons moving on a square lattice with the lattice parameter a. Let's ignore the electronic spins for now. The tight-binding hopping with the nearest-neighbour hopping is given by (in zero magnetic field),

$$H = -\sum_{\langle ij \rangle} t \left(c_i^\dagger c_j + h.c. \right) \tag{37}$$

where, $t > 0$ is the hopping matrix element and the sum is defined over nearest neighbor sites i and j. With the periodic boundary condition on the $N \times N$ lattice net, introduce the Fourier-transformed plan wave operators,

$$c_{\boldsymbol{k}}^\dagger = \frac{1}{\sqrt{N}} \sum_i c^\dagger e^{-i\boldsymbol{k}\cdot\boldsymbol{r_i}} \tag{38}$$

where the components of $\boldsymbol{k} = (k_x, k_y)$are inter multiples of $\frac{2\pi}{Na}$, and $\boldsymbol{r_i}$ is the location of site i. We can the diagonalize the Hamiltonian as,

$$H = \sum_k \epsilon_k c_k^\dagger c_k \tag{39}$$

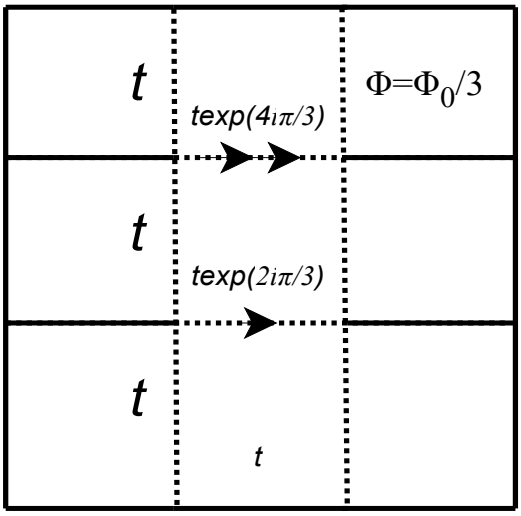

Figure 1.7: The Hofstadter model. The particle hop over a square lattice with magnetic flux $\Phi = \frac{\Phi_0}{3}$ passing through each plaquette. The Landau gauge is chosen with vector potential along x and varying along y. All the vertical bonds have zero-field hopping t. Horizontal bonds can take three possible values, denoted by zero, one and two arrows respectively. The supercell of the system denoted by dotted lines at this flux contains three original unit cells.

with the eigenenergies $\epsilon_{\boldsymbol{k}} = -2t\,(cosk_x a + cosk_y a)$. This system has one site per unit cell.

The Hofstadter model [Hofstadter, 1976] is obtained by adding a uniform perpendicular magnetic field $\boldsymbol{B} = B\hat{\boldsymbol{z}}$ to above defined tight-binding model with flux Φ per unit cell (see Fig. 1.7). The incorporation of a magnetic field into the tight-binding model can be performed as follows: Moving an electron around a unit plaquette should pick up a phase ϕ through the Aharonov-Bohm effect. This is done by modifying the Hamiltonian in (37) to incorporate a phase into hopping amplitudes,

$$H = -\sum_{\langle ij \rangle} \left[t \, \exp\left(i \frac{2\pi}{\phi_0} \int_{\boldsymbol{r_i}}^{\boldsymbol{r_i}} \boldsymbol{A}.\boldsymbol{dr} \right) c_i^\dagger c_j + h.c. \right] \tag{40}$$

Here, $\mathbf{A}$ is the electromagnetic vector potential created by the magnetic field.

1.6 Overview of concepts covered

In this chapter, we present a brief on both integer and fractional quantum Hall effects. Furthermore, we introduce the composite fermion framework, which provides a powerful mapping between the fractional filling factors of a two-dimensional electron gas and the integer quantum Hall states of emergent electron–flux composite particles. We conclude with a brief discussion of the topological nature of the quantum Hall effect.

2

Introduction to devices and probes

In this chapter, we provide an overview of the key devices and probes central to our study. We begin by introducing two-dimensional electron gas (2DEG) heterostructures. Next, we focus on the single quantum point contact (QPC), discussing its operational principles and reviewing relevant tunneling experiments. Finally, we explore the Mach-Zehnder interferometer, which consists of two QPCs, and examine major experiments involving short pulses within the quantum Hall regime.

2.1 2D gas heterostructures

A two-dimensional electron liquid is formed at the interface of semiconductor and an insulator or two semiconductors. This is due to the two different material band gaps on the interface of what it is formed. The most conventional 2D gas based device is $Si - SiO_2$ MOSFET (Metal Oxide Semiconductor Field Effect Transistor), as shown in Fig. 2.1(a), was first reported by Kahng and Atalla in 1963 [Kahng, 1963].

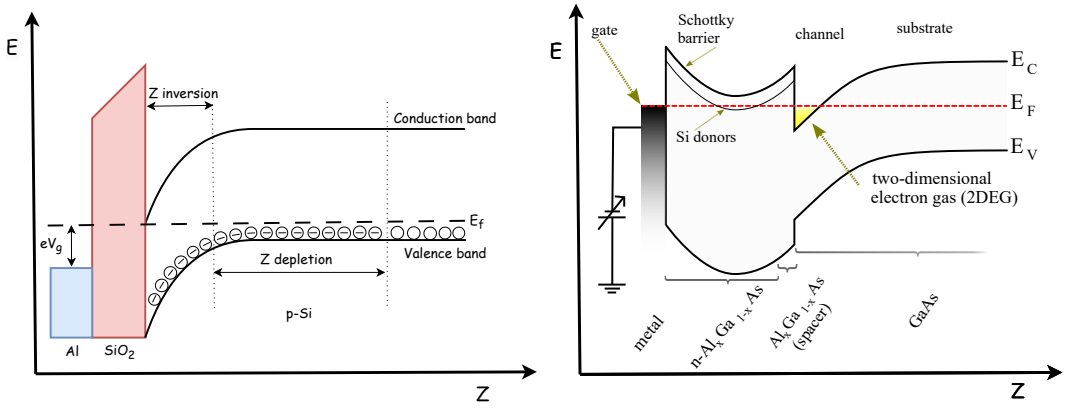

Figure 2.1: (a) Energy band diagram of a Si MOSFET. (b) Energy band diagram of a AlGaAs/-GaAs based 2DEG. The figure is adapted from Wikipedia.

In 1978, Dingle and collaborators [Dingle et al., 1978] devised a new kind of 2DEG, formed by using the technique of molecular beam epitaxy (MBE) for devising AlGaAs/-GaAs heterostructure. The typical schematics of the heterostructure is shown in Fig. 2.1(b).

In comparison, typical low temperature mobility for such devices is a few 10^7 $cm^2/Vsec$, with the highest reported mobility reaching $3.5 \times 10^7 cm^2/Vsec$ [Umansky et al., 2009]. The mobility translated into a mean free path l, according to $l = (2\pi n)^{1/2} \mu\hbar/e$. Thus, for typical Si-MOSFET parameters (density of $10^{11} cm^{-2}$ and mobility of 10^4 $cm^2/Vsec$), mean free path $l = 500\,\text{Å}$. In contrast, the mean free path in a high mobility AlGaAs/GaAs

device $\left(\mu = 10^7 \mathrm{cm}^2/\mathrm{Vsec}\right)$ exceeds 50 μm. This contrast demonstrates that AlGaAs/GaAs heterostructures, with their longer mean free paths and higher mobilities, provide a superior platform relative to standard Si devices.

2.2 Quantum point contacts

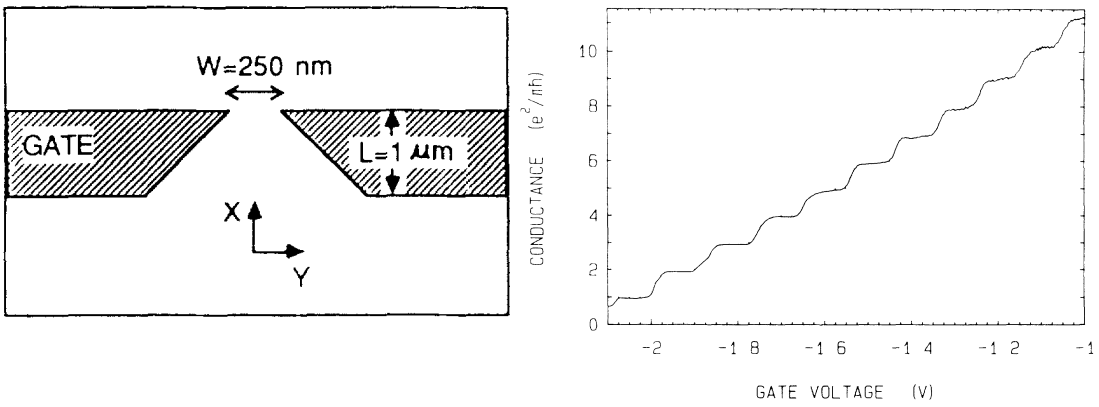

(a)

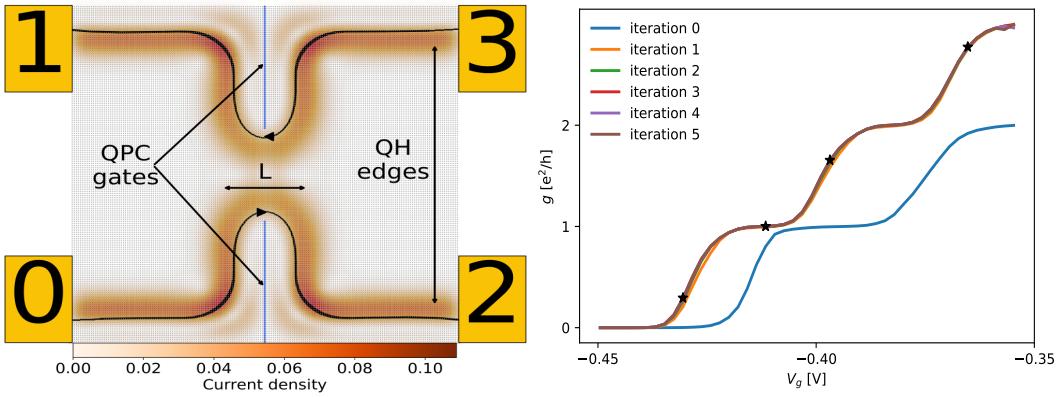

(b)

Figure 2.2: **Conductance quantization in a quantum point contact (QPC) in the absence (a) and presence (b) of a magnetic field.** (a) Conductance quantization through a QPC measured at 0.6 K in the absence of a magnetic field. Conductance G varies as a function of gate voltage, showing stepwise behavior in a unit of $2e^2/h$ [van Wees et al., 1988]. (b) Conductance quantization in the presence of a magnetic field. Shown in numerical simulation of a QPC geometry with narrow QPC-defining gates. The figure presents the current density of QH edges in a sample that has four leads and a QPC defined by inifinite potential on narrow gates(blue lines). The red density map represents the current density of two edge states. The edge states go around the gated regions smoothly, so that the tunnelling would happen over a finite QPC width of a few magnetic lengths. Conductance of QPC in units of e^2/h as a function of gate voltage V_g. The figure is adapted from [Armagnat et al., 2019].

The quantum point contact (QPC) is a fundamental "building block" of most realized mesoscopic devices. A QPC is fabricated in a 2DEG formed out of a GaAs/AlGaAs heterostructure, using a pair of gate electrodes. A negative gate voltage depletes the electron density underneath the electrodes, and reduces the width of the 2DEG constriction. The constriction works as a point contact between the two large 2DEG regions.

Quantized conductance in such a structure was first observed independently by [van Wees et al., 1988, Wharam et al., 1988] in GaAs/AlGaAs 2DEG systems configured with electrostatic gates, see Fig. 2.2. Subfigs. 2.2((a) and (b)) show the experimentally observed conductance quantization in the absence of an external magnetic field. In contrast, subfigs. 2.2((c) and (d)) present numerical simulations of conductance quantization under conditions relevant to the quantum Hall regime.

QPCs have been used extensively as electronic beam splitters [Liu et al., 1998], which split the motion of an electron beam into the reflected and transmitted modes. The experiments relevant to the quantum Hall effect and the role of QPCs in that context are discussed in the following section.

Tunneling experiments

Edge channels are ideal one-dimensional conductors. The physical separation between the opposite edges leads to suppression of back scattering and therefore, the electrons are exhibit elastic propagation over long lengths ($\sim$ mm at low temperatures). Such properties made them a convenient platform to test the Landauer-Büttiker relations [Büttiker, 1988],[Haug et al., 1988]. In order to perform such test, one must intentionally introduce elastic backscattering in a controllable fashion.

The tool which facilitate such requirement is a quantum point contact (QPC) (as in Fig. 2.2). With the help of an QPC the opposite edges can be brought close enough to induce backscattering. A set of remarkable experimentation came along with QPCs was the observation of the fractional charges. A QPC is used in order to realize a controllable local coupling between the two $v = 1/3$ fractional edges to reflect partially the incoming current. When quasiparticles shot noise tunnelling through the FQH systems stochastically at finite temperature T, is define as:

$$S = 2e^*\langle I\rangle \left[\coth\left(\frac{e^*V}{2k_BT}\right) - \frac{2k_BT}{e^*V}\right] \tag{1}$$

Here, $\langle I\rangle$ is the back-scattered current, and e^* is the effective charge of tunneling quasiparticles. Figures 2.3(a) and 2.3(b) compare the experimental shot- noise data at $\nu = 1/3$ and $2/3$ respectively, with the theoretical one simulated using Eq.(1) (see Fig. [Saminadayar et al., 1997, de Picciotto et al., 1997]). When the backscattered current $\langle I\rangle$ increases with the source-drain bias, the shot noise also increases, agreeing with the theoretical curves for $e^* = e/3$. These observations are the hallmark of Laughlin's $e/3$ quasiparticles in FQH systems. After these observations, shot-noise measurements demonstrated various fractional charges, for example, $e/5$ quasiparticles in the $\nu = 2/5$ state [Reznikov et al., 1999] and the $e/7$ quasiparticles in the $\nu = 3/7$ state [Chung et al., 2003], clearly exhibiting the importance of shot-noise measurements for observing exotic charge carriers.

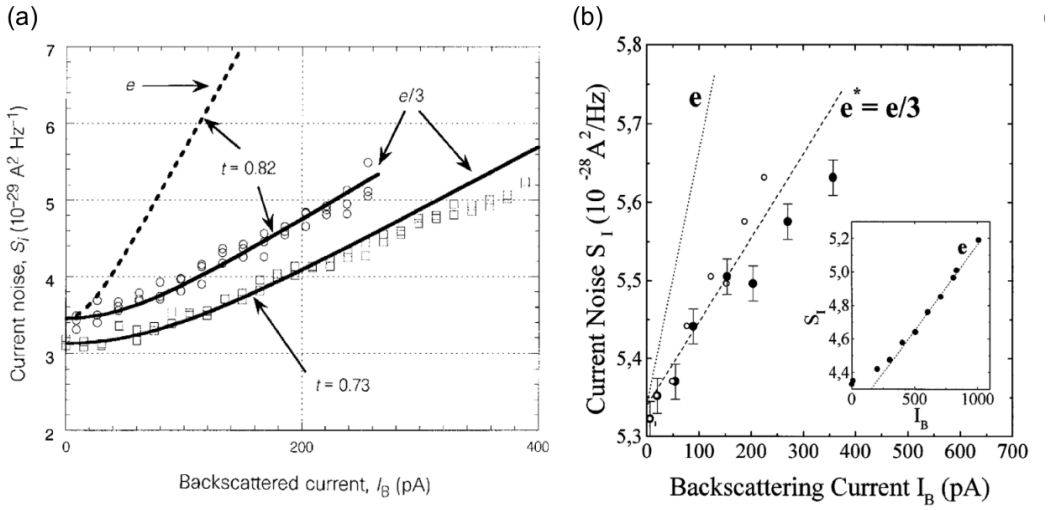

Figure 2.3: (a) Quantum shot noise measurements of the fractional charge at $\nu = 1/3$ and $\nu = 2/3$. The data is consistent with the quasiparticles charge being fractional $e/3$ (solid lines) and inconsistent with charge e (dashed lines). (b) Quantum shot noise in $\nu = 2/3$. The figures are being adapted from [Saminadayar et al., 1997, de Picciotto et al., 1997]

2.3 Mach-Zehnder interferometer

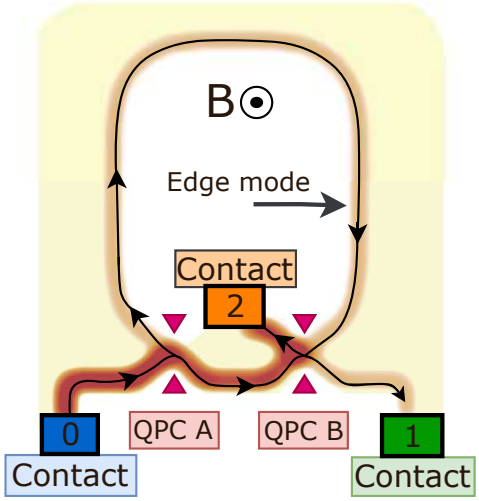

Figure 2.4: **Illustration of Mach-Zehnder Interferometer in quantum Hall regime**. The device consists of three contacts: two outer contacts (0 and 1) and one inner contact (2). Quantum point contacts (QPC A and QPC B) act as beam splitters for the chiral edge state injected from source contact 0. The edge channel is partially transmitted and reflected at QPC A, with the two paths recombining at QPC B. The resulting current is collected at the inner contact 2 and outer contact 1.

The Mach-Zehnder interferometers (MZIs) have been proposed theoretically and implemented experimentally as tools to probe the electronic charge and statistical properties. The electronic MZI setup is realized by two quantum point contacts (QPCs) and one-dimensional ballistic edge state in quantum Hall regime. Analogous to an optical MZI

setup, where mirrors act as beam splitters, in electronic interferometers, QPCs split the incoming edge state according to their respectively tuned transmission.

The MZI has been used widely to study fundamental phenomenon like quantum coherence, electron-electron interaction, entanglement as well as two particle interference. A possible realization of the MZI is an AB-ring combined with two tunnel-coupled wires. In the recent years, such system in quantum Hall settings, proves to be an efficient platform for realizing the flying qubits. Flying qubits are plausible quantum technology realized using purely electronic excitations . In addition to ability to transfer the quantum system over a long distance, flying qubits operates at very short operation time compared to other solid-state qubits. The operation time L/v_F (L, gate length; v_F, Fermi velocity) is of the order of 10 pico-second (10^{-12} s). For higher quality heterostructures, the coherence length can be as long as L_ϕ=100 μm. Since each quantum operation is within $1\mu m$ scale, it is possible to perform $\sim$ 100 qubit operations on the fly [Yamamoto et al., 2012].

The schematic of the Mach-Zehnder interferometer is presented in Fig. 2.4. With respect to quantum Hall settings, the first QPC partitioned the coming electron edge which propagates along the two arms of the interferometer. The two edges from the respective arms then combine to exhibit the interference phenomenon. To observe the interference pattern, one needs to vary the Aharonov-Bohm (AB-) flux through the surface S define between the two arms of the interferometer. The interference signature is displayed in the current characteristics, transmitted to the contact 1. The reflected part from second QPC is been absorbed by an inner contact. This inner contact is crucial in avoiding the re-injection of the electrons again into the interferometer, thus leading to more complicated interference pattern. The transmission probability D through the MZI is given by [Ji et al., 2003],

$$D = D_A D_B + (1 - D_A)(1 - D_B) + 2\cos(\Phi)\sqrt{D_A D_B (1 - D_A)(1 - D_B)}, \qquad (2)$$

where $\Phi = \frac{BS}{\hbar/e}$ with S being the area of the interferometer. Let D_A and D_B be respective tuned transmission probabilities of the first (A) and second (B) beam splitter. The AB-flux can be controlled either by varying the area defined by the two arms of the interferometer using gates or by varying the applied external magnetic field. Fig. 2.5 shows the current oscillations due to interference, under the variation of gate voltage and applied external magnetic field.

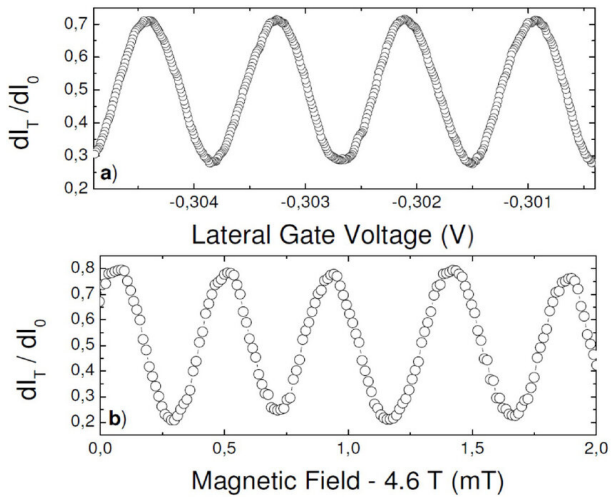

Figure 2.5: **DC interference measurements**. (a) MZI transmission as a function of the lateral gate voltage. (b) MZI transmission as function of the magnetic field. The interference pattern was obtained at filling factor $\nu = 2$ and $T = 20\,\mathrm{mK}$. The figure is adapted from [Yamamoto et al., 2012].

2.4 Short pulses experiments

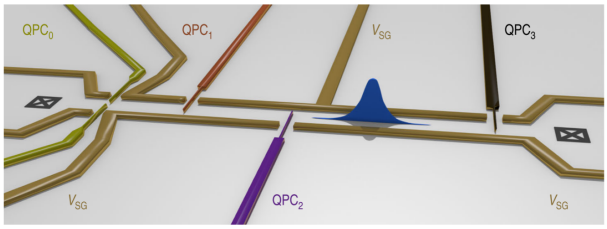

Figure 2.6: **Device and time-of-flight measurements**. Schematic of the quantum device. A few-electron pulse is launched at the left Ohmic contact (blackcrossed box) by applying a short voltage pulse. Three QPCs, denoted as $\mathrm{QPC}_1, \mathrm{QPC}_2$ and QPC_3, are placed along the quantum device. Each of these three QPCs is connected to a large bandwidth (40 GHz) bias tee and operated as an ultra fast switch. Time-resolved detection of current is done at the right Ohmic contact. QPC_0 is used as a channel selection. The figure is adapted from [Roussely et al., 2016].

In recent years, significant interest has emerged in the generation and propagation of single-electron pulses in mesoscopic systems, motivated by their potential applications in quantum information processing [Haack et al., 2011, Edlbauer et al., 2022]. The controlled manipulation of such pulses enables the study of coherence and interaction effects at the single-particle level.

To observe the interference effects discussed in this thesis, the pulse duration must be shorter than 100 ps, which requires ultrafast electronic control. However, the propagation of such short pulses is strongly influenced by Coulomb interactions [Matveev and Glazman, 1993], which can significantly modify their shape and velocity.

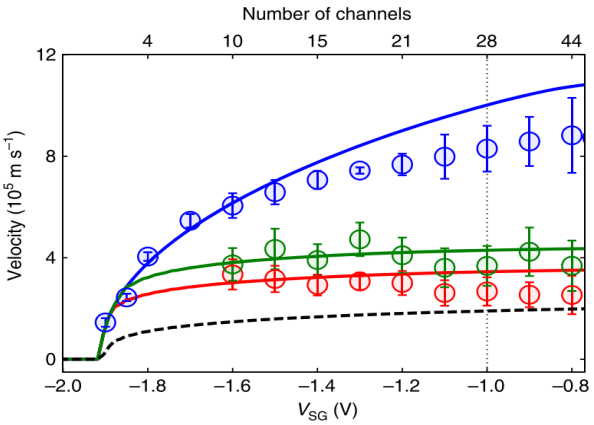

Figure 2.7: **Velocity versus confinement potential**. Velocity of the electron pulse as a function of the confinement potential and the corresponding number of channels. Open circles: experimental data, solid lines: parameter-free self-consistent calculation. The blue data points correspond to the situation where the channel selection QPC0 is not activated. The red (green) data are obtained by setting the channel selection QPC_0 at a conductance value of G= $2e^2/h$ (G=$4e^2/h$). The red (green) solid line corresponds to the velocity of the fast plasmon mode for a one-channel (two-channel) Tomonaga–Luttinger liquid. The black dashed line corresponds to the non-interacting Fermi liquid. The figure is adapted from [Roussely et al., 2016].

This influence becomes particularly evident in time-of-flight measurements in low-dimensional conductors (see Fig. 2.6). These experiments demonstrate how interactions affect charge dynamics in one-dimensional systems [Roussely et al., 2016]. By tuning the confinement potential, the system can transition from a Tomonaga–Luttinger liquid to a multi-channel Fermi liquid regime, resulting in an order-of-magnitude variation in the collective charge velocity (see Fig. 2.7).

Furthermore, to sculpt such charge excitations, for example in chiral edge channels, ultrafast gate drives can be used. However, the final excitation profile is governed by the full dynamical electrostatic response of the system [Misiorny et al., 2018]. In this thesis, we numerically investigate the effect of the mean-field Coulomb interaction on a single-electron pulse propagating through an interferometer in the quantum Hall regime.

2.5 Overview of concepts covered

In this chapter, we have introduced the key devices and experimental probes that form the foundation of the studies presented in this thesis. We began with an overview of two-dimensional electron gas (2DEG) heterostructures, emphasizing the advantages of high-mobility AlGaAs/GaAs systems over conventional Si-based devices.

We then discussed the quantum point contact (QPC), a central building block of mesoscopic electronics. The principles of conductance quantization were reviewed both in the absence and in the presence of a magnetic field, highlighting the role of QPCs as tunable constrictions and electronic beam splitters. In the quantum Hall regime, QPCs enable controlled coupling between chiral edge channels and provide a powerful tool for inducing and studying backscattering. This capability has been crucial for tunneling and shot-noise experiments, which have led to the experimental observation of fractionally

charged quasiparticles and have provided direct evidence for the exotic excitations of fractional quantum Hall states.

Building on the functionality of QPCs, we discussed the electronic Mach–Zehnder interferometer, realized using two QPCs as beam splitters for chiral edge states. The Mach–Zehnder geometry allows for controlled studies of quantum coherence, phase accumulation, and interference in the quantum Hall regime.

Finally, we reviewed experiments employing ultrafast voltage pulses, which open access to the time-resolved dynamics of low-dimensional electron systems. Together, the devices and probes introduced in this chapter constitute a comprehensive experimental toolbox for exploring quantum transport, coherence, and interaction effects in mesoscopic systems.

3

Theoretical and numerical methods

In this chapter, we deal with the transport properties of different systems under elastic scattering regime. The best formalism to study such systems is Landauer–Büttiker formalism. We will start with a brief review on the respective formalism, starting with introducing scattering matrix , deriving the generalized relations for the current operator, the noise and the Fano factor. We illustrate an example of modeling the scattering region with a rectangular-shaped potential and state the appropriate transport quantities for it. For a comprehensive treatment of the time-dependent extension of scattering theory, as well as an in-depth discussion of quantum transport more broadly, we refer the reader to the excellent textbook [Moskalets, 2011].

3.1 Brief: Scattering formalism

3.1.1 *Introduction*

According to Landauer–Büttiker approach [Blanter and Büttiker, 2000], the transport phenomenon in mesoscopic conducting systems can be described with the help of a corresponding quantum mechanical scattering problem. The mesoscopic system is assumed to be connected with the macroscopic contacts acting as reservoirs of electrons, which are scattered by the mesoscopic sample. After the scattering process, the electrons either return to the same contact or propagate to different one. Thus, the problem of calculating such transport characteristics as, for example, electrical and thermal current or noise is reduced to solving a quantum-mechanical scattering problem with a potential profile corresponding to the sample under consideration with possibly subsequent statistical averaging. All information concerning transport properties of a sample is encoded in its scattering matrix, $\hat{S}$.

We neglect electron-electron interactions and use the Schrödinger equation for electrons as the basic equation. In principle interactions can be easily incorporated on the mean-field level.

3.1.2 *Scattering matrix*

In quantum mechanics an electron is characterized by the wavefunction, $\Psi(t, \boldsymbol{r})$,which depends on time t and the position coordinate $\boldsymbol{r}$. The idea is that if the wave function of the incoming electron is known Ψ^{in}, then using the Schrödinger equation one can use calculate the wavefunction Ψ^{out} for a scattered electron. This raise further a question that

in order to solve the complete problem, does one need to solve the Schrödinger equation for each $\Psi_{\mathrm{j}}^{\mathrm{in}}$?

This is where the formalism of scattering matrix come to rescue. Using the scattering-matrix formalism, one needs to solve the scattering problem of incident states constituting the full orthonormal basis. Once done, using the superposition principle one can find the solution for any possible incoming scattering states.

Thus, in mathematical terms, we have the following problem at hand. We have the incoming scattering states expanded in the appropriate basis functions $\psi_\alpha^{\mathrm{in}}$ as,

$$\Psi^{\mathrm{in}} = \sum_\alpha a_\alpha \psi_\alpha^{\mathrm{in}} \tag{1}$$

The wavefunction of the scattered electron Ψ^{out}, in the appropriate basis,

$$\Psi^{\mathrm{out}} = \sum_\beta b_\beta \psi_\beta^{\mathrm{out}} \tag{2}$$

The set of functions $\psi_\alpha^{\mathrm{in}}$ and $\psi_\beta^{\mathrm{out}}$ constitute the full orthonormal basis. The problem is to establish a relation between the coefficients b_β if a_α is given. Thus, if the scattered wavefunction, $\Psi^{\mathrm{out}}$is expanded in the basis of $\Psi_\alpha^{\mathrm{out}}$, due to scattering of the initial waves, $\Psi_\alpha^{\mathrm{in}} = a_\alpha \psi_\alpha^{\mathrm{in}}$,

$$\begin{aligned} \Psi^{\mathrm{out}} &= \sum_\alpha \Psi_\alpha^{\mathrm{out}} \\ \Psi^{\mathrm{out}} &= a_\alpha \sum_\beta S_{\beta\alpha} \psi_\beta^{\mathrm{out}} \end{aligned} \tag{3}$$

The coefficients b_β for the scattered states are given as:

$$\begin{aligned} \Psi^{\mathrm{out}} = \sum_\alpha a_\alpha \sum_\beta S_{\beta\alpha} \psi_\beta^{\mathrm{out}} = \sum_\beta b_\beta \psi_\beta^{\mathrm{out}} \\ \text{where, } b_\beta = \sum_\alpha S_{\beta\alpha} a_\alpha \end{aligned} \tag{4}$$

Therefore, Eq.(4), expresses the coefficient b_β in terms of the coefficient of the incident waves. The coefficients $S_{\beta\alpha}$ are the quantum transition amplitude from the incident state Ψ^{in} to outgoing/scattered states Ψ^{out}. They are represented as a elements of a matrix $\hat{S}$, known as scattering matrix. Note, that the order of the indices is important. The followed convention is that the first index (β) corresponds to scattered state while the second index (α) corresponds to the scattering state.

3.1.3 *Generalized relations for transport quantities*

In this section, we will study the application of the scattering matrix approach to evaluate transport quantities in microscopic samples. The scattering matrix relies on the single-electron approximation. Under this approximation, the separate electrons are considered as separate independent particles which interactions with other electrons, nuclei and ions can be modeled via an effective potential energy.



(a)

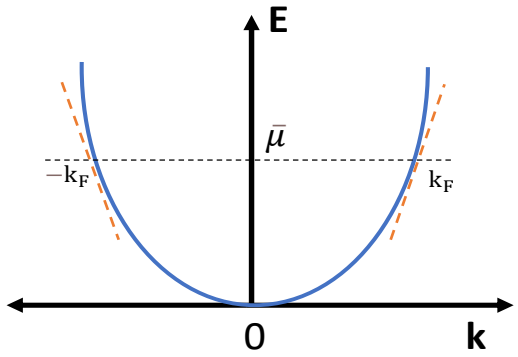

(b)

Figure 3.1: **Illustration of two-terminal scattering model.** (a) The conduction channels of injected $a_{L,k}$; $a_{R,k}$ and scattered $b_{L,k}$; $b_{R,k}$ respectively. (b) Parabolic dispersion relation in the leads. The orange dashed lines indicate the linear approximation near the Fermi surface, while the horizontal black dashed line marks the Fermi level.

Let's consider a simple two-terminal device coupled to a single conduction channel on both the left and right sides of the device. Electrons, propagating from some reservoir to the sample, enter it, are scattered inside it, and then leave it to go to the same or different reservoir. In order to calculate the relevant transport quantities, flowing between the sample and the reservoirs, we do not need to know what happens with each electrons inside the sample. It is enough to look at the incoming and the outgoing flow of the electrons.

In the case below, we deal with the following 1D scattering problem: Electrons propagating to the sample are incident, or incoming particles, while the electrons traveling away from the scattering regions are the scattered or outgoing particles. We consider the elastic scattering i.e., the energy conserving scattering. To neglect the inelastic effects, we assume the low temperatures when the phase coherence length L_ϕ is much larger than the sample size L.

Figure 3.1(a) shows a schematic of the setup. We consider the Hamiltonian for an one-dimensional free electron system, expressed in the language of creation and annihilation operators $\left(c_k^\dagger, c_k\right)$ as,

$$H = \sum_k (\epsilon_k - \mu) c_k^\dagger c_k \tag{5}$$

where, $\epsilon = \frac{\hbar^2 k^2}{2m}$ and μ is the chemical potential.

Under the linear approximation to the parabolic band dispersion around the Fermi surface, see Fig. 3.1(b),

$$\epsilon_k - \mu = \pm \hbar v_F (k \mp k_F) \tag{6}$$

Taking, $v_F = \frac{\hbar k_F}{m}$:= Fermi velocity and k_F being the wave number.

We define c_k in the following sense,

$$c_k = \begin{cases} a_k & k > 0 \\ b_k & k < 0 \end{cases} \tag{7}$$

The above introduced operators are subject to the fermionic commutation relations $\left\{a_{\alpha,k}, a^\dagger_{\alpha',k'}\right\} = \left\{b_{\alpha,k}, b^\dagger_{\alpha',k'}\right\} = \delta_{\alpha,\alpha'}\delta_{k,k'}$.

We introduce the field operator for the electron as:

$$\hat{\psi(x)} = \sum_{-\infty<k<\infty} \left(\frac{1}{\sqrt{L}}\right) e^{ikx} c_k = \sum_{k>0} e^{ikx} c_k + \sum_{k<0} e^{ikx} c_k = \sum_{k>0} \left(e^{ikx} c_k + e^{-ikx} c_{-k}\right). \tag{8}$$

In first quantization, the scattering problem in terms of wavefunction asymptotics:

$$\psi^{in}_{L,k}(x) = \begin{cases} e^{ikx} + Ae^{-ikx} & x \to -\infty \\ Be^{ikx} & x \to \infty \end{cases} \tag{9}$$

$$\psi^{in}_{R,k}(x) = \begin{cases} Ce^{-ikx} & x \to -\infty \\ e^{-ikx} + De^{ikx} & x \to \infty \end{cases} \tag{10}$$

According the second quantization formalism, we consider operators creation/annihilation operators in some quantum state. Let's consider $a^\dagger_{L,k}/a_{L,k}$ and $a^\dagger_{R,k}/a_{R,k}$ be the creation/annihilation operators for the left and the right lead respectively. The states in the left and right lead (L/R) is given by:

$$\hat{\psi_L}(x) = \left(\frac{1}{\sqrt{L}}\right) \sum_k \left(\hat{a}_{L,k} e^{ikx} + \hat{b}_{L,k} e^{-ikx}\right); \quad x < 0 \tag{11}$$

$$\hat{\psi_R}(x) = \left(\frac{1}{\sqrt{L}}\right) \sum_k \left(\hat{a}_{R,k} e^{-ikx} + \hat{b}_{R,k} e^{ikx}\right); \quad x > 0 \tag{12}$$

In the second quantization, within the asymptotic limits,

$$\hat{\psi}(x)_{x\to-\infty} = \sum_{k\geq 0} \left(\hat{a}_{L,k} e^{ikx} + \left(A\hat{a}_{L,k} + C\hat{a}_{R,k}\right) e^{-ikx}\right) \tag{13}$$

$$\hat{\psi}(x)_{x\to+\infty} = \sum_{k\geq 0} \left(e^{ikx}\left(B\hat{a}_{L,k} + D\hat{a}_{R,k}\right) + \hat{a}_{R,k} e^{-ikx}\right) \tag{14}$$

Comparing Eqs.(11,13) and Eqs.(12,14) gives,

$$\hat{b}_{L,k} = A\hat{a}_{L,k} + C\hat{a}_{R,k}$$
$$\hat{b}_{R,k} = B\hat{a}_{L,k} + D\hat{a}_{R,k}$$

In S-matrix form:

$$\begin{pmatrix} \hat{b}_{L,k} \\ \hat{b}_{R,k} \end{pmatrix} = s \begin{pmatrix} \hat{a}_{L,k} \\ \hat{a}_{R,k} \end{pmatrix} \tag{15}$$

$$\text{where, } s = \begin{pmatrix} s^{LL}(k) & s^{LR}(k) \\ s^{RL}(k) & s^{RR}(k) \end{pmatrix} = \begin{pmatrix} A & C \\ B & D \end{pmatrix} = \begin{pmatrix} r & t^{'} \\ t & r^{'} \end{pmatrix} \tag{16}$$

3.1.3.1 *Landauer formula*

Using the field operators, we write the current operator at position x in a given lead as:

$$\hat{I}(x) = \frac{\hbar e}{2im}\left(\hat{\psi}^{\dagger}(x)\frac{d\hat{\psi}(x)}{dx} - \frac{d\hat{\psi}^{\dagger}(x)}{dx}\hat{\psi}(x)\right) \tag{17}$$

Using Eq.(11), and place them in Eq.(17) for $k, k^{'}$ taken in the vicinity of k_F, the current flowing from the lead L into the sample,

$$\hat{I}_L = \hat{I}(x=0) = \frac{e}{L}\sum_{k,k^{'}}\left(\frac{2\hbar k_F}{2m}\right)\left[a^{\dagger}_{L,k}a_{L,k^{'}} - b^{\dagger}_{L,k}b_{L,k^{'}}\right]$$

$$\hat{I}_L = \frac{ev_F}{L}\sum_{k,k^{'}}\left[a^{\dagger}_{L,k}a_{L,k^{'}} - b^{\dagger}_{L,k}b_{L,k^{'}}\right] \quad ;\text{Fermi velocity: } v_F = \frac{2\hbar k_F}{2m} \tag{18}$$

Using Eq.(16), re-expressing b-operators in terms of a-operators,

$$\hat{I}_L = \frac{ev_F}{L}\sum_{\alpha=L,R}\sum_{\beta=L,R}\sum_{k,k^{'}} a^{\dagger}_{\alpha,k}A^{\alpha\beta}_{L}(k,k^{'})a_{\beta,k^{'}}$$

$$\text{where, } A^{\alpha\beta}_{L}\left(k,k^{'}\right) = \delta_{L,\alpha}\delta_{L,\beta} - [s^{L\alpha}(k)]^{*}s^{L\beta}\left(k^{'}\right) \tag{19}$$

Now, we derive the conductance formula. The incident electrons are in thermal equilibrium with the reservoirs and taking the statistical average $\langle ... \rangle$,we obtain:

$$\langle a^{\dagger}_{\alpha,k}a_{\beta,k^{'}}\rangle = \delta_{\alpha,\beta}\delta_{k,k^{'}}f_{\alpha}(k)$$

$$\text{where, } f_{\alpha}(k) = \frac{1}{exp\left[(\epsilon_k - \mu_{\alpha})/k_BT_{\alpha}\right]+1}$$

with $\alpha = L/R$, $f_{\alpha}(k)$ being the Fermi distribution in the left/right leads respectively. Hence, the average current $\langle \hat{I}_L \rangle$:

$$\langle \hat{I}_L \rangle = \frac{ev_F}{L}\sum_{\alpha=L,R}\sum_{\beta=L,R}\sum_{k,k^{'}} A^{\alpha\beta}_{L}\left(k,k^{'}\right)\langle a^{\dagger}_{\alpha,k}a_{\beta,k^{'}}\rangle$$

Performing the substitution $\frac{1}{L}\sum_k \rightarrow \int \frac{dk}{2\pi}$ and using dispersion relation (6) gives,

$$\langle \hat{I}_L \rangle = ev_F \int \frac{dk}{2\pi}\sum_{\alpha} A^{\alpha\alpha}_{L}\left(k,k^{'}\right)f_{\alpha}(k) \tag{20}$$

$$\langle \hat{I}_L \rangle = \frac{e}{2\pi\hbar}\int d\epsilon \sum_{\alpha} A^{\alpha\alpha}_{L}(\epsilon,\epsilon)f_{\alpha}(\epsilon) \tag{21}$$

and expressing $A_L^{\alpha\alpha}(\epsilon,\epsilon)$ in terms of transmission function $\mathcal{T}(\epsilon)$ (check Appendix A) gives:

$$\langle \hat{I}_L \rangle = \frac{e}{2\pi\hbar} \int d\epsilon\, \mathcal{T}(\epsilon) \left(f_L(\epsilon) - f_R(\epsilon) \right) \tag{22}$$

Equation (22) gives the general expression for the **Landauer formula**. We see that the current flowing into the lead L depends on the difference of the Fermi functions times the transmission function $\mathcal{T}(\epsilon)$. If all the reservoirs have same potential and temperatures, then the current is zero.

3.1.3.2 *Current noise*

In the last section we derived explicitly the expression for the average current. This term average current $\langle I \rangle$ implies that the fluctuations of the instantaneous current I been averaged over a time. Infact, the fluctuating current is a consequence of charge quantization. The magnitude of the fluctuations or the noise value, is characterized by:

$$\langle \delta I^2 \rangle = \langle (I - \langle I \rangle)^2 \rangle = \langle I^2 \rangle - \langle I \rangle^2 \tag{23}$$

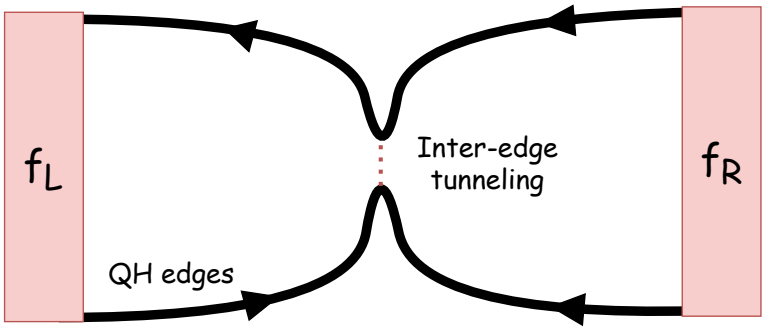

Figure 3.2: **Schematic of a two-terminal setup**. The f_L and f_R are the Fermi-distributions of the left and right reservoirs reservoirs respectively. The dots at the QPC marks the inter-edge tunneling.

Consider a two-terminal geometry as shown in Fig. 3.2. We focus on two primary sources of the noise in the mesoscopic devices. First is the **thermal noise or the Johnson-Nyquist noise**, due to finite temperature T of the reservoir. This noise exist in equilibrium. If the reservoirs of the samples are tuned to equal potentials, then the average flowing current will be zero. Nevertheless, the mean square fluctuations around the current is non-zero,

$$\frac{\langle \delta I^2 \rangle_{\text{th}}}{\Delta\nu} = 4 k_B T g_0$$

where, g_0 is the conductance of the sample, $\Delta\nu$ is a frequency bandwidth within which the current fluctuations are measured. The reason behind this fluctuations is due to the variation of the occupation states in the microscopic reservoir, hence results in the fluctuating electron flow to the scattering regions. At zero temperature, the occupation number doesn't change, therefore the thermal noise is zero.

Second is the shot noise [Blanter and Büttiker, 2000]. It was first studied by Schottky [Schottky, 1918] in context to current flows in electronic lamps. The probabilistic propagation of electrons leads to the current fluctuations. The shot noise arises due to the quantum-mechanical; probabilistic nature of scattering. The shot noise arises only in a non-equilibrium case when the current flows through the sample.

If the bias voltage V is applied to the sample the current fluctuations at zero temperature:

$$\frac{\langle \delta I^2 \rangle_{\text{sh}}}{\Delta \nu} = 2eVg_0\mathcal{T}\left(1-\mathcal{T}\right)$$

where, $\mathcal{T}$ is the transmission probability of an electrons traveling from one reservoir and being scattered to the another one. This accounts for the probabilistic nature of the shot noise. It is important to note that the two mentioned sources of noise are not independent. The presence of current changes the thermal noise and the shot noise is modified at the finite temperature. This implies that the nature of the underlying physics is same for both the thermal and the shot noise. The only difference is in the source of stochasticity — The thermal noise originate from the distribution function of the electrons while the shot noise comes from the quantum mechanical scattering processes.

Let's derive the two-terminal shot noise relation from the generalized expression [Nazarov and Blanter, 2009] of the noise for multi-terminal device:

$$S_{\alpha\beta} = \frac{e^2}{\pi\hbar}\int dE \sum_{\gamma\delta} \text{Tr}\left[\left(\delta_{\alpha\gamma}\delta_{\alpha\delta} - s^{\dagger}_{\alpha\gamma}s_{\alpha\delta}\right)\left(\delta_{\beta\gamma}\delta_{\beta\delta} - s^{\dagger}_{\beta\delta}s_{\beta\gamma}\right)\right] \times \left\{f_\gamma\left(E\right)\left[1-f_\delta\left(E\right)\right] + f_\delta\left(E\right)\left[1-f_\gamma\left(E\right)\right]\right\} \quad (24)$$

where the trace is taken over the transport channels. Here α/β are the respective terminals for outgoing/incoming electrons.

The noise in terms of time-averaged current operator at the frequency ω:

$$S_{\alpha\beta}\left(\omega\right) = \left\langle \hat{I}_\alpha\left(t\right)\hat{I}_\beta\left(t^{'}\right) + \hat{I}_\beta\left(t^{'}\right)\hat{I}_\alpha\left(t\right) - 2\langle I_\alpha\left(t\right)\rangle\langle I_\beta\left(t^{'}\right)\rangle\right\rangle_\omega$$

For the above setup (3.2), the corresponding S-matrix is:

$$s_{\alpha\beta} = \begin{bmatrix} s_{LL} & s_{LR} \\ s_{RL} & s_{RR} \end{bmatrix} = \begin{bmatrix} r & t' \\ t & r' \end{bmatrix} \quad (25)$$

Plugging the respective contribution using S-matrix for two-terminal setup:

$$\begin{aligned} S_{\alpha\beta} = \frac{e^2}{\pi\hbar}\int dE \Bigg[& \text{Tr}\left(\left[\delta_{LL}\delta_{LL} - s^{\dagger}_{LL}s_{LL}\right]\left[\delta_{RL}\delta_{RL} - s^{\dagger}_{RL}s_{RL}\right]\right)\left(2f_L\left(1-f_L\right)\right) \\ & + \text{Tr}\left(\left[\delta_{LL}\delta_{LR} - s^{\dagger}_{LL}s_{LR}\right]\left[\delta_{RR}\delta_{RL} - s^{\dagger}_{RR}s_{RL}\right]\right)\left(f_L\left(1-f_R\right) + f_R\left(1-f_L\right)\right) \\ & + \text{Tr}\left(\left[\delta_{LR}\delta_{LL} - s^{\dagger}_{LR}s_{LL}\right]\left[\delta_{RL}\delta_{RR} - s^{\dagger}_{RL}s_{RR}\right]\right)\left(f_R\left(1-f_L\right) + f_L\left(1-f_R\right)\right) \\ & + \text{Tr}\left(\left[\delta_{LR}\delta_{LR} - s^{\dagger}_{LR}s_{LR}\right]\left[\delta_{RR}\delta_{RL} - s^{\dagger}_{RR}s_{RR}\right]\right)\left(2f_R\left(1-f_R\right)\right)\Bigg] \end{aligned}$$

Time-reversal symmetry imposes unitarity, $t = -t^{'}$, $r = -r^{'}$ gives $s^{\dagger}_{LL}s_{LL} = |r|^2 = R$, $s^{\dagger}_{RL}s_{RL} = |t|^2 = \mathcal{T}$:

$$S_{\alpha\beta} = \frac{e^2}{\pi\hbar}\int dE\Big[(1-R)(-\mathcal{T})(2f_L(1-f_L)) + 2R\mathcal{T}(f_L+f_R-2f_Lf_R) + (-\mathcal{T})(1-R)(2f_R(1-f_R)) \quad (26)$$

gives the **shot-noise expression for two-terminal setup**:

$$S_{\alpha\beta} = \frac{e^2}{\pi\hbar}\int dE\left[\mathcal{T}(f_L+f_R-2f_Lf_R) - \mathcal{T}^2\left(f_L^2+f_R^2-2f_Lf_R\right)\right] \quad (27)$$

3.1.3.3 *Fano factor*

The Fano factor, F, is the ratio of the excess noise to the direct current times the charge of the carriers [Blanter and Büttiker, 2000].

$$F = \frac{S_{\text{excess}}}{2e\langle I\rangle} = \frac{S(V)-S(0)}{2e\langle I\rangle} \quad (28)$$

Schottky [Schottky, 1918] showed that for statistically independent carriers the Fano factor is unity. In the presence of correlation and interaction the Fano factor is usually less than unity.

One can infer from Eq.(22) that even for the simplest case, $\mathcal{T}(E) = \text{constant} = \mathcal{T}_0$ and $eV \gg k_BT$, the Fano factor:

$$F = \frac{S_{\text{excess}}}{2e\langle I\rangle} \sim \frac{\mathcal{T}_0(1-\mathcal{T}_0)}{\mathcal{T}_0} = (1-\mathcal{T}_0) \quad (29)$$

As $\mathcal{T}_0 \to 0$, the Fano factor $F \sim 1$. Thus, one can say that in case of small conductance $g/g_0 = \mathcal{T}_0 \ll 1$, the current is carried by statistically independent particles.

As the conductance increases, the Fano factor decreases due to correlations between the electrons. These correlations are a consequence of the Pauli exclusion principle forcing electrons to pass trough a lead one by one.

3.1.4 *Illustration: Rectangular barrier potential*

In this section, we model the scattering region with a rectangular barrier and derive the transport quantities in the constant transmission limit. For two-terminal geometry, we demonstrate the use of scattering formalism to evaluate current, noise and the Fano factor. First, let's consider a rectangular shaped potential with the potential height V_0 and length of the potential region a, as shown in Fig. 3.3. The potential profile is given as:

$$V(x) = \begin{cases} 0 & , x < \frac{a}{2} \\ V_0 & , x \in \left(-\frac{a}{2}, \frac{a}{2}\right) \\ 0 & , x > \frac{a}{2} \end{cases}$$

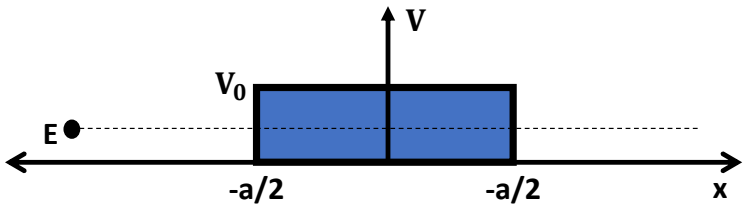

Figure 3.3: **Rectangular barrier.**

The transmission function of the rectangular barrier:

$$\mathcal{T}(E) = \frac{1}{\left[1 + \frac{\sinh^2\left(\sqrt{\frac{V_0}{\hbar^2/2ma^2}\left(1-\frac{E}{V_0}\right)}\right)}{4\left[\frac{E}{V_0}\left(1-\frac{E}{V_0}\right)\right]}\right]} \tag{30}$$

where, $\hbar$ is the reduced Plank's constant and m_e is the mass of the electron. Let's define the constant transmission as $\mathcal{T}(E = \bar{\mu}) = \mathcal{T}_{\bar{\mu}}$ as:

$$\mathcal{T}_{\bar{\mu}} = \frac{1}{\left[1 + \frac{\sinh^2\left(\sqrt{\frac{V_0}{\hbar^2/2ma^2}\left(1-\frac{\bar{\mu}}{V_0}\right)}\right)}{4\left[\frac{\bar{\mu}}{V_0}\left(1-\frac{\bar{\mu}}{V_0}\right)\right]}\right]} \tag{31}$$

This is a good approximation with low-energy excitations that occur near the Fermi energy. For the zero temperature limit, the respective Fermi distributions take the form of Heaviside function for $\bar{\mu} - \frac{eV}{2} < \epsilon < \bar{\mu} + \frac{eV}{2}$, where $V \geq 0$,

$$\begin{aligned} f_L(\epsilon) &\sim \theta\left(-\epsilon + \left(\bar{\mu} + \frac{eV}{2}\right)\right) = \begin{cases} 1 & \epsilon < \bar{\mu} + \frac{eV}{2} \\ 0 & \epsilon > \bar{\mu} + \frac{eV}{2} \end{cases} \\ f_R(\epsilon) &\sim \theta\left(-\epsilon + \left(\bar{\mu} - \frac{eV}{2}\right)\right) = \begin{cases} 1 & \epsilon < \bar{\mu} - \frac{eV}{2} \\ 0 & \epsilon > \bar{\mu} - \frac{eV}{2} \end{cases} \end{aligned} \tag{32}$$

Hence, using the Landauer formula Eq.((22)), the average current for the constant transmission is given as:

$$\langle I \rangle_{T_{\bar{\mu}}} = \frac{e}{2\pi\hbar} \int_{\bar{\mu}-\frac{eV}{2}}^{\bar{\mu}+\frac{eV}{2}} d\epsilon T_{\bar{\mu}} \left[\theta\left(-\epsilon + \left(\bar{\mu} + \frac{eV}{2}\right)\right) - \theta\left(-\epsilon + \left(\bar{\mu} - \frac{eV}{2}\right)\right)\right]$$

$$\text{which gives, } \langle I \rangle_{T_{\bar{\mu}}} = \frac{e^2 V}{2\pi\hbar} T_{\bar{\mu}} \tag{33}$$

Similarly, using the generalized noise relation in Eq.((9)), one gets,

$$S_{T_{\bar{\mu}}} = \frac{e^2}{\pi\hbar} T_{\bar{\mu}} (1 - T_{\bar{\mu}}) \int_{\bar{\mu}-\frac{eV}{2}}^{\bar{\mu}+\frac{eV}{2}} d\epsilon$$

$$\text{which gives, } S_{T_{\bar{\mu}}} = \frac{e^3 V}{\pi\hbar} T_{\bar{\mu}} (1 - T_{\bar{\mu}}) \tag{34}$$

Defining the Fano factor for constant transmission case,

$$F_{T_{\bar{\mu}}} = \frac{S_{T_{\bar{\mu}}} - S(0)}{2e\langle I \rangle_{T_{\bar{\mu}}}}$$
$$\text{which gives, } F_{T_{\bar{\mu}}} = 1 - T_{\bar{\mu}} \tag{35}$$

3.2 Numerical tools

The study of the mesoscopic quantum transport relies heavily on the efficient numerical algorithms capable of heavy complex geometries and external fields. We dedicate the present section to introduce the used numerical algorithms, namely KWANT and TKWANT, for simulating transport in time-dependent and time-independent domain. For further details, kindly refer to [Groth et al., 2014, Kloss et al., 2021].

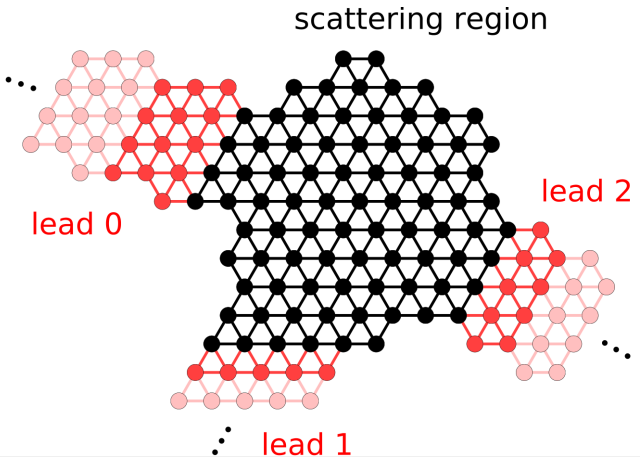

Figure 3.4: **Tight-binding system modeled with KWANT**. The scattering region is represented by black dots (sites), while the sites belonging to the semi-infinite leads is by red dots. Leads consist of an infinite sequence of interconnected identical unit cells. In this figure, the unit cells of a lead are drawn with different shade. Only the first two are shown for each lead. The figure is adapted from [Groth et al., 2014, Kloss et al., 2021].

KWANT is an open-source Python package for numerical quantum transport calculations. It provides a framework to simulate tight-binding Hamiltonians on arbitrary geometries. The package also supports simulations of multi-terminal setups and computes transport properties such as conductance, transmission probabilities, wavefunctions, and local densities. Transport is formulated using the scattering formalism, where a system is divided into a scattering region that is then attached to semi-infinite leads, as shown in Fig. 3.4. Electrons originating from the leads are scattered through the region, and all information about the respective transport quantities can be evaluated through the scattering matrix.

A focus application of KWANT in the present thesis is on simulating quantum Hall samples (more in next subsection). For such settings, the external magnetic field is incorporated via the Peierls substitution, where hopping elements acquire a phase proportional to the magnetic flux. This modification leads to the quantization of Landau levels and the formation of 1D chiral edge states, which are a distinctive signature of

the quantum Hall effect. Additionally, KWANT facilitates simulations of more exotic topological systems, such as graphene, honeycomb, and kagome lattices.

However, while KWANT is well-suited for problems involving stationary transport, many interesting time-dependent phenomena lie beyond this regime. In particular, phenomena involving time-dependent driving, such as voltage pulses in the context of electronic optics, cannot be captured. Therefore, the stationary scattering framework is insufficient to describe transient dynamics. To overcome such challenges, the extension TKWANT has been developed.

TKWANT directly builds on the framework of KWANT but incorporates time-dependent Hamiltonians. This package simulates any KWANT-defined tight-binding system supplemented by time-dependent terms, such as a time-dependent bias voltage applied at the interface between the leads and the scattering region.

The application we focus on is the simulation of voltage pulses propagating through the sample. In such a setup, the lead-sample interface is subjected to a time-dependent voltage profile— such as a Lorentzian pulse, Gaussian pulse, etc. The injected wave then propagates across the sample, undergoes scattering, and emerges through other leads.

TKWANT helps compute time-resolved observables, such as transient currents, charge densities, and local wavefunctions, thus offering insight into the dynamics of the propagating charge pulse across the sample.

In the upcoming chapters, we will demonstrate the simulations of KWANT and TKWANT respectively.

Part II

MODELLING OF A QUANTUM POINT CONTACT

4

Quantum Hall edge modes: KWANT

"The theory of quantum mechanics is now complete. The underlying physical laws necessary for the mathematical theory of a large part of physics and the whole of chemistry are thus completely known."

Paul Dirac

In this chapter, we illustrate the properties of edge states using KWANT package. We consider two types of systems: (i) a closed sample, corresponding to an isolated system without any attached leads, and (ii) open structured samples – the samples with the gate potentials in between and leads are attached.

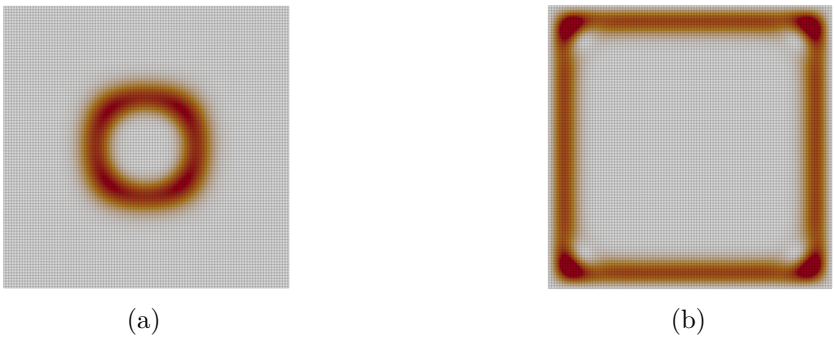

(a) (b)

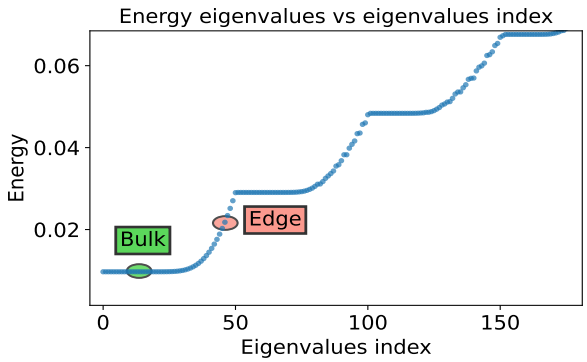

(c)

Figure 4.1: **Numerics for closed sample**. **(a)** The bulk wavefunction as marked in (c). **(b)** The edge wavefunction as marked in (b). **(c)** Energy eigenvalue spectrum. The stairs represent the corresponding Landau levels.

For each case, we show the KWANT visualization of the spatial distribution of the wavefunction modes for the closed and the open system. This embarks the utility of KWANT in demonstrating as a effective tool to analyses QH systems in the later chapters.

4.1 Closed sample

We begin with the closed, isolated system, studied using the KWANT package (see previous chapter for methodological details in section 3.2). Parameters representative of typical QPC setups are chosen. The electron density is set to $n_s = 1 \times 10^{15}\,\mathrm{m}^{-2}$. Given the effective mass $m^* = 0.067 m_e$ (with m_e is the bare electron mass), the filling factor $\nu = 1$ is achieved for the magnetic field $B = 4.14\,\mathrm{T}$, which further sets the magnetic length $l_B = 12.6\,\mathrm{nm}$ and the cyclotron energy $E_c = \hbar\omega_c = 7.17\,\mathrm{meV}$.

For the numerical simulations, the following parameters are used: lattice constant $(a = 1)$, hopping parameter $(t = 1)$, system size $(L_x \times L_y) = (180 \times 180)$. The Hamiltonian matrix is diagonalized, and its eigenvalues reveal the quantized Landau levels.

The visualization of representative wavefunctions from the bulk and from the edge are shown in Fig. 4.1(a,b). The corresponding eigenvalues are marked on the energy spectrum. The steps of the plateau has the bulk wavefunction while the transition points between the two corresponding plateaus denotes the edge wavefunctions as shown in Fig. 4.1(c). As one progresses through the eigenvalues, bulk-like wavefunctions are observed, which gradually evolve into edge-localized states. Upon reaching the second Landau level, however, the wavefunctions collapse back to bulk-like character before again developing into edge states associated with that Landau level.

4.2 Open sample

Finally, we consider the propagation of edge states in the presence of two gate potentials of width $75a$ (a is the lattice constant). When the two gates are placed sufficiently close together, reflection of the edge mode is observed, as shown in Fig. 4.2.

The analysis presented here serves to demonstrate the qualitative features of edge state dynamics in gated structures.

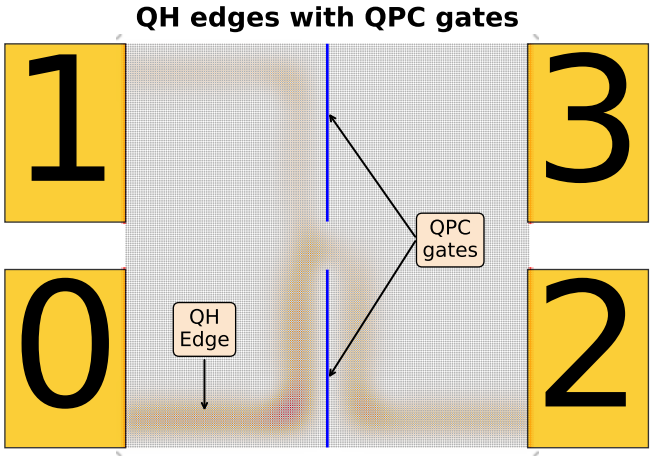

Figure 4.2: Quantum Hall edge with full gates in between and two contacts attached.

In the upcoming chapters (5 and 6), we study the proposed models analytically. A more detailed numerical investigation, including systematic studies of the local density of states and transmission characteristics, will be carried out in the following chapters.

5

Models

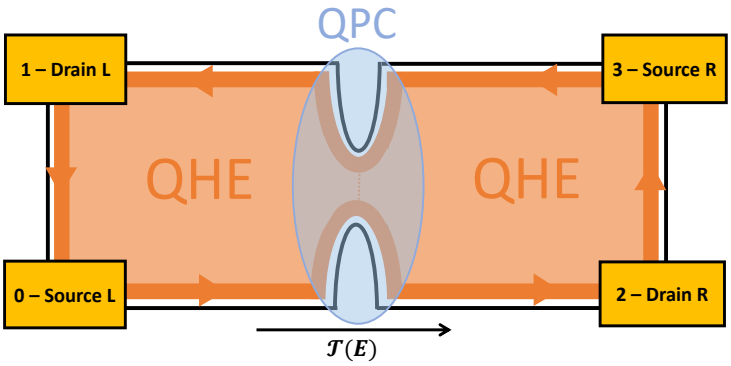

Figure 5.1: **Four-terminal setup of a quantum Hall QPC experiment**. The quantum Hall bulk supports a single chiral edge channel going around the sample (we focus on $\nu = 1$ integer quantum Hall regime). The edges from the opposite sides of the sample approach each other in one location — this is the QPC. Four Ohmic contacts are present in the sample, two (sources) are used to inject current into the chiral edge, two (drains) are used to extract the current that has passed through the QPC region. The key object for this paper's consideration is the energy-dependent transmission probability $\mathcal{T}(E)$: the probability for an excitation to be transmitted through the QPC without jumping to the other edge channel.

In the initial chapters, we introduced the quantum point contacts (see subsection 2.2). QPCs are the building units of the mesoscopic devices which been extensively studied over past many years. Despite that the experiments with a single QPC often show discrepancies with theoretical predictions: they agree at small values of the bias voltage, while at larger values (eV larger than the system temperature, $k_{\mathrm{B}}T$, yet significantly smaller than the bulk gap) they show noticeable disagreement [Saminadayar et al., 1997, de Picciotto et al., 1997]. With QPC being such an important instrument, it is crucial to understand the origin of these discrepancies in order to understand the instrument's limitations.

One of the possible explanation for the discrepancies is the energy dependence of the tunnelling amplitude. This dependence is generally expected to be highly non-universal: it may depend on the QPC geometry, impurities present in the sample etc. Here we attempt to investigate the energy dependence of tunnelling from basic theoretical considerations.

Figure 5.1 shows the basic setup for QPC experiments: The edges are in contact in a restricted region of space. The tunnelling is investigated by injecting current at source contacts and measuring the output current and noise at the drain contacts. In the conventional model, Fig. 5.2, the tunnelling is assumed to happen at a single point described by an energy-independent tunnelling amplitude. This point-QPC model is

the standard model for describing QPCs in the quantum Hall effect [Wen, 1991, 2004, Levkivskyi, 2012].

In this work, we introduce two models that account for different aspects of the realistic geometry of the QPC. The wide-QPC model shown in Fig. 5.4 accounts for an extended width of the QPC — the distance along which the two edges are in contact with each other. The long-QPC model shown in Fig. 5.6 accounts for the fact that the tunnelling amplitude originates from a finite bulk gap and for a finite distance between the two edges, and models the effective tunnelling barrier between the edges. The long-QPC model essentially models a small piece of the quantum Hall bulk in the spirit of the wire construction [Teo and Kane, 2014].

Throughout the chapter, we focus on $\nu = 1$ integer quantum Hall regime. We investigate the predictions of above two models and show that they predict drastically distinct energy dependences of the tunnelling behaviour. We compare the predictions of these models with those of the point-QPC model and with each other. We also provide their predictions for a number of transport quantities that can be measured.

Let's introduce the setup of quantum Hall QPC experiments. We focus on the case of $\nu = 1$ integer quantum Hall regime and remind the reader how the Landauer–Büttiker formalism for transport in non-interacting mesoscopic systems applies to this system. The complete overview of the Landauer–Büttiker formalism is presented in Chapter 3. We define the transmission function $\mathcal{T}(E)$, the key object for our consideration in the next sections.

The typical (four-terminal) setup of a quantum Hall QPC experiment is shown in Fig. 5.1. The sources are used to inject current into the chiral edge, as the drains are used to extract the current that has passed through the QPC region. The Landauer–Büttiker formalism [Martin and Landauer, 1992], requires the knowledge of the scattering matrix that describes the probability amplitudes of electrons emitted by one contact to arrive at a different contact:

$$\mathcal{S} = \begin{pmatrix} 0 & 1 & 0 & 0 \\ r_L & 0 & 0 & t_R \\ t_L & 0 & 0 & r_R \\ 0 & 0 & 1 & 0 \end{pmatrix} \begin{bmatrix} 0 - \text{Source L} \\ 1 - \text{Drain L} \\ 2 - \text{Drain R} \\ 3 - \text{Source R} \end{bmatrix} \tag{1}$$

The above matrix involves the amplitudes $t_{R/L}(E)$ for an electron to be transmitted through the QPC without changing its edge and $r_{R/L}(E)$ for it to be reflected to the other edge. Unitarity of the S-matrix implies $|t_L(E)|^2 + |r_L(E)|^2 = 1$ and $|t_R(E)|^2 + |r_L(E)|^2 = 1$, from which it follows that $|t_R(E)|^2 = |t_L(E)|^2$. The probability of being transmitted, $\mathcal{T}(E) = |t_L(E)|^2 = |t_R(E)|^2$, is called the transmission function.

We focus on the DC current I_2 extracted from Drain R, as well as the low-frequency noise of that current,

$$S_{22} = \left\langle \hat{I}(t)\hat{I}(t') + \hat{I}(t')\hat{I}(t) - 2\langle \hat{I}(t)\rangle\langle \hat{I}(t')\rangle \right\rangle_{\omega} \tag{2}$$

We focus on the DC current I_2 extracted from Drain R, as well as the low-frequency noise of that current S_{22}. The Landauer–Büttiker formalism gives,

$$I_2 = \frac{e}{2\pi\hbar} \int dE\ \mathcal{T}(E) \left(f_{\mathrm{L}}(E) - f_{\mathrm{R}}(E)\right), \tag{3}$$

$$S_{22} = \frac{e^2}{\pi\hbar}\int dE \left\{ f_{\rm eq}(E)\left(1-f_{\rm eq}(E)\right) + \right.$$
$$+\mathcal{T}^2(E) f_{\rm L}(E)\left(1-f_{\rm L}(E)\right) + \left(1-\mathcal{T}(E)\right)^2 f_{\rm R}(E)\left(1-f_{\rm R}(E)\right) +$$
$$\left.\mathcal{T}(E)\left(1-\mathcal{T}(E)\right) f_R(E)\left(1-f_L(E)\right) + \mathcal{T}(E)\left(1-\mathcal{T}(E)\right) f_L(E)\left(1-f_R(E)\right)\right\} \quad (4)$$

Here, we assumed that the L and R sources are described by Fermi distributions $f_{\rm L}(E) = f(E-\mu_{\rm L})$ and $f_{\rm R}(E) = f(E-\mu_{\rm R})$, while the drains are in equilibrium with the sample and are defined by the equilibrium distribution$f_{\rm eq}(E) = f(E-\mu)$, where $f(E) = \left(1+e^{E/(k_{\rm B}T)}\right)^{-1}$. In what follows, we set $\mu = 0$.

Often the approximation of constant transmission is employed: $\mathcal{T}(E) = \mathcal{T}_0$ [Wen, 1991, 2004, Levkivskyi, 2012]. In this case, the above expressions simplify to:

$$I_2|_{\mathcal{T}\equiv\mathcal{T}_0} = \frac{e^2V}{2\pi\hbar}\mathcal{T}_0, \quad (5)$$

$$S_{22}|_{\mathcal{T}\equiv\mathcal{T}_0} = \frac{e^2}{\pi\hbar}\left[2k_BT + eV\mathcal{T}_0\left(1-\mathcal{T}_0\right)\left(\coth\left(\frac{eV}{2k_{\rm B}T}\right) - \frac{2k_{\rm B}T}{eV}\right)\right] \quad (6)$$

Here we have taken $\mu_{\rm L} - \mu_{\rm R} = eV$ to be the bias voltage across the QPC.

Experiments often see behaviour consistent with Eqs.(5,6) for small enough V, whereas at larger V deviations for this behaviour are observed. One of the possible explanations is that the dependence of $\mathcal{T}(E)$ on the energy becomes important at larger values of the bias voltage. Below, we introduce several models, based on general considerations and investigate the dependence $\mathcal{T}(E)$ they predict, as well as its effect on I_2 and S_{22}.

5.1 Analytical models of QPC

In the previous section, we defined the key object for our consideration: the QPC transmission $\mathcal{T}(E)$. Here we introduce a number of phenomenological models that allow for predicting the energy dependence of $\mathcal{T}(E)$. We start by reminding the reader the standard point-QPC model. We then introduce two models that account for different aspects of the realistic geometry of the QPC: wide QPC and long QPC. We explain their physical meaning and calculate the $\mathcal{T}(E)$ for each of the models.

5.1.1 *Point model*

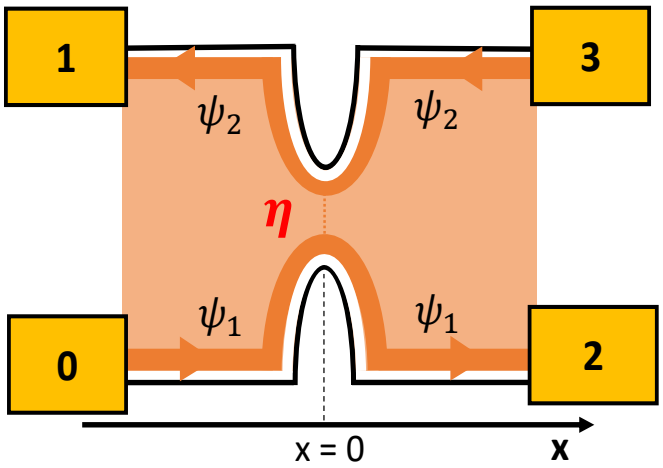

Figure 5.2: **Point-QPC model.** Two counter-propagating chiral edge modes approach each other at a single point, x=0, which allows for tunnelling of excitations between the edge modes.

The standard model of QPC [Wen, 1991, 2004, Levkivskyi, 2012] assumes that tunnelling between the two edges happens at a single point, cf. 5.2. The model is described by the Hamiltonian:

$$\mathrm{H}_{\mathrm{pqpc}} = \mathrm{H}_{\mathrm{edge}} + \mathrm{H}_{\text{tun-point}}, \tag{7}$$

$$\mathrm{H}_{\mathrm{edge}} = \int_{-\infty}^{+\infty} dx \left(-i\psi_1^\dagger v\partial_x\psi_1 + i\psi_2^\dagger v\partial_x\psi_2\right), \tag{8}$$

$$\mathrm{H}_{\text{tun-point}} = \eta\Big(\psi_1^\dagger\left(x=0\right)\psi_2\left(x=0\right) + \mathrm{h.c.}\Big). \tag{9}$$

The edge Hamiltonian $\mathrm{H}_{\mathrm{edge}}$ describes chiral fermionic channels ψ_1 and ψ_2 propagating to the right and to the left respectively. The tunnelling Hamiltonian $\mathrm{H}_{\text{tun-point}}$ describes electron transport between the two edges. Solving the scattering problem for $\mathrm{H}_{\mathrm{pqpc}}$, one finds the transmission function

$$\mathcal{T}_{\mathrm{pqpc}}\left(E\right) = \mathcal{T}_{\mathrm{pqpc}}^{0\to 2} = \left(\frac{1-\frac{\eta^2}{4v^2}}{1+\frac{\eta^2}{4v^2}}\right)^2 \tag{10}$$

The reader can find the details of the derivation in Appendix B.

The above result, though standard, warrants a few comments. First, note that $\mathcal{T}_{\mathrm{pqpc}}\left(E\right)$ does not depend on energy, which renders the transport predictions (5, 6) exact for this model.

Second, one naturally expects bigger values of η to lead to bigger tunnelling (and, thus, smaller transmission) at the QPC. This intuition holds for $|\eta| \leq 2v$, at which $\mathcal{T}_{\mathrm{pqpc}}\left(E\right) = 0$ vanishes. For $|\eta| > 2v$, however, one again has $\mathcal{T}_{\mathrm{pqpc}}\left(E\right) > 0$. This indicates singular behaviour of this model, which has been previously pointed out in the context of perturbative calculations [Filippone and Brouwer, 2016]. The wide-QPC and long-QPC models considered below regularize this behaviour *in distinct ways*. We will discuss this in more detail in Sec. 5.3.

5.1.2 *Wide model*

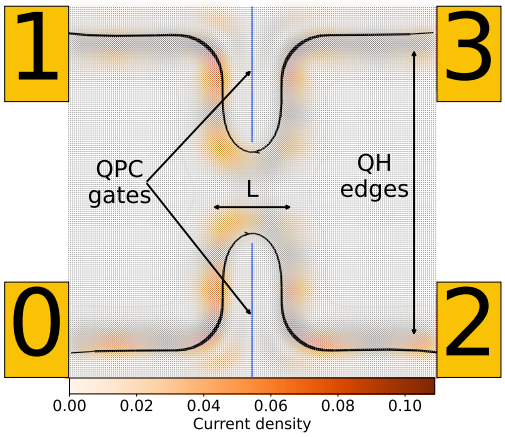

Figure 5.3: **Numerical simulation of a QPC geometry with narrow QPC-defining gates**. The figure presents the current density of QH edges in a sample that has four leads and a QPC defined by infinite potential on narrow gates (blue lines). The sample is modelled as 180x180 lattice, and the QPC-defining potential is applied to regions of 1-site width and 70-site length. The red density map represents the current density of two edge states. The edge states go around the gated regions smoothly, so that the tunnelling would happen over a finite QPC width of a few magnetic lengths. This motivates our wide-QPC model shown in Fig. 5.5. The simulation has been performed using KWANT package [Groth et al., 2014].

In the previous section, we presented the conventional point-contact (point-QPC) model. A key assumption of the point-QPC model is that tunneling occurs at a single spatial point. However, quantum point contacts in real samples inevitably possess a finite tip width. Moreover, even in the most narrowly constructed QPCs, opposite QH edges are in contact over a width of the order of the magnetic length $l_B = \sqrt{\hbar/(eB)}$, as exemplified in Fig. 5.3. This challenges the point-like approximation and warrants an investigation of the effects of the finite width of the QPC.

To this end, we introduce the wide-QPC model, which incorporates a finite-width tunneling region between the chiral QH edge channels (Fig. 5.4).

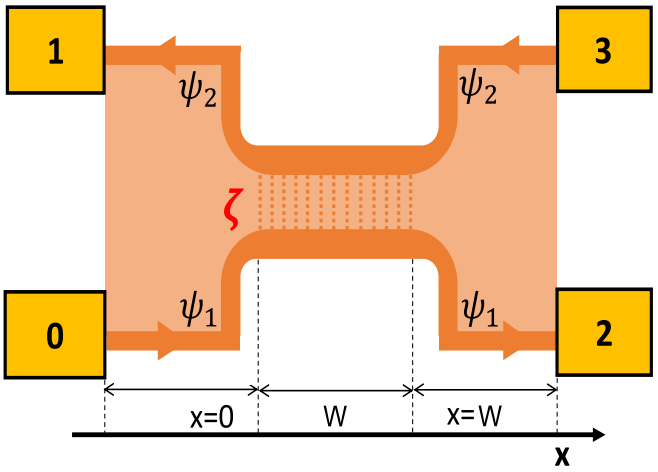

Figure 5.4: **Wide-QPC model**. Two chiral edge channels undergo tunneling over a finite region of width W.

In this model, the two edge states, ψ_1 and ψ_2 propagate in opposite directions, as in Fig. 5.2. However, the tunnelling happens over edge length L, and the tunnelling amplitude is ζ:

$$\mathrm{H}_{\mathrm{wqpc}} = \mathrm{H}_{\mathrm{edge}} + \mathrm{H}_{\mathrm{tun\text{-}wide}} \tag{11}$$

$$\mathrm{H}_{\mathrm{edge}} = \int_{-\infty}^{+\infty} dx \left(-i\psi_1^\dagger v\partial_x\psi_1 + i\psi_2^\dagger v\partial_x\psi_2\right), \tag{12}$$

$$\mathrm{H}_{\mathrm{tun\text{-}wide}} = \zeta \int_0^L dx \left(\psi_1^\dagger(x)\,\psi_2(x) + \mathrm{h.c.}\right) \tag{13}$$

Solving the scattering problem for $\mathrm{H}_{\mathrm{wqpc}}$ (see Appendix C for derivation), one finds the transmission function for wide-QPC model ($\mathcal{T}^{\mathrm{wqpc}}_{0\to 2}$) as:

$$\mathcal{T}_{\mathrm{wqpc}}(E) = \mathcal{T}^{0\to 2}_{\mathrm{wqpc}} = \frac{1}{1+\Xi(E,\zeta,W)},$$
$$\text{where, } \Xi(E,\zeta,W) = \frac{\sinh^2\left(\frac{\zeta W}{v}\sqrt{1-\left(\frac{E}{\zeta}\right)^2}\right)}{\left(1-\left(\frac{E}{\zeta}\right)^2\right)} = \frac{\sin^2\left(\frac{\zeta W}{v}\sqrt{\left(\frac{E}{\zeta}\right)^2-1}\right)}{\left(\left(\frac{E}{\zeta}\right)^2-1\right)}. \tag{14}$$

Note that unlike in the case of point-QPC model, here the transmission depends on energy.

The typical scale for the energy is the tunnelling amplitude ζ , whereas the overall behaviour of the transmission is determined by the dimensionless parameter $\zeta W/v$. Indeed, at $\mathcal{T}_{\mathrm{wqpc}}(E=0) = \left[1+\sinh^2\left(\frac{\zeta W}{v}\right)\right]^{-1}$. At large energies, the transmission is perfect: $\mathcal{T}_{\mathrm{wqpc}}(|E|\gg\zeta) = 1$. At the characteristic scale, $\mathcal{T}_{\mathrm{wqpc}}(|E|=\zeta) = \left[1+\left(\frac{\zeta W}{v}\right)^2\right]^{-1}$.

The behaviour of $\mathcal{T}_{\mathrm{wqpc}}(E)$ at various values of $\zeta W/v$ is shown in Fig. 5.5. Several aspects are worth noting. The strength of energy dependence of $\mathcal{T}_{\mathrm{wqpc}}(E)$ varies with $\zeta W/v$ in a non-trivial way. In particular, for $|E|>\zeta$, $\mathcal{T}_{\mathrm{wqpc}}(E)$ oscillates, cf. Eq.(14). The oscillation frequency, however, depends on $\zeta W/v$ and is only noticeable for large $\zeta W/v$ in Fig. 5.5.

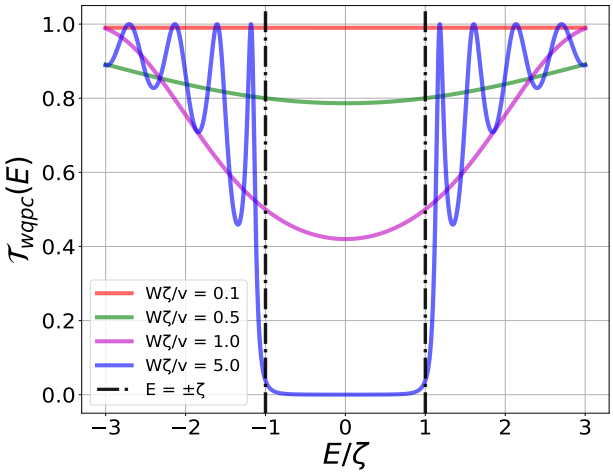

Figure 5.5: The dependence of $\mathcal{T}_{\text{wqpc}}(E)$ on energy for various values of $\zeta W/v$. The value of the dimensionless parameter $\zeta W/v$ determines $\mathcal{T}_{\text{wqpc}}(E=0)$. At $|E| \to \infty$, the transmission becomes perfect, $\mathcal{T}_{\text{wqpc}}(E) \to 1$. Oscillatory behaviour for $|E| > \zeta$ strongly depends on $\zeta W/v$.

5.1.3 *Long model*

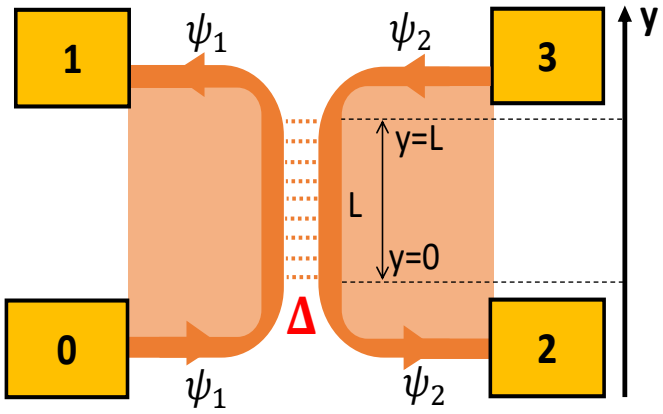

Figure 5.6: **Long QPC model**. In order to model the tunnelling barrier created by the bulk gap inside the QPC (cf. Fig. 5.1), we model the bulk in the spirit of the wire construction. The region of strong electron tunnelling (amplitude Δ) across the region devoid of electrons is topologically equivalent to the bulk of the quantum Hall sample.

In the models considered above (point QPC and wide QPC), the tunnelling amplitude between the edges was treated as a phenomenological parameter. However, the intuition based on quantum mechanics tells that the tunnelling arises from a barrier that makes it energetically costly for quasiparticles to be between the two edges in the QPC. This barrier may govern the energy dependence of the tunnelling amplitude, and thus of the transmission probability $\mathcal{T}(E)$.

In order to model this dependence, we model the QH bulk inside the QPC in the spirit of the wire construction [Teo and Kane, 2014]. In its general form, the wire construction models the QH bulk as a 1D array of one-dimensional wires with appropriate tunnelling processes between them. Here we use a minimalistic model, framing the QPC

as two edges, between which electrons tunnel across a depleted region, cf. Fig. 5.6. The tunnelling amplitude Δ corresponds to the bulk gap, and the length of the tunnelling region L corresponds to the distance between the edges on the different sides of the QPC, cf. Fig. 5.1 — these parameters have been notably absent from the point- and wide-QPC models. While here we consider the example of integer QH effect, the generalization of this model for the fractional QH effect would reflect the famous duality of weak quasiparticle tunnelling and strong electron tunnelling [Wen, 2004, Fendley et al., 1995a,b].

The Hamiltonian for the long-QPC model is:

$$\mathrm{H}_{\mathrm{lqpc}} = \mathrm{H}_{\mathrm{edge}} + \mathrm{H}_{\text{tun-long}}, \tag{15}$$

$$\mathrm{H}_{\mathrm{edge}} = \int_{-\infty}^{+\infty} dy \left(-i\psi_1^\dagger v \partial_y \psi_1 + i\psi_2^\dagger v \partial_y \psi_2 \right), \tag{16}$$

$$\mathrm{H}_{\text{tun-long}} = \Delta \int_0^L dy \left(\psi_1^\dagger (y)\, \psi_2 (y) + \mathrm{h.c.} \right). \tag{17}$$

Note that the Hamiltonian for the long-QPC model is formally identical exhibits a structural similarity to that of the wide-QPC model, Eqs.(11–13). The two Hamiltonians differ primarily by the substitutions $x \to y$ and $\zeta \to \Delta$, which reflects the conceptual difference between the models.

Most importantly, the models differ by the connection of ψ_1 and ψ_2 to different Ohmic contacts, cf. Figs. (5.4 and 5.6).

This enables us to reuse the solution of the wide-QPC model (14), while accounting for these distinctions:

$$\begin{aligned} \mathcal{T}_{\mathrm{lqpc}}(E) &= \mathcal{T}_{\mathrm{lqpc}}^{0\to 2} = 1 - \mathcal{T}_{\mathrm{lqpc}}^{0\to 1} \\ &= 1 - \mathcal{T}_{\mathrm{wqpc}}^{0\to 2}\Big|_{\substack{\zeta \to \Delta \\ W \to L}} = \frac{\Xi(E,\Delta,L)}{1+\Xi(E,\Delta,L)}, \\ \text{where } \Xi(E,\Delta,L) &= \frac{\sinh^2\left(\frac{L\Delta}{v}\sqrt{1-\left(\frac{E}{\Delta}\right)^2}\right)}{\left(1-\left(\frac{E}{\Delta}\right)^2\right)} = \frac{\sin^2\left(\frac{L\Delta}{v}\sqrt{\left(\frac{E}{\Delta}\right)^2-1}\right)}{\left(\left(\frac{E}{\Delta}\right)^2-1\right)}. \end{aligned} \tag{18}$$

Similarly to the wide-QPC model and in contrast to the standard point-QPC model, the transmission function in the long-QPC model explicitly depends on energy. However, the nature of the dependence is drastically different as compared to the wide-QPC model.

Indeed, the transmission is maximum at $E = 0$ and goes to zero at large energies, $\mathcal{T}_{\mathrm{lqpc}}(|E| \gg \Delta) = 0$, cf. Fig. 5.6. This is natural as for $|E| \ll \Delta$ the quasiparticles are unlikely to tunnel across the QPC, and are likely to be transmitted. Conversely, for $|E| \gg \Delta$, the bulk gap does not present a significant obstacle for quasiparticles to travel to a different edge. Of course, our crude model does not capture all the important aspects of the QH bulk, notably its disordered nature. However, our model does capture the concept of the tunnelling barrier.

The value of transmission $\mathcal{T}_{\mathrm{lqpc}}(E=0) = \left[1+\sinh^{-2}\left(\frac{L\Delta}{v}\right)\right]^{-1}$ is controlled by the dimensionless parameter $L\Delta/v$ that captures the barrier height Δ and length L. We do

not expect our model to be valid beyond $|E| = \Delta$, where proper bulk modelling needs to be performed. At this energy scale, $\mathcal{T}_{\text{lqpc}}(|E| = \Delta) = \left[1 + \left(\frac{L\Delta}{v}\right)^{-2}\right]^{-1}$.

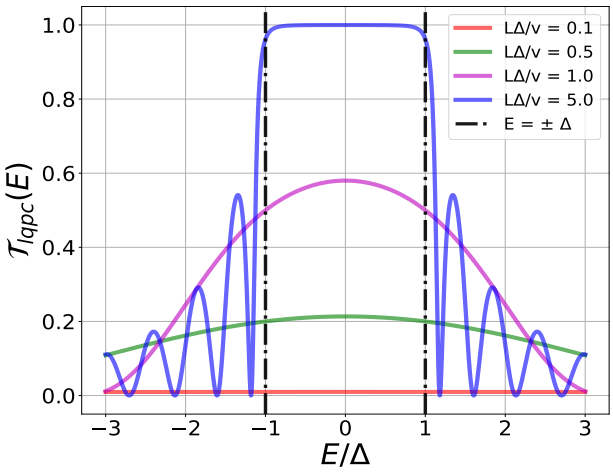

Figure 5.7: The dependence of $\mathcal{T}_{\text{lqpc}}(E)$ on energy for various values of $L\Delta/v$. The dimensionless parameter $L\Delta/v$ is associated to the "area of the tunnelling barrier", $L\Delta$. Its value determines $\mathcal{T}_{\text{lqpc}}(E = 0)$. At $|E| \to \infty$, the transmission decays to zero, $\mathcal{T}_{\text{lqpc}}(E) \to 0$. The vertical black lines $E = \pm\Delta$, marks the magnitude of the bulk gap Δ ; we do not expect our model to be valid beyond this energy scale.

5.2 Point-QPC limit

The models introduced in the previous section can be viewed as generalizations of the point-QPC model, incorporating aspects of realistic QPC setups. The wide- and long-QPC models allow a parameter regime $(L \to 0)$ that reduces them back to the point-QPC geometry. It is natural to expect the predictions for $\mathcal{T}(E)$ to reduce to those of the point-QPC model in this limit. Below we show that this is not the case, which points at the singularity of the point-QPC model.

Consider the wide-QPC model. Taking the limit $W \to 0$, $\zeta \to \infty$ such that $\zeta W =$ const, the Hamiltonian of the wide-QPC model (11–13) reduces to that of the point-QPC model (7–9) with $\eta_{\text{wqpc}} = \zeta W$. Taking the limit for the transmission function (14) yields,

$$\mathcal{T}_{\text{wqpc}}(E) = \mathcal{T}_{\text{wqpc}}^{(\text{point limit})} = \frac{1}{1 + \sinh^2\left(\frac{\eta_{\text{wqpc}}}{v}\right)}. \tag{19}$$

Compare this to $\mathcal{T}_{\text{pqpc}}(E)$ in Eq.(10). Both expressions predict no energy dependence of the transmission function and both predict $\mathcal{T}(E) \approx 1 - \eta^2/v^2$ for $|\eta| \ll v$. However, for η comparable or larger than v, the models yield drastically different predictions, despite having the identical Hamiltonian in this limit. In particular, the point-QPC model predicts $\mathcal{T}_{\text{pqpc}}(E) = 0$ at $\eta = 2v$ and $\mathcal{T}_{\text{pqpc}}(E) = 1$ at $\eta \to \infty$. At the same time, $\mathcal{T}_{\text{wqpc}}^{(\text{point limit})}$ is monotonous with respect to η_{wqpc} and vanishes for $\eta_{\text{wqpc}} \to \infty$.

The long-QPC model also features a point limit $L \to 0$, $\Delta \to \infty$ such that $L\Delta =$ const. In this limit, its Hamiltonian (15–17) reduces to that of the point-QPC model (7–9) with

$\eta_{\text{long}} = L\Delta$. However, the roles of the contacts 1 and 2 are interchanged compared to the wide- and point-QPC models, cf. Figs. (5.2,5.4,5.6). Taking the limit for the transmission function, one gets

$$\mathcal{T}_{\text{lqpc}}(E) = \mathcal{T}_{\text{lqpc}}^{(\text{point limit})} = \frac{\sinh^2\left(\frac{\eta_{\text{lqpc}}}{v}\right)}{1+\sinh^2\left(\frac{\eta_{\text{lqpc}}}{v}\right)}. \tag{20}$$

Again, this predicts an energy-independent transmission function in the point limit, yet does not match $\mathcal{T}_{\text{pqpc}}^{0\to 1} = 1 - \mathcal{T}_{\text{pqpc}}^{0\to 2}$ in its dependence on η , see Eq.(10).

This shows that the point-QPC model (7–9) is ill-defined: depending on the regularization of the point tunnelling, the model produces different results. This has, in fact, been highlighted before in Ref. [Filippone and Brouwer, 2016].

These results are in stark contrast to the case of point barrier in the conventional quantum mechanics for $p^2/(2m)$ dispersion relation, where the transmission across the delta-barrier is reproduced by taking the point limit of a rectangular potential, see Appendix D. It may be interesting to investigate in the future whether incorporating the curvature of the dispersion relation into the model (i.e., the terms $\sim \psi_i^\dagger \partial_x^2 \psi_i$) would eliminate the singularity of the point-QPC model.

5.3 Model predictions

Above, we have defined three distinct QPC models and derived their predictions for the transmission function $\mathcal{T}(E)$. In this section, we compare these models using experimentally realistic parameters. In Sec.(5.3.1), we compare their predictions for the transmission functions. In Sec.(5.3.2), we show how these predictions translate to experimentally observable quantitites.

5.3.1 *Model comparison with realistic parameters*

Above, we have derived the energy dependence of the transmission function $\mathcal{T}(E)$ as predicted by the point-QPC, wide-QPC, and long-QPC models. These predictions exhibit qualitatively different behaviours: for the wide-QPC model, the minimum value of $\mathcal{T}(E)$ is achieved at $E = 0$, cf. Fig. 5.5, whereas in long-QPC model $E = 0$ corresponds to the maximum of $\mathcal{T}(E)$. Therefore, different aspect of realistic QPC geometry predict different energy dependences of $\mathcal{T}(E)$. However, what is the significance of those dependences in realistic systems? We investigate this question below.

We begin by estimating the experimental parameters appropriate for typical QPC setups. Consider a GaAs-based quantum Hall sample with an electron density $n_s = 1\times 10^{15}\,\text{m}^{-2}$. Given the effective mass $m^* = 0.067 m_e$ (with m_e is the bare electron mass), the filling factor $\nu = 1$ is achieved for the magnetic field $B = 4.14\,\text{T}$, which further sets the magnetic length $l_B = 12.6\,\text{nm}$ and the cyclotron energy $E_c = \hbar\omega_c = 7.17\,\text{meV}$.

The edge state velocity may vary depending on the sample: values of the orders $v = 10^4$–10^6 m/s have been reported depending on whether the quantum Hall edge is defined by a gate or by the boundary of the sample [McClure et al., 2009, Gurman et al., 2016, Kamata et al., 2010, Kumada et al., 2011, Kataoka et al., 2016, Nakamura et al., 2019, 2020, Weldeyesus et al., 2025]. Given that the velocity of interest for us is the

velocity inside the QPC that is typically gate-defined, we take the value on the lower end of the range, $v = 2 \cdot 10^4\ m/s$.

Given the system parameters, we can now estimate the relevant parameters of our QPC models. For the wide-QPC model, the parameters are the tunneling amplitude, ζ , and the width of the tunneling region, W.

The QPC width can hardly be smaller than a few magnetic lengths. Indeed, Fig. 5.3 shows that even for infinitely-small QPC-defining gate, the tunnelling region has the double the width of the edge wave function. With the edge wave function having the width $l_B\sqrt{2}$ [Band and Avishai, 2013, (Section 9.5.4)], we take $W = 2\sqrt{2}l_B$. The tunnelling amplitude ζ is then determined by the transmission value at zero energy, $\mathcal{T}_0 = \mathcal{T}(E = 0)$, from Eq.(14):

$$\zeta = \frac{\hbar v}{W} \sinh^{-1}\left(\sqrt{\frac{1-\mathcal{T}_0}{\mathcal{T}_0}}\right), \tag{21}$$

where, we have explicitly restored $\hbar$. This gives the values of $\zeta = 0.45, 0.22$, and 0.08 meV for $\mathcal{T}_0 = 0.1$, $\mathcal{T}_0 = 0.5$, and $\mathcal{T}_0 = 0.9$ respectively.

For the long-QPC model, the parameters are the tunnelling amplitude, Δ , and the QPC length, L. The value of 2Δ is natural to identify with the bulk gap of the quantum Hall sample, cf. Appendix C. Therefore, $\Delta = E_c/2 = 3.58$ meV. The length of the QPC is then determined by the zero-energy transmission $\mathcal{T}_0$ through Eq.(18):

$$L = \frac{\hbar v}{\Delta} \sinh^{-1}\left(\sqrt{\frac{\mathcal{T}_0}{1-\mathcal{T}_0}}\right). \tag{22}$$

This yields the values of $L = 1.2, 3.2$, and 6.7 nm for $\mathcal{T}_0 = 0.1, \mathcal{T}_0 = 0.5$, and $\mathcal{T}_0 = 0.9$ respectively.

Given the parameters estimated above, the dependences $\mathcal{T}(E)$ are shown in Fig. 5.8(a). The range of energies on the horizontal axis is chosen to correspond to the typical bias voltages (100–300 μV) used in experiments. One sees that the long-QPC does not predict any noticeable deviation of $\mathcal{T}(E)$ from constant. This is due to the energies of interest being much smaller than the bulk gap $2\Delta = E_c$. The wide-QPC model, though, produces noticeable deviations. This shows that the QPC width is an important effect even for the narrowest QPCs possible.

Furthermore, we probed the energies beyond the typical voltage range up to half the bulk gap $2\Delta = E_c = 7.16$ meV, as shown in Fig. 5.8(b). The results displayed significant variation in the transmission characteristics. In context to point-QPC prediction (constant transmission), the long QPC model display noticeable deviation away from the point model. The wide model, however, vary a lot reaching to the full transmission from zero and then display oscillations. Such oscillations suggests the resonant tunneling and interference.

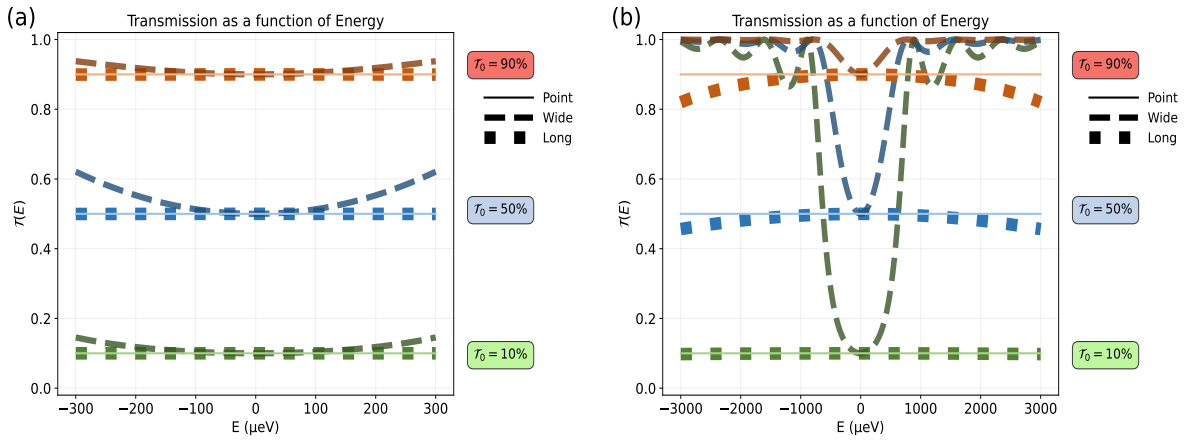

Figure 5.8: **Transmission $\mathcal{T}(E)$ for various models for experimentally realistic parameters**. (a) Comparison of the dependence of QPC transmission on energy that point-, wide-, and long-QPC models predict for realistic experimental parameters. The effects of the long-QPC model are negligible in the experimentally relevant regime. Whereas the width of the QPC does have a noticeable effect. These predictions are obtained using edge velocity $v = 2 \cdot 10^4$ m/s. The role of velocity is further discussed in Appendix **??**. (b) Comparison of QPC energy-dependent transmission for the same set of models for energy scales beyond the typical experimental range. The long-QPC predicts a noticeable dependence on energy as the scale becomes comparable with the cyclotron gap $E_c = \hbar\omega_c = 7.17\,\text{meV}$. By contrast, the wide-QPC predicts extremely strong dependence with transmission saturating at 1 (up to small oscillations) at large energies.

These $\mathcal{T}(E)$ dependences translate into experimentally measurable quantities: the QPC current, the current noise, and the Fano factor. We provide predictions for those quantities in Sec.(5.3.2).

5.3.2 *Transport predictions*

In the previous section, we analyzed the transmission functions associated with three distinct models within the conventional experimental regime. We observed noticeable variations in the transmission characteristics across typical experimental energy ranges. To enable a systematic comparison, we determined model parameters corresponding to fixed transmission values representative of weak, intermediate, and strong transmission regimes. We further examined the transmission functions beyond the conventional experimental voltage ranges, where the models exhibit more pronounced features, as discussed below in detail.

In this section, we investigate the predictions for transport quantities – specifically, the current, noise, and the Fano factor—across the point-contact, wide, and long-QPC models. We take a representative experimental temperature of be $T = 10$ mK (experiments typically use $T = 10$–40 mK).

Using Eqs.(3-4), the current $I_2(V)$ and noise S_{22} for each model are obtained directly from the corresponding transmission function $\mathcal{T}(E)$. The differential conductance is defined as,

$$g = dI_2/dV \tag{23}$$

Using Eq.(22), the current for each model is obtained directly from the corresponding transmission function. Next, we define the excess noise as the component of the noise

beyond the thermal contribution. It is obtained by subtracting the thermal noise from the total noise. For a four-terminal device, the generalized relation for the noise is given in Eq.(24), and we therefore define the excess noise as:

$$S_E = S - S\,(V = 0)$$

Further, we consider a dimensionless parameter called the Fano factor. We define it as,

$$F = \frac{S_E}{2e\left(\frac{e^2}{h}V\right)\bar{\mathcal{T}}\,(1-\bar{\mathcal{T}})}; \quad \bar{\mathcal{T}}(V) = \frac{I_2}{I_0} \tag{24}$$

where $\bar{\mathcal{T}}\,(V)$ is average transmission at a given voltage, defined as ratio of the transmitted current I_2 to the injected current $\left(I_0 = \frac{e^2}{h}V\right)$. Note that this definition is slightly different from the standard Fano factor definition due to inclusion of $(1-\bar{\mathcal{T}}\,(V))$ in the denominator. This modification allows one to treat $\bar{\mathcal{T}} \approx 0$ and $\bar{\mathcal{T}} \approx 1$ on an equal footing and is often employed in experimental papers.

The results for $|V| \leq 300\ \mu$V (which is the typical voltage range in modern experiments) are presented in Fig. 5.9. Similarly to the behavior of transmission $\mathcal{T}(E)$ in Fig. 5.8(a), the long-QPC model is indistinguishable from the point-QPC model in this voltage range. The wide-QPC model does exhibit noticeable yet small deviations from the point-QPC predictions. These deviations are can be seen in the behavior of the differential conductance g and the excess noise S_E, yet are completely unnoticeable in the behaviors of the total current I_2 and the Fano factor F.

5.3.2.1 *Typical experimental regime*

In the low-voltage regime, the current exhibits the expected linear dependence on the transmission value for all models, with no appreciable model-dependent differences, as shown in Fig. 5.9(a).

This confirms the linear transport in the weak-bias limit, where details of the transmission function are mostly irrelevant. In contrast, the noise already reveals sensitivity to the specific model. While the long QPC model produces an almost voltage-independent noise, almost consistent with its point QPC model, the wide QPC model shows non-monotonic behavior, bending downward in the weak-tunneling limit ($\mathcal{T}_0 = 0.9$) and upward in the strong-tunneling limit ($\mathcal{T}_0 = 0.1$). These features indicate that noise, unlike current, provides a more sensitive information of the underlying energy dependence of the transmission, even at voltages accessible in standard experiments, see Fig. 5.9(b).

Furthermore, for low-voltage regime, the Fano factor remains essentially constant across all models, demonstrating that voltage variations do not appreciably affect tunneling phenomenon much, as shown in Fig. 5.9(c). This insensitivity states a key point: while the transmission function $\mathcal{T}(E)$ itself varies with energy, the transport quantities—current, noise, and Fano factor—are effectively protected from these details in the experimentally relevant low-bias window. Consequently, distinguishing between different QPC models requires probing beyond the conventional voltage range.

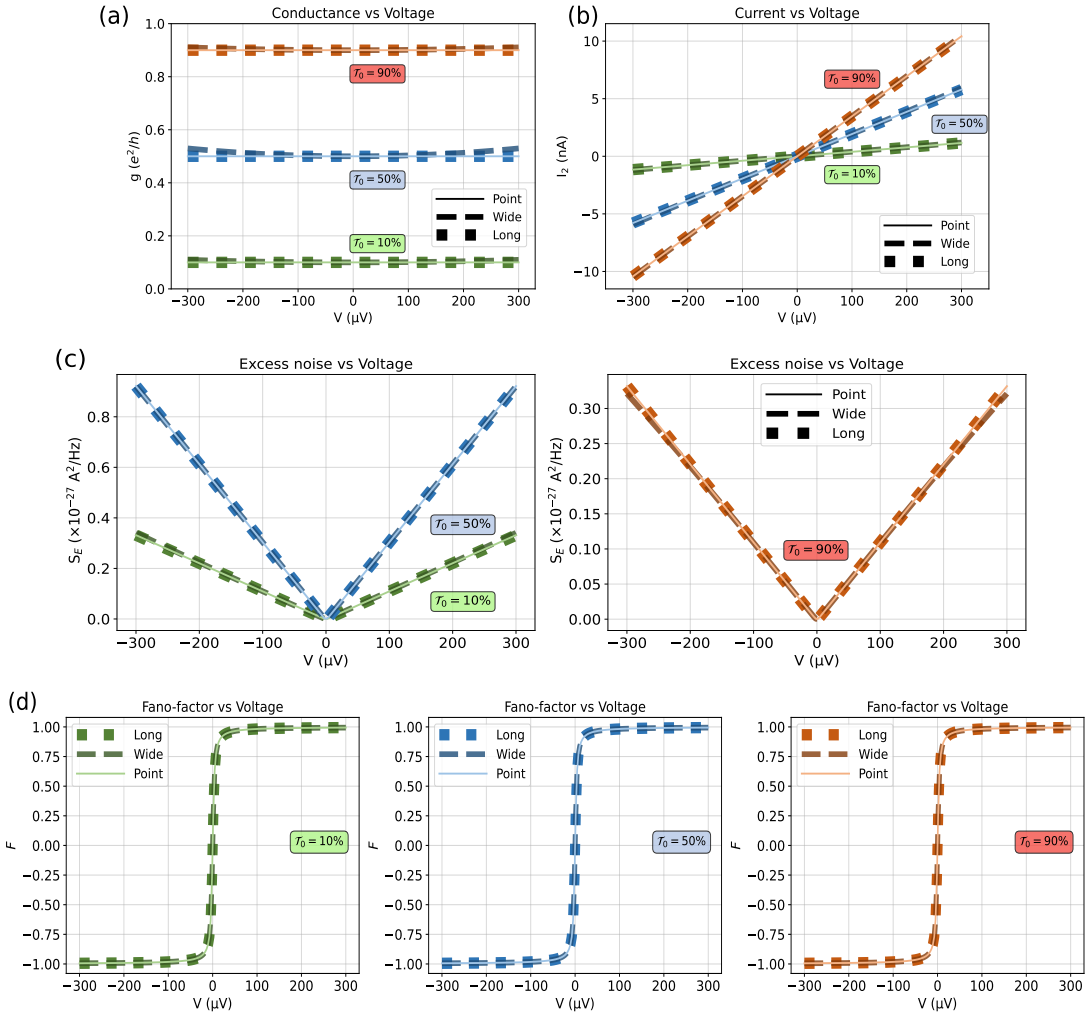

Figure 5.9: **Transport observables for point-, wide-, and long-QPC models for experimentally realistic parameters as a function of the bias voltage V.** (a) Differential conductance g. The wide-QPC model predicts a slightly higher g at large $|V|$, as compared to the point-QPC model. (b) Current I_2. No deviation between the models is noticeable. (c) Excess noise S_E. At low and high transmissions $\mathcal{T}_0$, the noise is slightly increased in the wide-QPC model at large $|V|$. (d) Fano-factor F. No deviation between the models is noticeable.

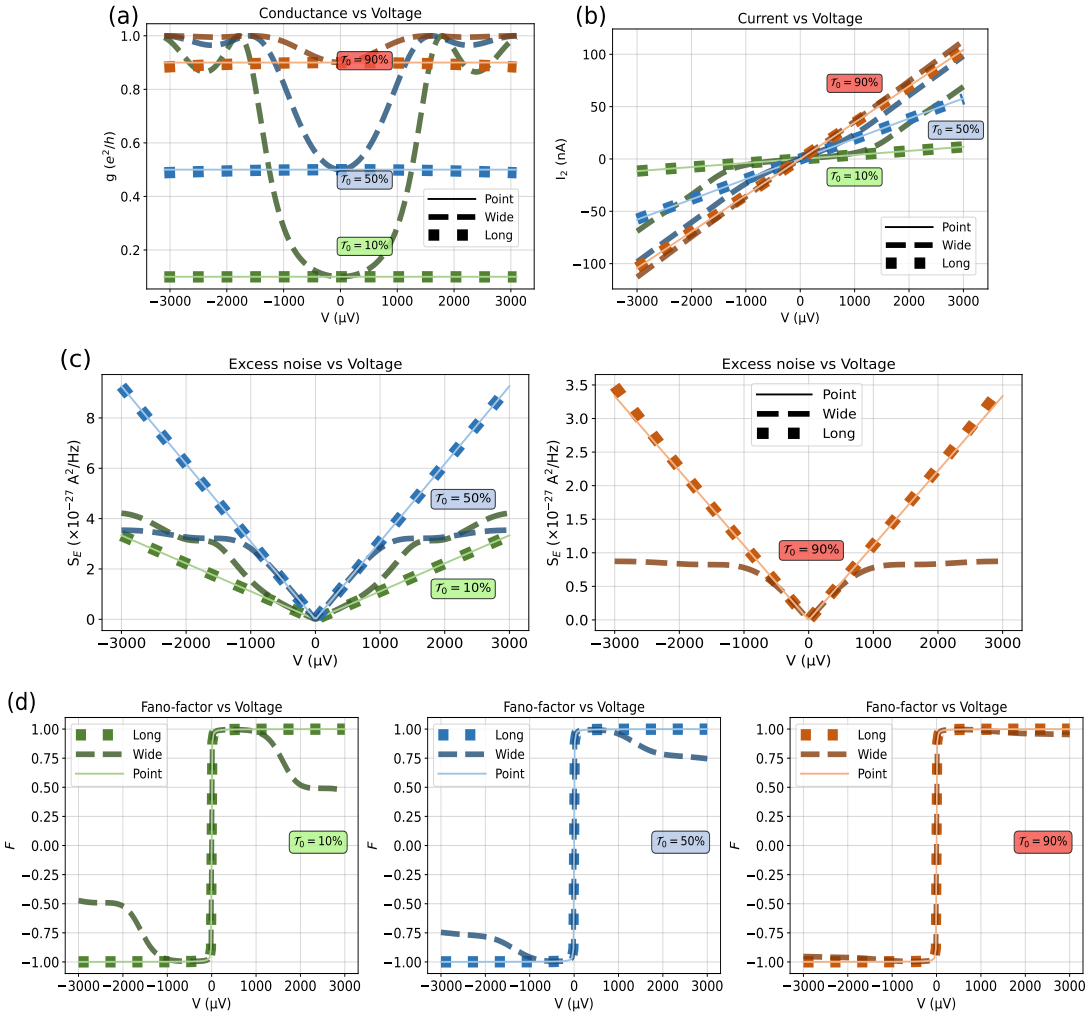

Figure 5.10: **Transport observables for different QPC models for a voltage range larger than typically investigated, yet experimentally reasonable.** (a) Differential conductance g. (b) Current I_2. (c) Excess noise S_E. (d) Fano-factor F. The long-QPC model exhibits small deviations from the point-QPC for some observables. The deviations predicted by the wide-QPC model are significant for all observables.

5.3.2.2 *High voltages*

At voltages extending beyond the typical experimental range (up to half the bulk gap $2\Delta = E_c = 7.16$ meV), the current begins to reflect the energy dependence of the transmission function. Most visible deviations among the models are observed at weak tunneling $\mathcal{T}_0 = 0.9$, with diminishing dependencies as towards strong tunneling limit $\mathcal{T}_0 = 0.1$, see Fig. 5.10(a). Among all, the wide QPC model exhibits the strongest deviation. Excess noise is strongly suppressed at elevated voltages, with the effect being most pronounced in the wide QPC model, while the long QPC model shows only gradual variations Fig. 5.10(b). Although the voltages considered extend beyond typical experimental conditions, they remain well below the bulk gap, making these predictions experimentally accessible. The dependence of the long QPC model against voltage variations is due to scale which is yet half below the bulk gap. However, present energy scale suggests a clear signature to distinguish between wide and long QPC geometries. The Fano factor also exhibits distinct variations across the three transmission values. For all models, thermal rounding is observed at low voltages until the tunneling becomes completely uncorrelated, at which point the Fano factor approaches unity. At higher voltages, the long QPC model shows only minor variations, while the wide QPC model displays the most significant changes, with the strongest suppression at $\mathcal{T}_0 = 0.1$ and the weakest at $\mathcal{T}_0 = 0.9$, see Fig. 5.10(c). This further implies that device geometry play crucial role in transport characteristics. These predictions are particularly relevant for experiments operating at elevated voltages. Overall, the results clearly indicate that both the transmission function and transport quantities carry signatures of energy dependence beyond the typical experimental range.

5.4 Conclusion

In this chapter, we introduce the transmission function as the primary focus of our analysis. Based on this, we propose two models: the wide-QPC model (5.1.2) and the long-QPC model (5.1.3). We analyze the transmission functions corresponding to each and compare them to the conventional point-QPC model (5.1.1). Finally, we investigate the transport behavior of these models using realistic parameter values.

Our results indicate that the transmission functions for the proposed models remain largely unchanged over the energy range typically accessible in experiments. Similarly, associated transport quantities—such as current, noise, and the Fano factor—exhibit minimal variation within this experimentally relevant range. This suggests that an energy-independent transmission function plays a limited role in typically probed energy range in experiments (see Fig. 5.9).

However, as the energy extends beyond the typical experimental range, significant variations in the transmission characteristics emerge. Correspondingly, the transport quantities show pronounced changes (see Fig. 5.10). These observations marks the importance of considering energy-dependent transmission effects at higher energies.

For a complete analysis and model comparison, the code repository is available at https://github.com/pkumar231999/QHE_QPC_modelling.

6

Numerical Investigation

This chapter examines the transmission characteristics of both closed and open samples incorporating two quantum point contact (QPC) gates. The edge states are injected from source 0 and collected at contacts 1, 2, and 3, respectively.

For each configuration, the propagation velocity of the edge states was evaluated. The velocity was determined using two approaches: (i) extraction from the dispersion relation, and (ii) current–density analysis across specific cross-cut of the system. Two such cross-cuts were considered—one located away from the QPC region and another within the QPC itself. Comparison between these two regions reveals distinct differences in the extracted velocities, highlighting the significance of velocity as a parameter for understanding energy-dependent transmission through QPC structures.

To further probe the bulk electronic wavefunctions, the local density of states (LDOS) was calculated along the same cross-cuts. The LDOS analysis indicates the absence of a well-defined bulk gap, contrary to assumptions made in proposed analytical models. A detailed discussion of these observations is provided in the corresponding results section. All simulations were conducted using identical parameters to ensure direct comparability between the closed and open QPC configurations.

Below are the current density map of the propagating edge modes for the closed and open QPC samples. In the closed configuration, the edge mode propagates along the sample boundary and circulates around the device, as shown in Fig. 6.1(a). In contrast, for the open configuration, the mode is injected from source 0 and absorbed at contact 2, as illustrated in Fig. 6.1(b).

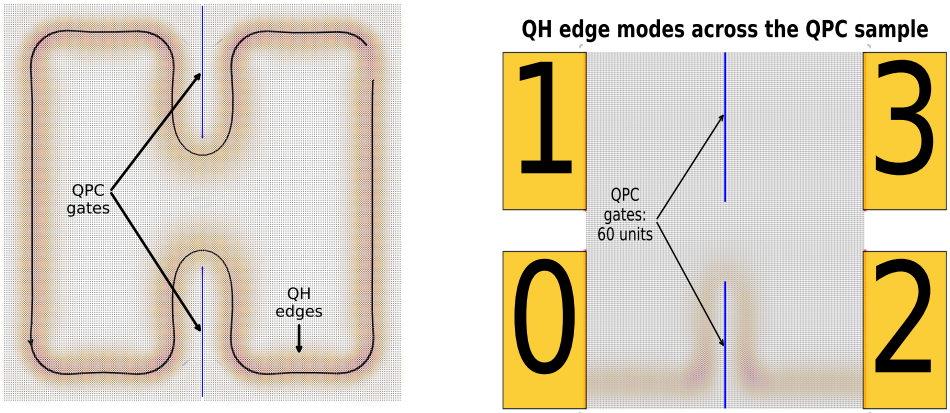

(a) (b)

Figure 6.1: **Current density** plotted for a closed-QPC gate sample and open-QPC sample. The open sample is attached with four contacts namely contact 0,1,2 and 3.

6.1 Transmission function

The transmission was analyzed as a function of energy for samples with QPC constriction lengths of 65, 75, 80, and 89 lattice units. Prior to this analysis, the dispersion relation of the contacts was plotted, with horizontal reference lines corresponding to the Landau levels of the closed sample (see Fig. 6.2. The wave vector k is defined over the Brillouin zone, ranging from $(-\pi, +\pi)$. The data for the closed sample is taken from Fig. 4.1. The observed offset in the potential arises from the confinement experienced in the lead due to its finite width. However, in our simulations, we apply an additional voltage to align the potential of the lead with that of the scattering region, allowing us to access the full energy range of the Landau levels. The chemical potential ($\bar{\mu}$) is fixed between the lowest and first Landau levels (within the green-shaded region). This green region defines a typical experimental energy window of 600 μeV (see Fig. 5.8).

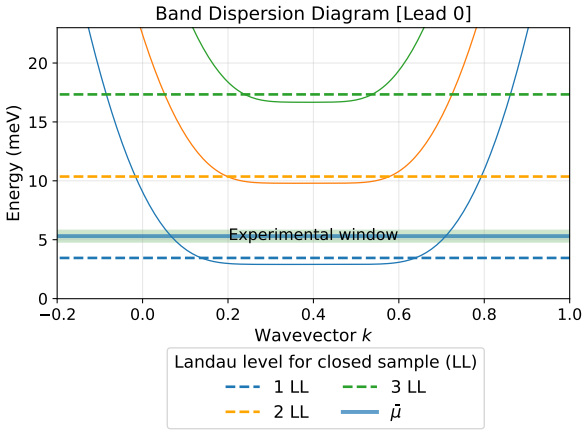

Figure 6.2: **Dispersion relation** for the contact 0. The dashed horizontal line marks the Landau levels for the closed sample. The green region is typical experimental energy windows. We set the chemical potential between the lowest and first Landau level, marked with blue line.

Let's discuss characteristics of each sample. The chemical potential is set between the lowest and the first Landau levels. The four curves in the transmission plot represents the number of transmission mode propagating from contact 0, the source contact, to rest of the contacts, namely 0,1 and 2. In addition we plot $\sum T_n$ to verify that the net transmission is equal to one. Below we comment on the respective transmission characteristics for corresponding QPC constrictions.

QPC length 65 units: The edge mode originating from contact 0 is collected at contact 2, as the inter-gate distance exceeds the magnetic length of the edge mode. This is manifested as a quantized plateau for the first Landau level (see Fig. 6.3). Reflection occurs only for the third Landau level, where the edge channel width becomes comparable to the inter-gate distance.

QPC length 75 units: Increasing the gate length reduces the inter-gate distance, leading to the onset of weak reflection. While the lowest Landau level exhibits negligible energy dependence, pronounced reflection emerges for the second and third Landau levels (see Fig. 6.4).

QPC length 80 units: At this constriction length, the inter-gate distance approaches the magnetic length, resulting in significant reflection. This behavior is clearly

reflected in the transmission spectra (see Fig. 6.5). However, near the chemical potential, transmission remains nearly constant, consistent with the point-QPC approximation of energy-independent transmission.

QPC length 89 units: For this case, the gates are sufficiently long that the inter-gate distance becomes smaller than the magnetic length. As a result, all modes are reflected and no transmission occurs (see Fig. 6.6). The characteristics are qualitatively similar to those of the 65-unit case, except that transmission is entirely suppressed rather than fully preserved.

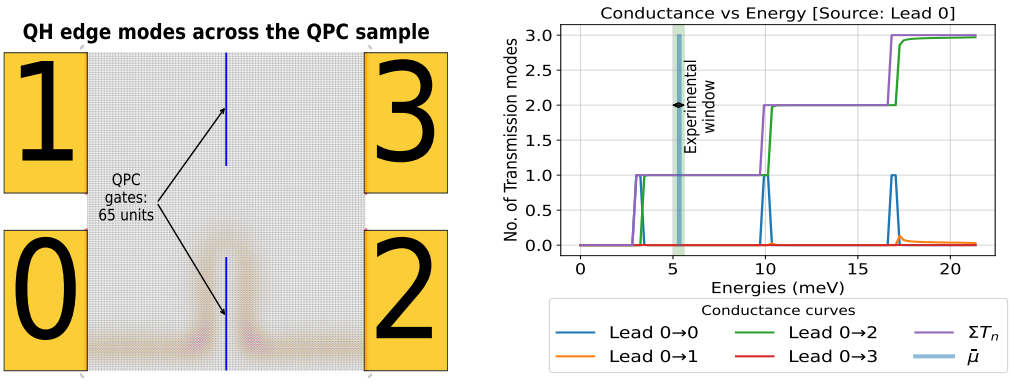

Figure 6.3: **Charge density and transmission characteristics** for a QPC constriction length of 65 lattice units. The four transmission curves represent the number of propagating modes from the source contact (0) to the drain contacts (1, 2, and 3). The thick blue vertical line indicates the chemical potential at which the charge density plot is obtained.

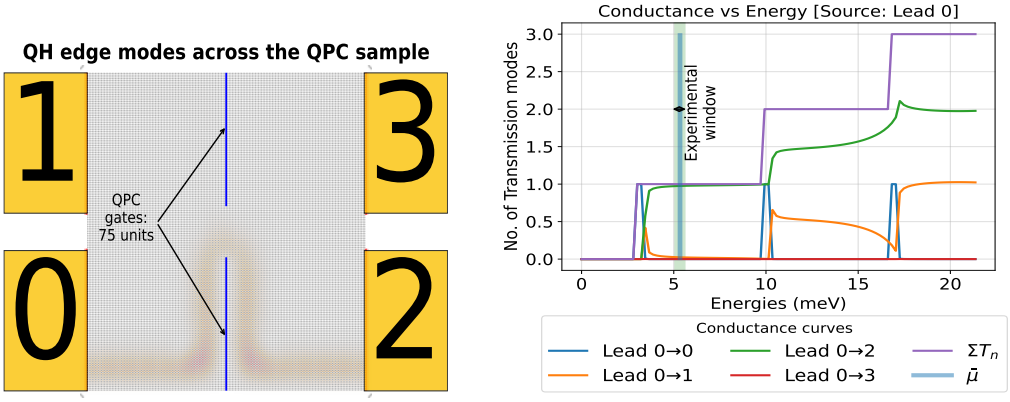

Figure 6.4: **Charge density and transmission characteristics** for a QPC constriction length of 75 lattice units. The four transmission curves represent the number of propagating modes from the source contact (0) to the drain contacts (1, 2, and 3). The thick blue vertical line indicates the chemical potential at which the charge density plot is obtained.

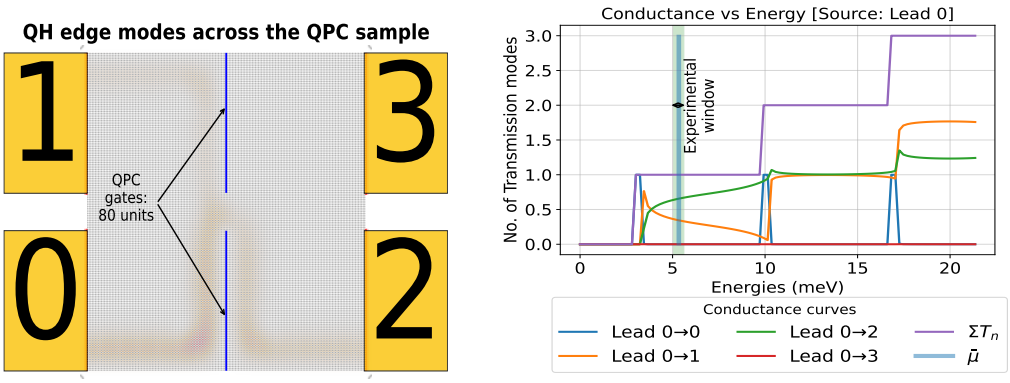

Figure 6.5: **Charge density and transmission characteristics** for a QPC constriction length of 80 lattice units. The four transmission curves represent the number of propagating modes from the source contact (0) to the drain contacts (1, 2, and 3). The thick blue vertical line indicates the chemical potential at which the charge density plot is obtained.

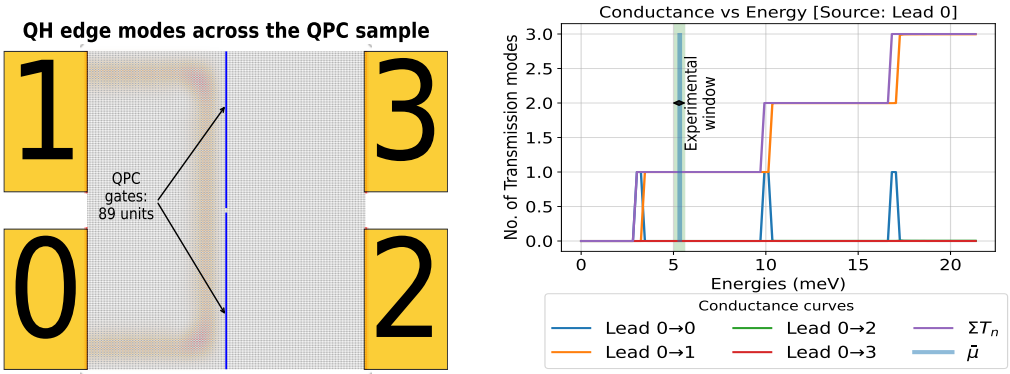

Figure 6.6: **Charge density and transmission characteristics** for a QPC constriction length of 89 lattice units. The four transmission curves represent the number of propagating modes from the source contact (0) to the drain contacts (1, 2, and 3). The thick blue vertical line indicates the chemical potential at which the charge density plot is obtained.

6.2 Transmission function: Key takeaways

For the lowest Landau level, the transmission exhibits negligible dependence on energy, in contrast to the predictions of the analytical models. At higher Landau levels, however, a pronounced reflection becomes evident as the inter-gate distance approaches the magnetic length. This effect is also influenced by where one sets the chemical potential, resulting in corresponding variations in the transmission. Nonetheless, the assumption of constant transmission remains valid predominantly for the lowest Landau level.

Moreover, analytical models predict a parabolic dependence of the transmission function on energy, as shown in Fig. 6.7. However, such behavior is not reproduced in the numerical simulations. Instead, the numerical results (see Fig. 6.5) negligible change in the transmission profile, indicating , in contrast to what been predicted by the analytical models.

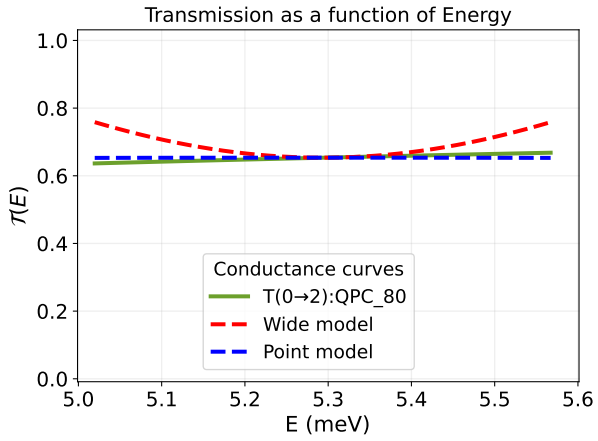

Figure 6.7: **Numerics versus analytics**: Comparison of the energy-dependent transmission function $\mathcal{T}(E)$ obtained from numerical simulations using the KWANT and from analytical models. A quantum point contact (QPC) system of 80 lattice units is considered. The numerical data correspond to the transmission from lead 0 to lead 2 in each system. Analytical curves are derived from the wide and point contact models, evaluated under equivalent physical parameters. The comparison highlights the degree of agreement between numerical and analytical approaches within a experimental window of $600\,\mu eV$.

Consider now the comparison of the predictions of the analytical models considered in Chapter (5) with the results of numerical simulations. We focus on a range of energies centered at $\bar{\mu} = 5.33\,meV$ (middle between the lowest and the first Landau levels). The width of the energy range is $600\,\mu eV$, which corresponds to the typical experimental window, cf. Fig. 5.8(a). We choose the parameters of the analytic models to match the transmission at $E = \bar{\mu}$.

We notice that the variation of transmission predicted by the wide model is significantly larger than that predicted by the numerics. Surprisingly, the point model provides a better description of numerical prediction.

Remember that even the variation of transmission predicted by the wide model does not lead to a noticeable effect on observable quantities, cf. Fig. 5.9. This means that the level of variation predicted by numerics in will not produce any noticeable difference of the observable quantities from the predictions of the point model.

6.3 Velocity analysis

We next analyze the open system, where two leads are attached to the left (lead 0) and right (lead 1) of the sample, and a single gate potential is introduced in the central region (see Fig. 6.8(b)). Compared to the closed system, where only clean bulk and edge modes are visible, the introduction of leads and a gate allows us to study transport properties and mode evolution in a more experimentally relevant setting.

6.3.1 *Edge velocity: Comparison between band and cut*

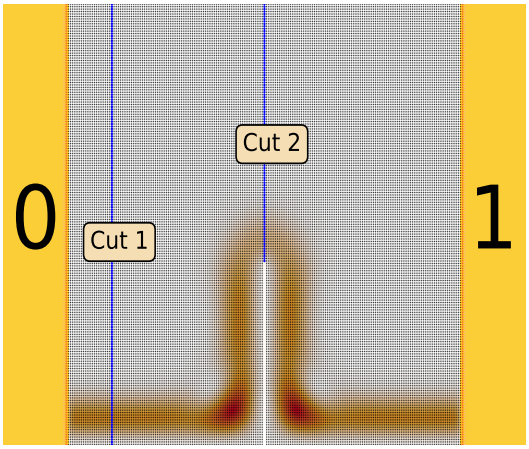

Figure 6.8: **Charge density.** The wavefunction mode injected from the left contact and propagating to right contact. The vertical blue lines marks the cuts.

The dispersion relation of lead 0 (the left lead) is shown in Fig. 6.2. Two horizontal lines indicate the cyclotron gap, and the analysis is restricted to modes within the first Landau level. The group velocity of the propagating modes is obtained directly from the slope of the dispersion relation,

$$v = \frac{dE}{dk} \tag{1}$$

Alternatively, the velocity of the chiral edge mode can be calculated from the relation between the current and density across a cut placed perpendicular to the propagation direction:

$$J = \rho v \tag{2}$$

We evaluate the velocity at two cuts, as illustrated in Fig. 6.8(b). Cut 1 is positioned away from the QPC, while cut 2 is placed inside the QPC region. The velocity extracted at cut 1 agrees with the value obtained from the dispersion relation, demonstrating consistency between the two approaches. However, the velocity at cut 2, within the QPC, deviates significantly from the injected edge state velocity. This highlights that the local velocity of edge states is strongly modified by the confinement potential of the QPC and have some noticeable dependence on the spacial configurations of the sample..

To provide a direct comparison with experiments, the velocity is evaluated using realistic physical parameters, and the results are plotted in Fig. 6.9. These findings emphasize that velocity is not a uniform property of edge states but depends sensitively on local geometrical and electrostatic details.

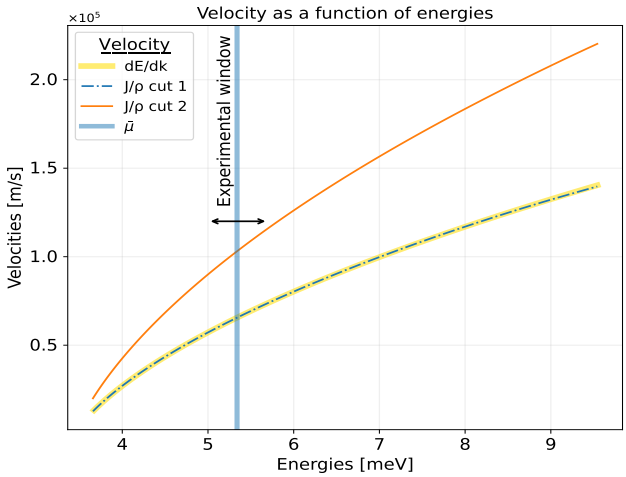

Figure 6.9: Comparison of velocities obtained from dispersion analysis and line cut-based evaluation. The experimental energy range corresponds to that typically accessed by real measurement devices.

6.4 Velocity analysis: Key takeaways

The key findings from the velocity analysis can be summarized as follows. First, the propagation velocity varies by ~10% within the typical experimental energy window. This variation is not accounted for in our analytic models and might explain the unexpectedly small variation of the transmission within the typical experimental energy window. However, developing analytical models that take the energy dependence of velocity into account is a task for the future. Second, the velocity in the middle of the QPC (cut 2) is significantly different from the edge velocity away from the QPC. This shows that the variation of velocity within the QPC may also be an important to account for.

6.5 LDOS analysis

In order to probe the bulk wavefunctions, one need to probe the closed system geometry. We perform the LDOS analysis for samples with QPC constriction lengths of 65, 75, 80, and 89 lattice units. Two cuts were considered:

- Cut 1: located away from the QPC region.
- Cut 2: positioned within the inter-gate region.

The edge-mode density profiles at both cuts, together with the corresponding LDOS, are shown in Figs. (6.10,6.11,6.12,6.13).

For cut 1, the LDOS exhibits both bulk and edge states, as the cut traverses the bulk region and its boundaries. The three observed bands correspond to the first three Landau levels. Importantly, cut 1 yields nearly identical density maps across all QPC lengths, confirming the robustness of bulk and edge features with respect to QPC's constriction length.

For cut 2, the most significant observation is the absence of a well-defined bulk gap. This indicates that the simulations do not reproduce the predictions of the long-QPC model, which incorporates a bulk gap of approximately half the cyclotron energy.

Consequently, the long-QPC model falls outside the scope of the present comparison. However, the long-QPC model may still remains relevant in the fractional quantum Hall regime, where the bulk gap is substantially reduced due to electrostatic interactions.

Within the wide-QPC framework, the analysis reveals that the spatial separation between wavefunctions originating from opposite edges within the QPC region varies with gate length. Consequently, the overlap of wavefunctions across the QPC width L is also modified. Furthermore, the dependence of edge velocity on QPC geometry is not accounted for in the present simulations. As demonstrated in the previous chapters, it plays a critical role in determining transport properties.

6.6 LDOS analysis: Key takeaways

We have calculated the local density of states (LDOS) in the bulk of the system (cut 1) and in the QPC (cut 2). The bulk of the system shows flat Landau levels and edge states, as expected. The LDOS in the QPC depends on the QPC parameters. When the constriction is so wide that no tunnelling across the QPC happens (Fig. 6.10), one clearly sees the bulk Landau levels and a gap between them in the middle of the QPC. For narrower constrictions (Fig. 6.11), there is non-zero LDOS inside the gap. For yet narrower constrictions (Fig. 6.12), the LDOS corresponding to the bulk Landau levels is hardly distinguishable from the LDOS of in-gap states. These features may be studied quantitatively within the analytic long-QPC model, which is an interesting task for the future.

6.7 Conclusion

Inspired by the experimentally observed deviations from the predictions of point-QPC model in the IQHE and FQHE, we have developed analytical models that take the QPC geometry into account. We have studied these models in the context of the IQHE. We found that while realistic QPC geometry would indeed predict noticeable energy-dependent transmission, this dependence does not significantly affect experimental observables. Further, we have performed numerical modelling of the QPC transmission. We found that numerics predicts an even weaker dependece of the transmission on the energy than our analytical models. This suggests that the energy dependence of the transmission function cannot explain experimental observations and alternative explanations must be investigated. In particular, electron-electron interactions in the QPC may play an important role, as suggested by [Schiller et al., 2024]. Alternatively, disorder (absent from our numerics) may play a significant role.

We make an observation that within the typical experimental energy range, the transmission function hardly depends on energy. One might think that the point-QPC model thus provides an accurate description of the QPC. However, the numerics show that velocity dependences on energy and on the position within the sample are significant and violate the assumptions of the point-QPC model. Further, the considerations involving the wide-QPC model, clearly show that the effect of a finite QPC size is also noticeable in the energy dependence of the transmission function. Yet the numerical data predict a much weaker dependence.

Therefore, developing an analytical model that corresponds to the numerical modelling of a 2D system in multiple aspects (velocity dependence on energy, LDOS within the QPC, transmission dependence on energy) is an outstanding challenge. Developing such a model may facilitate understanding of the QPC physics.

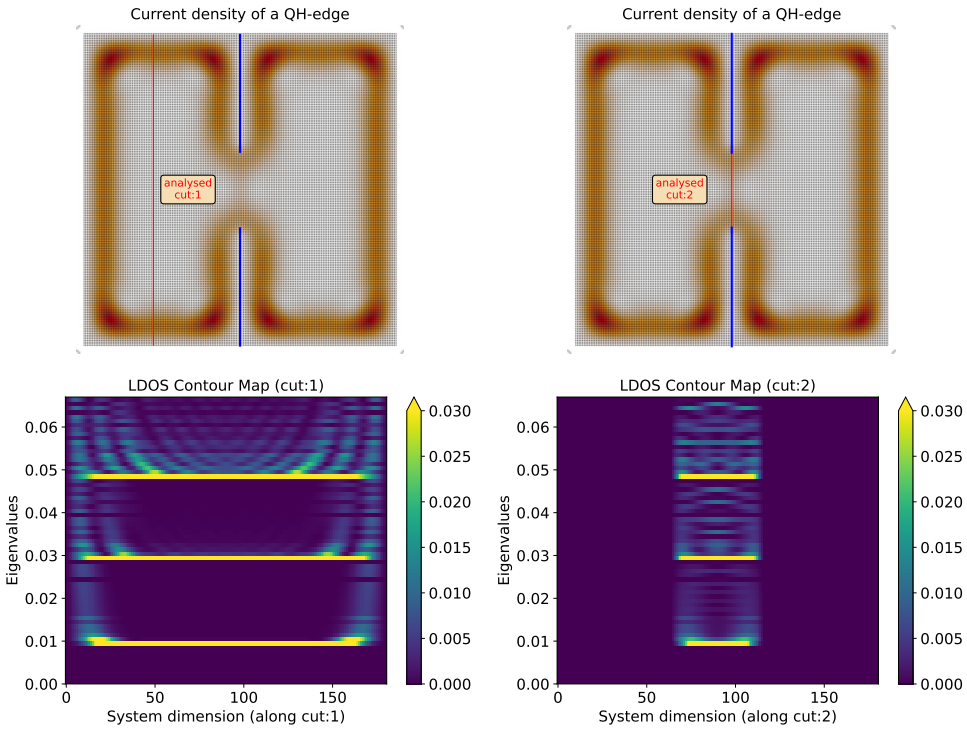

Figure 6.10: **Charge density and local density of states (LDOS)** for the closed system with a QPC constriction length of 65 lattice units. The LDOS plots are shown for the corresponding spatial cuts.

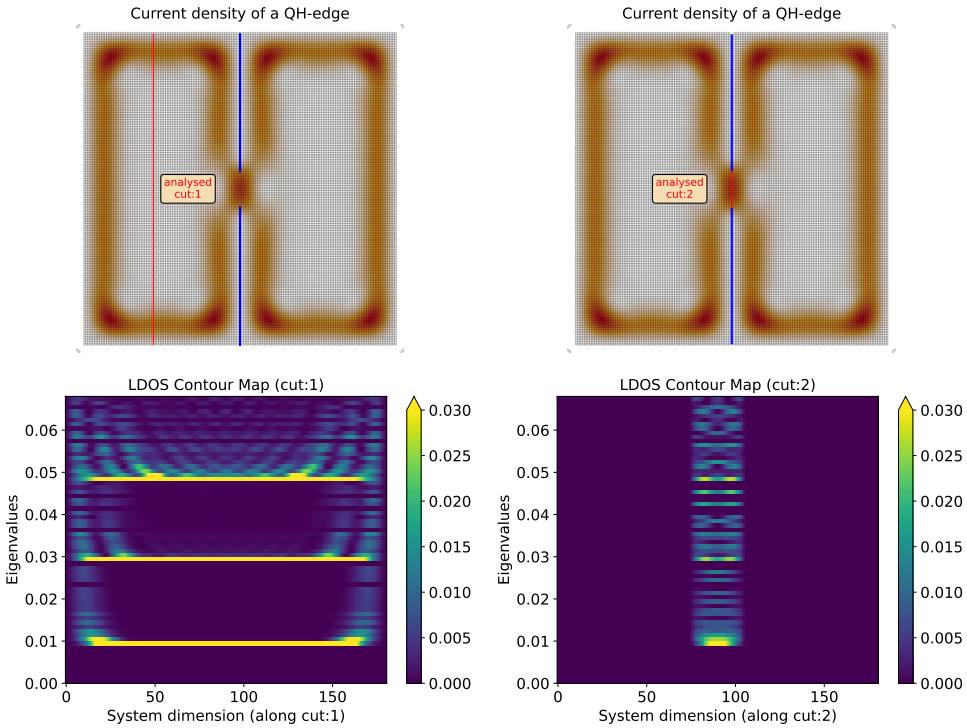

Figure 6.11: **Charge density and local density of states (LDOS)** for the closed system with a QPC constriction length of 75 lattice units. The LDOS plots are shown for the corresponding spatial cuts.

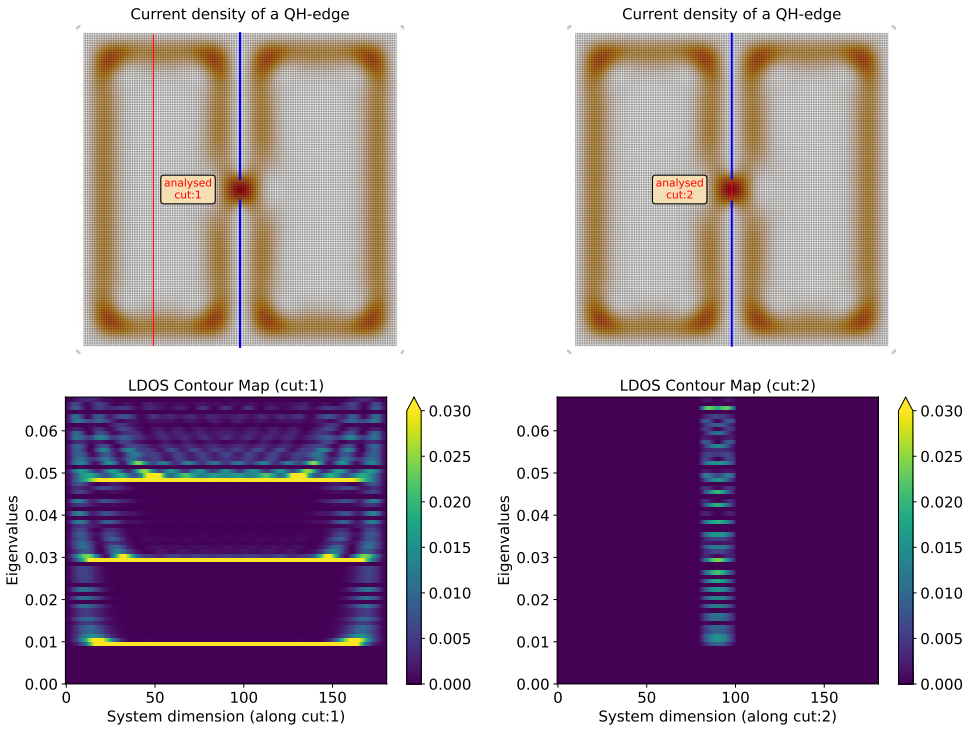

Figure 6.12: **Charge density and local density of states (LDOS)** for the closed system with a QPC constriction length of 80 lattice units. The LDOS plots are shown for the corresponding spatial cuts.

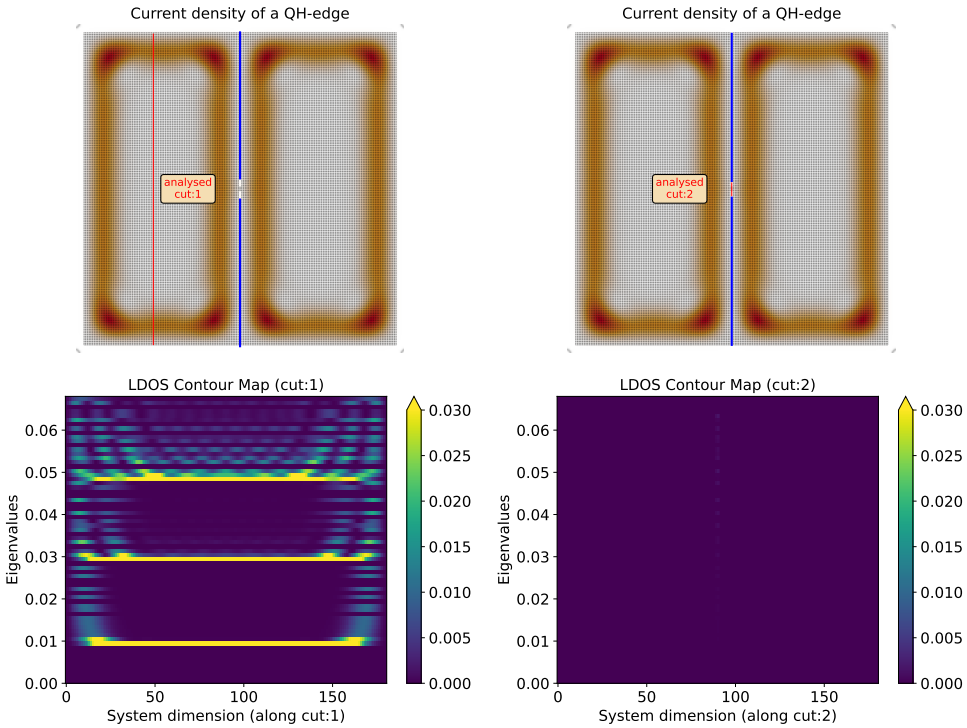

Figure 6.13: **Charge density and local density of states (LDOS)** for the closed system with a QPC constriction length of 89 lattice units. The LDOS plots are shown for the corresponding spatial cuts.

Part III

EFFECT OF INTERACTION IN ELECTRONIC INTERFEROMETERS

7

Introduction

"What we observe is not nature itself, but nature exposed to our method of questioning."

Werner Heisenberg

Until now, we have focused on modeling a single quantum point contact (QPC) in the stationary limit. While most elementary courses in quantum mechanics deal with the stationary limit, the time-dependent dynamics highlight the propagation of wave packets, which give rise to many interesting effects.

In this part of the thesis, we will study the Mach–Zehnder interferometer (MZI) device. Specifically, we will investigate the propagation of voltage pulses and the effects of electron–electron interactions, treated within the mean-field approximation. The detailed analysis and methodology will be presented in the following chapters.

Before performing full MZI simulations, we decompose the system into smaller, more manageable units and study each individually. All geometries are simulated within the lowest Landau level. We begin our investigation with the simplest quasi–one-dimensional geometry and a QPC characterized in the DC and then in short-pulse limit. Finally, we extend our study to the complete interferometer device.

7.1 Setting the tone

One key frontier in phase-coherent nanoelectronics is what happens at ultrahigh frequency, in the terahertz regime. Indeed, the typical phase-coherent length L_ϕ in a two dimensional electron gas (2DEG) is of the order of a few micrometers[Roulleau et al., 2008] while a charged excitation propagates at a speed $v_P \sim 10^5\,\mathrm{m/s}$ or faster [Roussely et al., 2016]. Hence, the duration of a voltage pulse must be shorter than $L_\phi/v_P \sim 10\,\mathrm{ps}$ for dynamical electronic interference effects to be able to take place. It is a very active field of research to try and reach this regime experimentally; it is also a necessary step towards building an electronic flying qubit [Bäuerle et al., 2018].

Among those, an interesting alley is that of controlling an interference pattern dynamically using voltage pulses [Gaury and Waintal, 2014, Gaury et al., 2015, 2014]. The predicted effects include DC currents that oscillate with the amplitude of the voltage bias [Gaury and Waintal, 2014], the non-superconducting analogue to the AC-Josephson effect [Gaury et al., 2015] or a current that oscillates as a function of the time waited before a pulse is released inside the device[Gaury et al., 2014].

All these predictions, however, have been performed in non-interacting models. The reason is chiefly technical: treating correlations is difficult while numerical simulations must performed for large devices and long times. Indeed the latter is necessary for the results to be controlled by the low energy physics and not by atomistic effects such as band gaps whose characteristic time-scale $\sim 1\,\mathrm{fs}$ is much shorter. Yet, it is well known that the transient presence of charges inside a nanoelectronics devices must be accounted for with a treatment of electron-electron interactions, if only to account for displacement currents properly. This point was discussed early on by Büttiker [Buttiker, 1993, Büttiker, 1995] who noted that the AC-conductance of a non-interacting theory did not obey current conservation (the sum of incoming AC currents does not match the sum of out-going AC current) nor gauge-invariance (raising the voltage on all electrodes generates some non-zero currents). The breakdown of these two important laws is the manifestation that the electrostatic of the problem has not been treated properly. In the non-interacting theory, charges are allowed to pile up in parts of the system at great cost in Coulomb energy. A proper treatment of Coulomb repulsion would have them screened to keep the system globally neutral. It follows that Coulomb repulsion is expected to affect the physics quite significantly.

The goal of this work is to provide such a description at the time-dependent mean-field level, the minimum level of description that can treat displacement currents properly while still remaining feasible numerically. Specifically, we study how the propagation of a voltage pulse inside a Mach-Zehnder interferometer (MZI), and the associated predicted effects, is affected by electron-electron interactions.

7.2 Review of the non-interacting theory

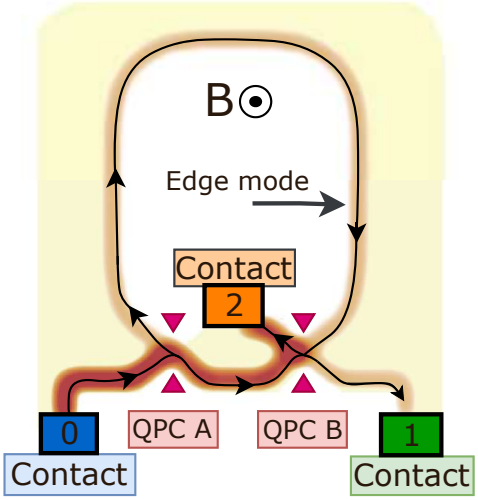

Figure 7.1: **Illustration of Mach-Zehnder Interferometer in quantum Hall regime**. The device consists of three contacts: two outer contacts (0 and 1) and one inner contact (2). Quantum point contacts (QPC A and QPC B) act as beam splitters for the chiral edge state injected from source contact 0. The edge channel is partially transmitted and reflected at QPC A, with the two paths recombining at QPC B. The resulting current is collected at the inner contact 2 and outer contact 1.

We start by considering the non-interacting picture and understand the corresponding predictions. The non-interacting predictions discussed in this section are naturally formulated within the time-dependent scattering framework (see [Moskalets, 2011] for a detailed exposition). A schematic of the system under consideration is shown in Fig. 7.1. It consists of a 2DEG in a perpendicular magnetic field B that brings it to the $\nu = 1$ quantum Hall plateau. The 2DEG has a ring topology and is connected to three Ohmic contacts: two outer contacts and one inner contact. The electronic propagation entirely takes place inside the chiral edge states; the Fig. 7.1 shows the edge state originating from contact 0, the counter propagating one originating from contact 1 is not shown, nor is the one from 2. Two quantum point contacts serve as beam splitters for the chiral edge states. A voltage pulse is sent to contact 0 and the transmitted (resp. reflected) currents I_1 (resp. I_2) are measured in contact 1 (resp. 2).

In DC, the behaviour of such a MZI is well understood: the edge state originating from contact 0 is split at the first QPC A into a short lower path of length L_l and a long upper path of length L_u that goes around the whole inner part of the ring. The two paths are recombined at QPC B and continue to either contact 1 (which we call the transmitted path) or to contact 2 (which we call the reflected path). We call d_A (resp. $D_A = |d_A|^2$) the transmission amplitude (resp. probability) of QPC A and r_A (resp. $R_A = 1 - D_A$) the corresponding reflection amplitude (resp. probability) with similar notations for QPC B. The total transmission amplitude d_{tot} to contact 1 (up to a global phase) is given by the interference of the two paths:

$$d_{\text{tot}} = d_A d_B + r_A r_B e^{\iota\Phi} \tag{1}$$

where,

$$\Phi = k_F \left(L_u - L_d\right) + \frac{BS}{\hbar/e} \tag{2}$$

and k_F is the Fermi momentum of the edge state and S is the surface of the enclosed by the two edge states. It follows that, the differential conductance given by the Landauer formula, $dI_1/dV_0 = \frac{e^2}{h}|d_{\text{tot}}|^2$ is expected to present oscillations with the magnetic field or a side gate that changes the surface S of the interfering loop,

$$\mathrm{D}_{\text{tot}} = |d_{\text{tot}}|^2 = D_A D_B + (1 - D_A)(1 - D_B) + 2\cos\left(\Phi\right)\sqrt{D_A D_B (1 - D_A)(1 - D_B)} \tag{3}$$

The transmission thus reaches external values depending on the Aharonov–Bohm phase ,

$$\begin{aligned} \mathrm{D}_{\text{max}} &= \mathrm{D}_{\text{tot}}\left(\cos\left(\Phi = 0\right)\right) \\ \mathrm{D}_{\text{min}} &= \mathrm{D}_{\text{tot}}\left(\cos\left(\Phi = \pi\right)\right) \end{aligned} \tag{4}$$

A full derivation of the Mach–Zehnder interferometer (MZI) DC transmission is provided in Appendix(G).

Such electronic interference effects have been repeatedly observed experimentally and obey well the above non-interacting theory up to a damping factor e^{-L/L_ϕ} due to decoherence processes.

7.2.1 *Voltage pulse excitation*

Having established the non-interacting framework, we now examine the effects of applying a voltage pulse of duration τ_P with an amplitude V_P described by $V_0(t)$. A typical form that we will consider is a Gaussian pulse,

$$V_0(t) = V_P e^{-t^2/\tau_P^2} \tag{5}$$

but the Lorentzian pulse (also called Levitons) popular. For our investigation, the precise shape of the shape is irrelevant, what matters are τ_P and V_P. The total number n_1 of the transmitted electron,

$$n_1 \equiv \frac{1}{e}\int_{-\infty}^{\infty} dt I_1(t) \tag{6}$$

In the adiabatic limit of very slow pulses (large values of τ_P so that $\hbar/\tau_P$ is the smallest energy scale in the problem), the Landauer formula applies at all times,

$$I_1(t) = \frac{e^2}{h} D_{\text{tot}} V_0(t) \tag{7}$$

and therefore,

$$n_t = D_{\text{tot}} \int_{-\infty}^{\infty} dt \frac{eV_0(t)}{h} \tag{8}$$

The total number of electrons $\bar{n}$ sent by the pulse is ($D_{\text{tot}} = 1$),

$$\bar{n} = \int_{-\infty}^{\infty} dt \frac{eV_0(t)}{h}$$

so that in the adiabatic limit we get the relatively straightforward result that $n_t = D_{\text{tot}}\bar{n}$. For our Gaussian pulse, $\bar{n}$ is given simply by,

$$\bar{n} = \frac{1}{2\sqrt{\pi}} \frac{eV_P\tau_P}{\hbar} \tag{9}$$

The more interesting regime arises in the limit of ultrashort pulses, where the adiabatic approximation no longer holds.

7.2.2 *Dynamic interference*

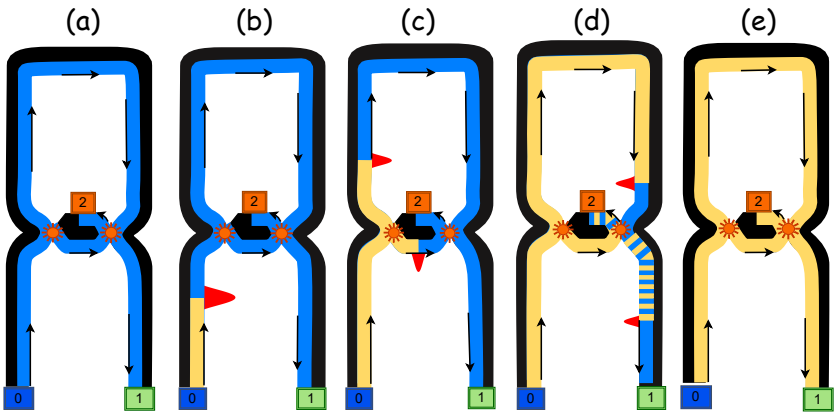

Figure 7.2: Schematic representation of the phenomenon of dynamic interference. The blue part is the delocalized waves already present. The voltage pulse (red pulse) generates a domain wall whose front (blue strip) and back (yellow strips) differs with a phase, displayed respectively. This phase difference leads to interference effect.

In contrast to stationary limit, discussed in the last section, the situation becomes really interesting in the limit of ultrafast pulses, which is the focus of our work. Under this limit, τ_P is short with respect to the flight through the interferometer. However, we suppose that τ_P is still sufficiently long that the QPC can be properly described by their transmission at the Fermi energy i.e. that the energy dependence of the transmission can be neglected. In this limit, [Gaury and Waintal, 2014] found that,

$$n_{1/2} = \Big[D_A D_B + (1 - D_A)(1 - D_B)\,\bar{n} \pm \sqrt{D_A D_B (1 - D_A)(1 - D_B)}\,\sin(\pi\bar{n})\cos(\pi\bar{n} + \Phi) \Big] \quad (10)$$

i.e. that in addition to the linear term, n_1 actually oscillates with the amplitude V_P of the pulse. Observing this prediction is the focus of some experimental activity as it would be a clear evidence of dynamical phase-coherence at the picosecond scale. If one interprets the two paths of the interferometer as a $|0\rangle$ and a $|1\rangle$, such experiments could become the basis of an electronic flying qubit, where the QPCs plays the role of a Hadamard gate and the phase Φ picked up in the loop is a rotation along the z-axis [Bäuerle et al., 2018].

To understand the origin of Eq.(10), we need to describe what happens in the lead, at the place of the potential drop, before the interferometer. Before the pulse is applied, the electronic wavefunction of the edge state in the lead is a simple plane wave,

$$\psi(y,t) = e^{\imath k y - \imath E t}$$

where, y is one-dimensional coordinate along the edge state, k is the momentum and $E = E(k)$ the corresponding energy.

Supposing that the voltage drop happens at $y = 0$, during the duration of the pulse, the rear of the plane wave ($y < 0$ inside the lead) acquires a phase,

$$\phi(t) = \int_{-\infty}^{t} \frac{eV_0}{\hbar} du \tag{11}$$

with respect to the front ($y > 0$ on the device side). The wave function thus becomes,

$$\psi(y,t) = e^{\imath ky - \imath Et - \imath\phi(t)\theta(-y)}$$

where, $\theta(y)$ is the Heaviside function. It follows that after the pulse is finished there is a domain wall in the phase of the wavefunction between the front ($y > 0$) and rear ($y < 0$) of the wave:

$$\psi(x,t) = \begin{cases} e^{\imath ky - \imath Et} & y > 0 \\ e^{\imath ky - \imath Et + \phi(+\infty)} & y < 0 \end{cases} \tag{12}$$

The phase $\phi(+\infty)$ is proportional to the number of electrons sent in the pulse $\phi(+\infty) = 2\pi\bar{n}$. The oscillations of Eq.(10) should be understood as interference between the front and the rear of the pulse as it propagates through the system. More precisely, Fig. 7.2 shows a schematic of different snapshots of the phase during the propagation of the excitation generated by the pulse.

Initially the phase is $e^{iky - iEt}$ everywhere which is represented as blue in panel (a). In panel (b), the pulse has been generated and its rear carries an extra phase $2\pi\bar{n}$ shown in yellow. In panel (c) the pulse has been split by QPC A. The interesting situation occurs in panel (d) where the lower part of the pulse has crossed QPC B but the upper part has not reached it yet. At this moment, the rear of the pulse interferes with its front (yellow-blue stripe) giving rise to the above mentioned effect. Eventually, in panel (e), the pulse reaches all the electrodes and the phase becomes yellow everywhere. In summary, there is a transient range of time for which the lower pulse has reached the electrode 1 but the upper part of the pulse has not done so. During this transient time, $I_1(t)$ contains an oscillating term $\cos(2\pi\bar{n})$that is the manifestation of the interference between the two phases in the front and rear of the pulse.

This phenomenon is demonstrated in the numerical calculations performed by [Gaury and Waintal, 2014]. The characteristics of the pulse are illustrated in Fig. 7.3(c). The time point t_a indicates the arrival of the fastest pulse, followed by subsequent pulse corresponding to the second peak. The interval between these two events represents the transient regime in which the pulse from the shorter arm of the interferometer has already arrived, while the pulse from the longer arm has not yet reached the detector. The time t_b denotes such transient regime, characterized by oscillations as a function of $\bar{n}$, see Fig. 7.3(b).

7.3 Outlook

The objective of the upcoming chapters is to investigate the robustness of such transient interference effect in the presence of mean-field interactions. In particular, we examine how mean-field interactions influence the results shown in Fig. 7.3.

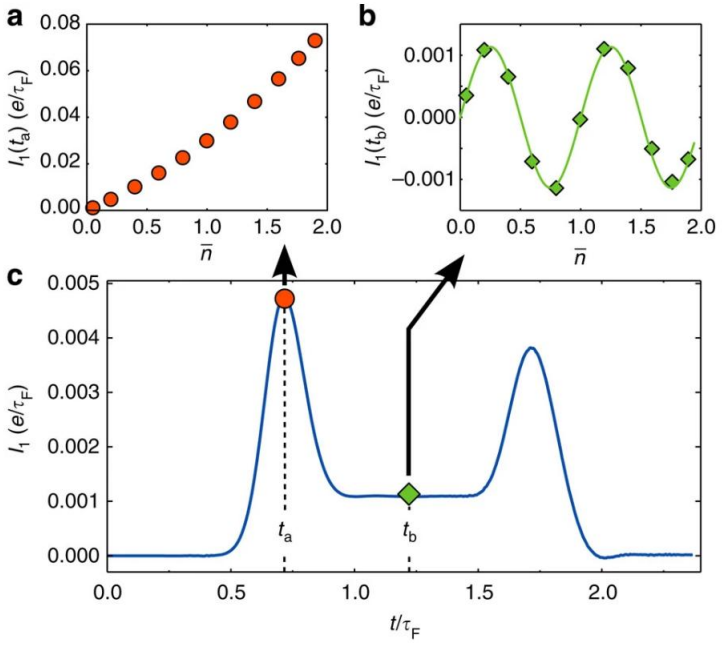

Figure 7.3: (a,b) Amplitude of $I_1(t_a)$, $I_1(t_b)$, as a function of the number of injected particles. Symbols are numerical data. The line in (b) corresponds to $I_1(t_b) = 0.001 \sin(2\pi\bar{n})$. (c) Transmitted current $I_1(t)$ as a function of time for $\bar{n} = 0.2$. The figure is adapted from [Gaury and Waintal, 2014].

8

Model and Techniques

In this chapter, we describe our discrete model, our numerical technique and discuss how interactions are treated self-consistently using TKWANT, along with the simulation parameters that form the foundation for our subsequent analysis.

8.1 Microscopic model

Let's begin with each unit of interest. All sample geometries are illustrated in Fig. 8.1.

The first and simplest unit is the quasi–one-dimensional (1D) wire (see Fig. 8.1(a)). It consists of two contacts connected by a ballistic region of length $\mathrm{L} = 200a$ and $\mathrm{W} = 10a$. The charge current is injected from contact 0 and collected at contact 1. In the quantum Hall regime, this configuration corresponds to a chiral edge mode propagating from lead 0 to lead 1.

The second component is the single quantum point contact (QPC) (see Fig. 8.1(b)). It comprises two external contacts, labeled as 0, 1 and an internal contact 2. The current is injected from the source contact 0 and collected at contacts 1 and 2. The QPC region has dimensions $\mathrm{L_{QPC}} = 22a$ long and $\mathrm{W_{QPC}} = 22a$.

Finally, two adjacent QPCs arranged as shown in Fig. 8.1(c), form an interferometer structure. Here, the edge state splits at the first QPC and recombines at the second, constituting a Mach–Zehnder interferometer (MZI). The interferometer has a total length of $\mathrm{L_{MZI}} = 100a$ long and $\mathrm{W_{MZI}} = 250a$, with each arm of width $\mathrm{W} = 10a$. The corresponding figure highlights all the key components of the MZI as in the discretised lattice form.

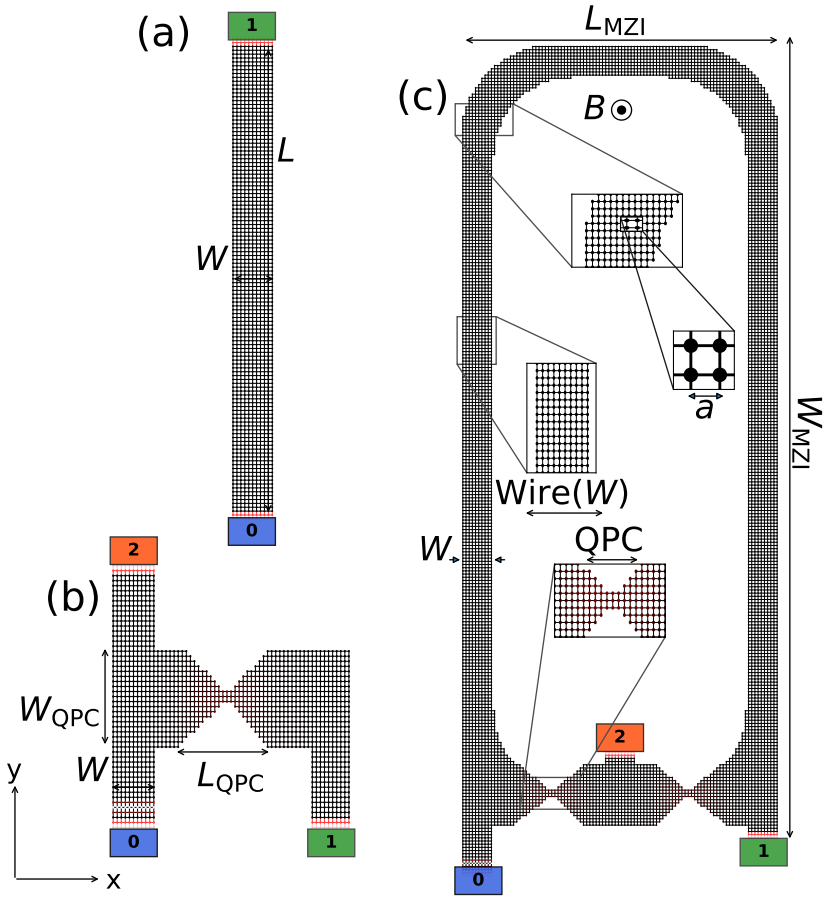

Figure 8.1: Tight-binding models considered in this work. (a) A quasi-one dimensional wire connected to two semi-infinite electrodes 0 and 1. Width: W = 10 sites, length: L = 200. (b) a Quantum Point Contact (QPC) connected to three electrodes 0, 1 and 2. $L_{QPC} = W_{QPC} = 22$. (c) the Mach-Zehnder interferometer (MZI) that contains the QPC and the wire region as subparts. $L_{MZI} = 100$ and $W_{MZI} = 250$ for a total of around 17000 sites. The different insets are zoom into different regions.

8.1.1 *Model with mean-field interaction:*

Our starting point is a 2DEG (as typically found at an interface of GaAs and GaAlAs) described at the effective mass approximation level,

$$H_{2\mathrm{DEG}} = \frac{1}{2m^*}\left(\boldsymbol{P} - e\boldsymbol{A}\right)^2 + V\left(\vec{r}\right) \tag{1}$$

where, m^* is the effective electron mass, $\boldsymbol{P}$ is the momenta, e is the electronic charge, $\boldsymbol{A}$ is the vector potential and $V\left(\vec{r}\right)$ is the onsite potential on site $\vec{r}$. We discretise the problem on a square grid with a lattice parameter a using,

$$\partial_x^2\psi \approx \left[\frac{\psi\left(x-a\right) - 2\psi\left(x\right) + \psi\left(x+a\right)}{a^2}\right] \tag{2}$$

We incorporate the perpendicular magnetic field by means of Peierls phase in the Landau gauge. The Coulomb interaction is treated through a contact Hubbard-like interaction that

we treat at the mean-field level. This is the self-consistent time dependent Hartree-Fock approximation which, we recall, is more accurate than its static counterpart. In particular, it captures the Random Phase Approximation (RPA)[Negele and Orland, 2018]. We arrive at

$$\mathrm{H} = \mathrm{H}_0 + \mathrm{H}_\mathrm{b} + \mathrm{H}_\mathrm{int} \tag{3}$$

where,

$$\mathrm{H}_0 = \sum_{\langle i,j\rangle,\sigma} H_{ij}\left(t\right) c_{i\sigma}^\dagger c_{j\sigma}\,;$$
$$\mathrm{H}_\mathrm{p} = \sum_{i\sigma} V_i c_{i\sigma}^\dagger c_{j\sigma}$$
$$\mathrm{H}_\mathrm{int} = \sum_{i,\sigma} U_{i\sigma}\left(t\right) c_{i\sigma}^\dagger c_{i\sigma}$$

The H_0 is the non-interacting term with H_{ij} is the nearest neighbor hopping. The $c_{i\sigma}^\dagger$ $[c_{i\sigma}]$ creates[destroys] a particle on site i with spin σ and $\langle\rangle$ represents the nearest neighbor coupling. The external potential is given as $V_i \equiv V\left[\vec{r} = (i_x a, i_y a)\right]$. The shape of the potential pulse V_i is chosen in the regime such that it varies quickly enough with respect to the propagation time through the interacting region, however, slow enough with respect to the energy bandwidth of the system to avoid the spurious effects due to energy scales comparable to the Fermi energy E_F/γ.

Under the time-dependent mean-field approach, the interaction terms read as:

$$U_{i\sigma} = U\left[\rho_{i\sigma}\left(t\right) - \rho_{i\sigma}\left(t=0\right)\right] \tag{4}$$

with the self-consistent condition:

$$\rho_i\left(t\right) \equiv \langle c_{i\bar{\sigma}}^\dagger\left(t\right) c_{i\bar{\sigma}}\left(t\right)\rangle \tag{5}$$

Here, $\bar{\sigma} = \uparrow$ (resp. $\downarrow$) when $\sigma = \downarrow$ (resp. $\uparrow$).

In practice, we do not consider the role of the Zeeman-field or exchange energy, so that the spin degree of freedom is purely spectator and from now onward we drop the spin index. Note that the system in infinite, i.e, finite scattering region with the leads extend to infinity. The interaction and the external potential terms are only present in the MZI region. We suppose that the external potential already accounts for possible self-consistent potential due to static term, before one send the voltage pulse in the system.

The matrix element H_{ij} are zero except when i and j are nearest neighbors on the grid. In that case, according to the Landau gauge, we have

$$H_{ij} = \gamma e^{-\iota\phi_a \frac{(i_x+j_y)(i_y-j_y)}{2}} \tag{6}$$

with $\gamma = \frac{\hbar^2}{2m^* a^2}$ and $\phi_a = Ba^2/\left(\hbar/e\right)$, the magnetic flux passing through a $a \times a$ plaquette in units of the quantum of flux. At the interface of the lead 0 and the scattering region of the MZI, H_{ij} acquires an extra phase $\phi\left(t\right)$ that corresponds to the voltage pulse,

$$\forall i \in \text{Lead } 0; \forall j \in \text{MZI } H_{ij} \rightarrow H_{ij} e^{-\iota\phi(t)} \tag{7}$$

8.1.2 *Numerical technique: Self-consistent TKWANT*

To solve the model, we use the self-consistent module of the TKWANT package[Kloss et al., 2021]. We refer to the TKWANT documentation for details of how the system of equations is solved. First, the scattering states $\Psi_{\alpha E}$ of the problems are calculated (before the pulse is applied) using the KWANT package,

$$\sum_j H_{ij}\Psi_{\alpha E}(j) + V_i\Psi_{\alpha E}(i) = E\Psi_{\alpha E}(i) \tag{8}$$

for all open modes α and N_E different values of energy that span all the occupied part of the lead bands $E \in [-4\gamma, E_F]$ (Here a single band is occupied as we work within the lowest landau level, see the section on the wire (9.1)). Second, we solve N_E Schrödinger equations self-consistently in parallel,

$$\iota\partial_t\Psi_{\alpha E}(i,t) = \sum_j H_{ij}\Psi_{\alpha E}(j,t) + V_i\Psi_{\alpha E}(i,t) + U_i(t)\,\Psi_{\alpha E}(i,t) \tag{9}$$

where, $\Psi_{\alpha E}(i, t=0) = \Psi_{\alpha E}(i)$ and

$$U_i(t) = U\sum\int_\alpha \frac{dE}{2\pi}\left[|\Psi_{\alpha E}(i,t)|^2 - |\Psi_{\alpha E}(i)|^2\right] f_\alpha(E) \tag{10}$$

where, $f_\alpha(E)$ is the Fermi function in lead α (here we work at zero temperature and all leads share the same Fermi energy). TKWANT solves this problem using a prediction-correction scheme [Kloss et al., 2021] that takes advantage of the fact that $U_i(t)$ has a much slower evolution than $\Psi_{\alpha E}(i,t)$. A typical simulation shown in this manuscript corresponds to the self-consistent solution of $N_E \approx 500$ Schrödinger equations in parallel, each of them containing a total of $17,050$ lattice sites for the full Mach-Zehnder interferometer.

8.2 Current conservation and gauge invariance

In this section, we comment on the importance of treating electron-electron interaction at some level when dealing with time-dependent phenomena, even when the system under consideration, here a relatively high density 2DEG, is weakly correlated. In a 2DEG, the strength of electron-electron interactions is measured by the dimensionless parameter $r_s = 1/\sqrt{n_s}$ which is the ratio of the electrostatic energy $\left(e^2/4\pi\epsilon r\right)$ with $r = 1/\sqrt{n_s}$ being the average distance between electrons) over the kinetic energy $\left(\hbar^2/2mr^2\right)$. The system starts to be correlated for $r_s > 10$ with the transition to the Wigner crystal around $r_s = 30$.

Yet, one should remember that at equilibrium the system is essentially neutral. As soon as one starts to, say, send a voltage pulse inside the system some extra charge will propagate within the 2DEG carrying an important amount of electrostatic energy. This charge will be screened in one way or another either by the 2DEG itself or by surrounding

metallic elements in e.g. the electrostatic gates. Let us consider the charge conservation equation,

$$\frac{\partial \rho_i}{\partial t} = \sum_j I_{ij} \tag{11}$$

where, $\rho_i = \langle c_i^\dagger c_i \rangle$ is the charge on site i and $I_{ij} = -2\Im\left[H_{ij}\langle c_i^\dagger c_i\rangle\right]$ is the current going from site j to site i. This current term is the discrete version of the divergence of a current density $\boldsymbol{\nabla}\cdot \mathrm{I}$. Remembering Gauss law, the appearance of the term $\partial\rho i/\partial t$ must correspond to the appearance of an electric field $\boldsymbol{E}$ with

$$\nabla \cdot \frac{\partial \boldsymbol{E}}{\partial t} = \frac{e}{\epsilon}\frac{\partial \rho}{\partial t} \tag{12}$$

i.e. a displacement current $\partial \boldsymbol{E}/\partial t$ adds on to the particle current $\mathbf{I} \to \mathbf{I} + \partial \mathbf{E}/\partial t$ in order to screen the charge. This displacement current is the key ingredient that is missing in the non-interacting theory.

A dual way to look at the same problem is through gauge invariance. Suppose that one raises the electric potential of the system *everywhere* in the system (i.e. in the lead *and* in the MZI) by a pulse $V(t)$. Then it is trivial to observe that this pulse can be "gauged out" by redefining the wave function as

$$\Psi_{\alpha E}(i,t) = e^{-i\int_0^t du V(u)}\bar{\Psi}_{\alpha E}(i,t) \tag{13}$$

where $\bar{\Psi}_{\alpha E}(i,t)$ obeys the Schrödinger equation without the time dependent term. In other words, if one send a voltage pulse everywhere, it does nothing. In the non-interacting version of our model however, we have supposed implicitly that the electric potential of the MZI is fixed as if the potential difference (in an actual experiment only potential *differences* could be applied between the electrode and the MZI itself. In reality, however, this potential can only be applied between different electrodes or between electrodes and electrostatic gates. It follows that the electric potential inside the MZI must be allowed to vary in time to restore the correct physical behaviour.

In short, in order to get a physically coherent picture, the electrostatic of the problem must be respected. In a discrete model this amounts to introduce a capacitance matrix C_{ij} with $\sum_j C_{ij}U_j(t) = \rho_i(t)$. The self-consistent time dependent Hartree-Fock approximation used in this work corresponds to $C_{ij} = U\delta_{ij}$. The locality of the matrix emerges spontaneously from the response of the 2DEG but can also be helped by the presence of nearby metallic gates (see Fig. 4 in [Armagnat et al., 2019]). Previous work have studied the effect of the electron-electron interactions, at this level of approximation, inside a wire geometry and in the absence of magnetic field. It was found in particular that, as expected by bosonisation and Luttinger theory, the Fermi velocity gets renormalized into a (larger) plasmon velocity. The calculated plasmon velocity agreed quantitatively with what is obtained from (multichannel) Luttinger theory and a quantitative match, in the absence of fitting parameter, was found with experiments measuring this velocity. The present work extend these works to the quantum Hall regime and to an actual full-fledged MZI interferometer.

8.3 Simulation parameters

For a discretisation parameter $a = 13\,\text{nm}$, the simulation correspond to a sample of realistic size $2.6\,\mu\text{m} \times 1.3\,\mu\text{m}$.

The width is limited to $W = 130$ nm for efficiency purpose but this is sufficient for the two counter propagating edge states to propagate freely without unwanted back-scattering. We get $\gamma = 3.3\,\text{meV}$ and the electronic density corresponds to $n_s = 0.75 \times 10^{15}\,\text{m}^{-2}$, a typical value for GaAs/GaAlAs 2DEGs (on the low side). It corresponds to $\lambda_F \sim 91\,\text{nm}$. The externally applied magnetic field is $B = 1.71\,\text{T}$ which corresponds to magnetic length $l_B = 19\,\text{nm}$ and a cyclotron frequency of $E_c = \hbar\omega_c = 2.91\,\text{meV}$.

For the time-dependent simulations, our Gaussian pulse have,

$$\phi\left(t\right) = \frac{V_p \tau_p \sqrt{\pi}}{2}\left[1 + \text{erf}\left(t\tau_P\right)\right] \tag{14}$$

where, the voltage V_P is measured in units of γ and the time τ_P in units of $\hbar/\gamma$, setting $\hbar = 1$. The external potential V_i is zero except in the QPC regions where it smoothly interpolates between $V_i = V_A$ (resp. V_B) for i at the center of QPC A (resp. QPC B) to $V_i = 0$ away from the QPC. The decay of the potential is chosen so that it is smooth with respect to the Fermi wave length $\lambda_F = 2\pi/k_F$. Our dispersion relation is $E\left(k\right) = 2\gamma\left[\cos\left(k_x a\right) + \cos\left(k_y a\right)\right]$.

Typical values used in the simulations are $\tau_P = 36/\gamma$ and $V_P = 0.023\gamma$ which corresponds to $\bar{n} = 0.2$ electrons per pulse. The Fermi energy is set at $E_F/\gamma = -3.2$ which corresponds to $\lambda_F/a = 2\pi/\sqrt{E_F/\gamma + 4} \approx 7$ and a (spinless) electronic density per lattice site $n_s a^2 = \left(E_F/\gamma + 4\right)/\left(4\pi\right) \approx 0.064$. We use $\phi_a = 0.44$ which corresponds to a magnetic length $l_B/a = 1/\sqrt{\phi_a} \approx 1.51$ and a cyclotron energy $\hbar\omega c/\gamma = 2\phi_a \approx 0.88$.

To estimate the value of U that would be relevant, we need to understand how the screening takes place in the sample since we only use a local contact interaction while the actual Coulomb repulsion is long range. A particularly easy situation is when this screening is induced externally by adding a second 2DEG at a distance d below the one of interest in order to force this screening and reduce the role of the electron-electron interactions. Such a scheme has been implemented successfully in a set of recent experiments [Nakamura et al., 2020, 2022] in order to suppress Coulomb blockade and observe the phase associated with abelian anyons. In such a system, one can model the interaction by a simple planar capacitance ϵ/d per unit surface, i.e. the addition of $\delta\rho$ electron on a site gives rise to a raise of onsite energy $\delta U = \epsilon a^2/\left(de^2\right)\delta\rho$. Making contact with our model, we arrive at,

$$U = \frac{2m^* e^2 d}{\epsilon\hbar^2} \tag{15}$$

for $d = 10\,\text{nm}$, a typical experimental value, we obtain $U \approx 25$ which gives us the order of magnitude of U we should have in mind. In the next section, we discuss pulse shape in greater detail.

8.4 Conclusion

In this chapter, we established the basic framework used to investigate time-dependent transport in quantum Hall edge channels. We introduced the fundamental building blocks of the system—namely the quasi–one-dimensional wire, the single quantum point contact, and the Mach–Zehnder interferometer. We stated the simulation parameters chosen to correspond to conventional experimental setup.

We also outlined the methodology for mapping between physical and simulation units, as well as the procedure for injecting Gaussian voltage pulses to drive the system out of equilibrium. These prescriptions form the foundation for analyzing the propagation of charge excitations. In the subsequent chapter, we investigate the influence of mean-field interactions within the each component and finally on full MZI.

9

Characterization of interferometer sub-components

9.1 1D wire

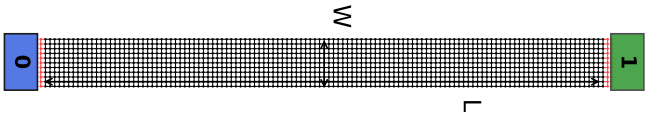

Figure 9.1: Schematic of the wire sample. The wire connects to contacts labeled 0 and 1, with a total length of $200a$ and a width of $10a$.

We start presenting our numerical results with a simple "wire" geometry corresponding to Fig. 9.3(a) for the lowest Landau level (LLL). The goal is characterize the regime in which the simulations are performed and isolate the main effect of the interactions that will take place in the Mach-Zehnder, the renormalization of the velocity.

9.1.1 *DC characterization*

We start with characterizing our wire before we send the pulse. Fig. 9.2(a) shows the dispersion relation $E(k)$ of the wire. We observe the usual Landau levels. We place the Fermi level so that a single chiral edge state is occupied. Fig. 9.2(b) show the velocity $v(k)$ for the same bands. Formally, $v\left(k\right) = \left(1/\hbar\right) dE/dk$ but here the velocity is calculated directly using the eigenstate of the current operator [Waintal et al., 2024]. A zoom of $v\left(E\right)$ is shown in Fig. 9.2(c) highlighting the velocity at the Fermi level E_F/γ and the velocity at $E_F/\gamma + V_P$. We see that V_P is sufficiently small in these numerics that the velocity can be effectively considered as constant (even though in the numerics its full energy dependence is fully taken into account).

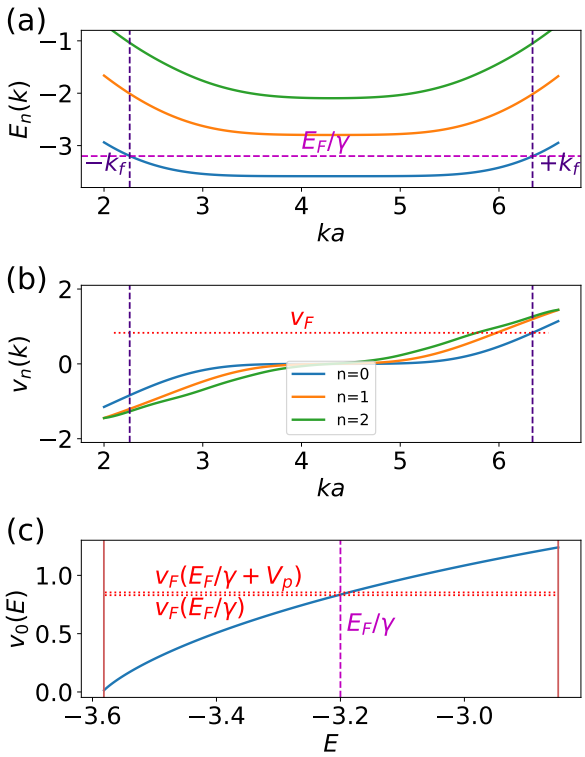

Figure 9.2: DC characterization of the wire model at ϕ_a =0.44: dispersion relation. (a) Band dispersion $E_n(k)$ of the infinite electrodes for the three lowest Landau levels. The horizontal dashed line marks the Fermi level E_F/γ. (b) The corresponding band dispersion velocity $v_n\,(k)$. (c) Same as (b) but versus energy for the lowest Landau level $v_0\,(E)$. The left and the right red bars are respectively the bottom of the lowest and first Landau levels.

The transmission D_{10} and reflection D_{00} probabilities versus energy (panel(b)) and magnetic field (panel(c)) are shown respectively in Fig. 9.3. The sample is invariant under translation which imposes $D_{00} = 0$. The Fermi energy is placed such that E_F is away from both the opening of the second channel and the bottom of the band, even in presence of the voltage pulse. Panel (c) shows the transmission versus magnetic field; the length of the last plateau is an indication of the system entering the quantum Hall regime. The position of the nth Landau level is expected theoretically to be at $E/\gamma = -4 + 2n\phi_a$ which indeed matches our observation ($\phi_a \approx 0.44$). A snapshot of the corresponding current density is shown in panel a, confirming that it is indeed an edge state.

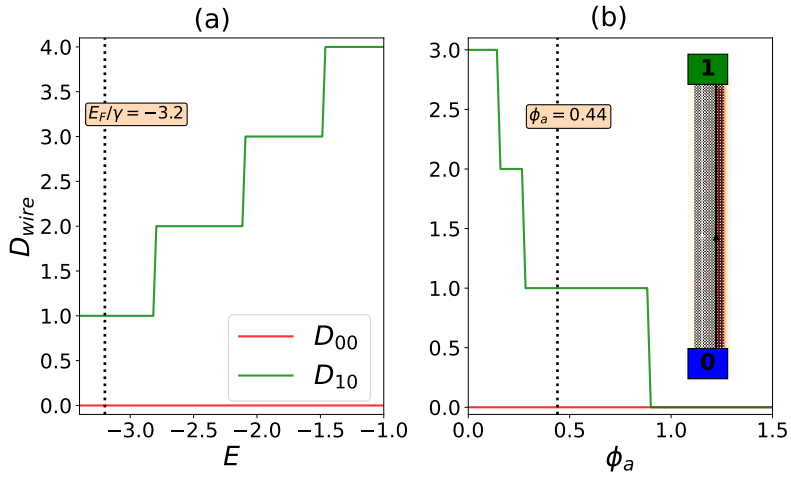

Figure 9.3: DC characteristics of a wire sample. (a) The wire sample with two contacts, namely 0 and 1. (b) The Hall edge mode for respective vertical crossovers in (b). (c) Transmission characteristics as a function of energy is plotted. The green stairs (D_{10}) are the Hall steps.

9.1.2 *Sending pulses in 1D wire*

We characterized the simple quasi–one-dimensional sample in the last section. In this section, we present the results of our numerical simulations for a pulse propagating along the sample in the quantum Hall regime.

9.1.2.1 *Adiabatic switching of interaction*

Having characterized the wire, we proceed with sending a voltage pulse through it and studying the propagation of the associated excitation. To avoid spurious reflections created by an abrupt switch on of the interaction, the interaction is adiabatically switched on in the wire over a length of $\sim 20a$, as shown in Fig. 9.4(b). More precisely, we replace the constant U with a spatially varying $U(x)$ that vanishes in the lead and saturates at the value U in the wire, following [Kloss et al., 2018]. The current versus time is measured at three cross sections of the wire (labeled cut 0, 1 and 2 in Fig. 9.4(a) and the results are shown in Fig. 9.4(c). The peaks at the different cuts appear at different times allowing one to follow precisely the propagation of the pulse in the wire, hence to extract a velocity. One observes that the propagation is faster in presence of interaction ($U = 10$, full lines) compared to the non-interacting case ($U = 0$, dotted lines) which corresponds to the renormalized velocity characteristic of Luttinger liquids.

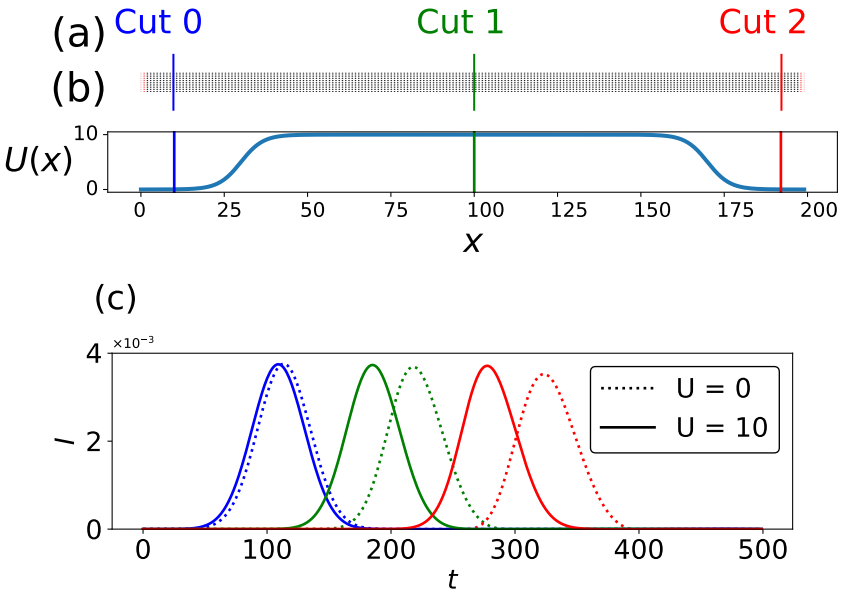

Figure 9.4: Propagation of a voltage pulse inside the wire model (9.1). (a) Schematic of the wire with the three positions where the current is recorded. (b) Profile of the interaction $U(x)$: in order to avoid backscattering due to an abrupt switch on of the interaction, the interaction is switched on adiabatically over a length of 200 sites. (c) Current versus time t at the three positions shown in (a) (respectively blue, green, red) with (full lines, $U = 10$) and without (dotted lines, $U = 0$) interaction.

The propagation can also be monitored at the level of the electronic density, as shown in Fig. 9.5. Fig. 9.5(a) shows a few snapshots of the excess electronic density without (left) and with (right) interaction. We observe again an increase of the velocity in presence of interactions. To measure this effective velocity quantitatively, we record the position of the maximum x_i in space of the electronic density at different times t_i (see Fig. 9.5(b); the slope $x_i = vt_i$ is the renormalized velocity. The resulting curve $v(U)$ is shown in Fig. 9.6. As expected, $v(U = 0)$ is given by the non-interacting velocity provided by the band structure.

9.1.2.2 *Interaction induced re-normalization of velocity*

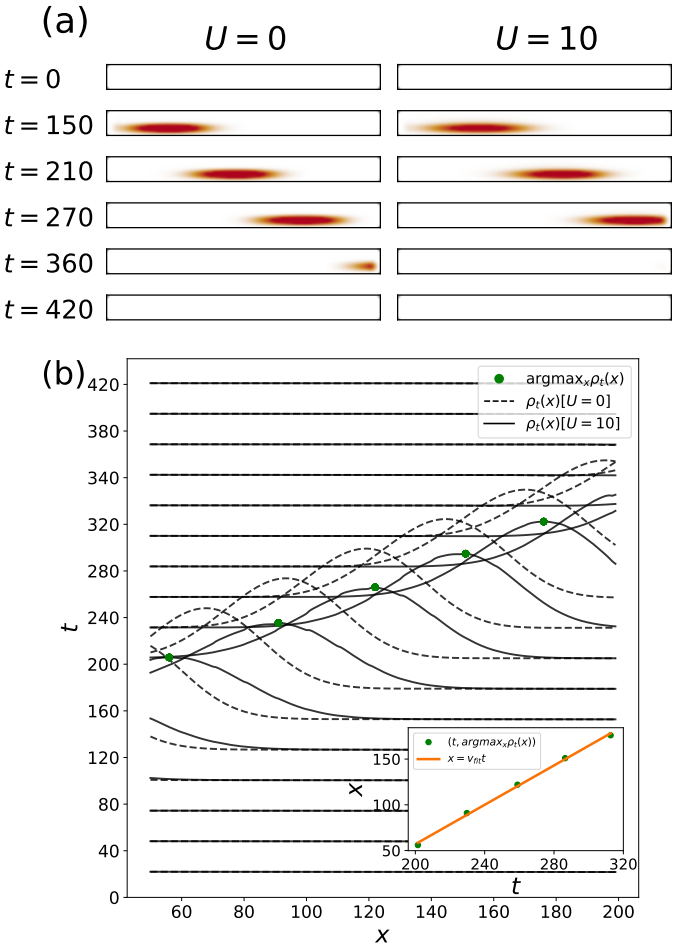

Figure 9.5: Propagation of a voltage pulse through the wire: electronic density. (a) Colormap of the density $\rho(x, y)$ at different times with (right) and without (left) interaction. (b) Same data but the density is integrated across the transverse direction y without (dashed) and with (full line, $U = 10$) interaction. The different curves $\rho_t(x) = \sum_y \rho(x, y, t)$ are translated vertically by a shift proportional to the time t. The inset shows the positionof the maximum $x = \mathrm{argmax}_x \rho_t(x)$ versus t for the different curves shown in the main plot and $U = 10$. The full line is a linear fit $x = v_{\mathrm{fit}}t$ from which the velocity of the pulse is extracted.

To understand the effect of interaction on the velocity, we resort to the semi-classical theory developed in [Kloss et al., 2018]. Qualitatively, the excess density due to the pulse gives rise to an associated gradient of potential, hence a force, which self-consistently accelerates the pulse. This effect can be accounted for quantitatively at the Boltzmann equation level which has been found to (i) recover exactly the Luttinger liquid expression derived from bosonization theory [Kloss et al., 2018] and (ii) accounts quantitatively for the experimental data of [Roussely et al., 2016] (using a proper electrostatic solver instead of the simple contact interaction used in the present work). With respect to [Kloss et al., 2018], we have two modifications to operate: first, the edge state is chiral so we have only forward propagation to account for instead of the forward and backward densities.

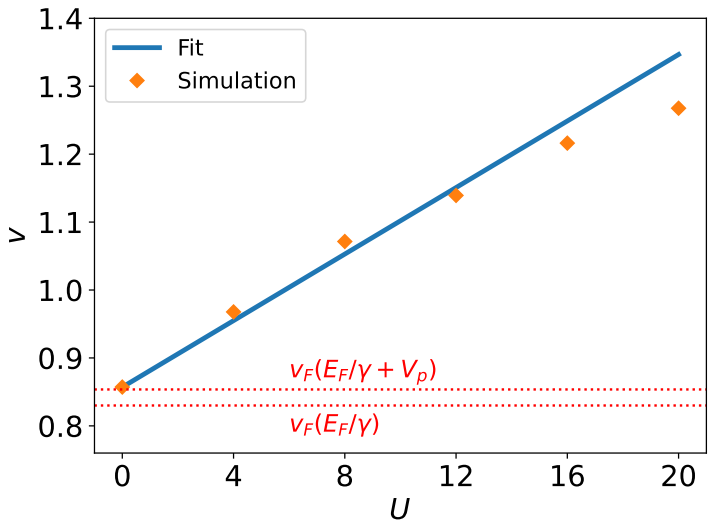

Figure 9.6: Pulse velocity (v) extracted from the simulation (see Fig. 9.5) versus interaction strength U. The horizontal red dashed lines mark the window of non-interacting velocity Fermi velocity $v(E_F/\gamma) \leq v \leq v(E_F/\gamma + V_P)$. The blue full line corresponds to Eq.2 with $l = 6.5$.

Second, the edge state has a finite width l instead of the purely one-dimensional case of [Kloss et al., 2018]. One arrives at a Liouville equation of the form,

$$\partial_t \rho\,(x,t) + \left(v_F + \frac{U}{2\pi l}\right) \partial_x \rho\,(x,t) = 0 \tag{1}$$

so that the velocity is given by a simple linear form,

$$v = v_F + \frac{U}{2\pi l} \tag{2}$$

Here, $l \propto l_B$ is the width of the edge state which we measure to be of the order of $l \approx 5$ on the density profile of Fig. 9.5. The best fit to the numerical data is given by $l \approx 6.5$ and we also note that the numerical data is not perfectly linear.

9.2 QPC

We now shift our focus from the simple quasi–one-dimensional geometry to the case of a single quantum point contact (QPC). We begin our analysis with the DC characterization of the QPC to verify its expected transport behavior. In the subsequent subsection, we send the voltage pulses and investigate the influence of interactions on the system's dynamics.

9.2.1 *DC characterization*

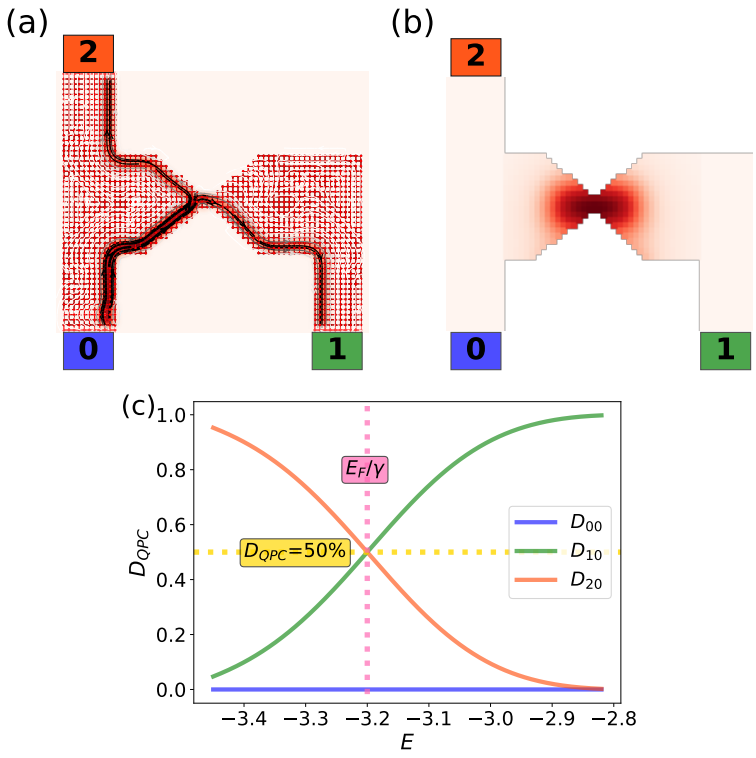

Figure 9.7: DC characteristics of the QPC model at $\phi_a = 0.44$. (a) Colormap of the current density in the QPC injected from contact 0. (b) Colormap of the potential in the QPC. The potential is maximal with value V_g at the center of the QPC and decays smoothly away from it; (c) Transmission from contact 0 to the three contacts0 (blue), 1 (green) and 2 (orange) versus energy E. The gate potential V_g has been tuned so that the QPC works as a beam splitter $D_{10} = D_{20} = 1/2$ at the Fermi energy $E_F/\gamma = -3.2$.

We now turn to the characterization of the QPC. A smooth (with respect to λ_F) potential V_i is added in the QPC region so that $V_i = 0$ away from the center of the QPC and reaches a maximum $V_i = V_g$ in the center of the constriction, see Fig. (9.7(b)) for a typical potential used in the numerics. The gate potential V_g is used to tune the QPC to be a perfect beam splitter of transmission $D_{\mathrm{QPC}} = 1/2$ at the Fermi level. Fig. 9.7(c) shows the resulting dispersion curve for the QPC transmission versus energy and Fig. 9.7(a) shows a snapshot of the edge state partition at the Fermi level.

9.2.2 *Sending pulses on a QPC*

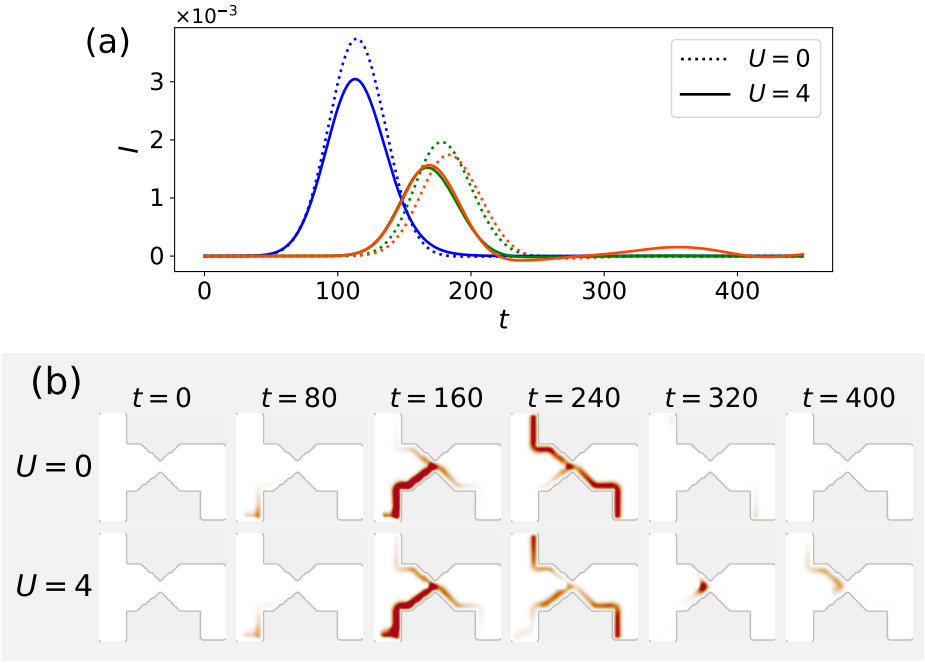

Figure 9.8: Pulse injection inside the QPC model. (a) Current $I(t)$ measured at contact 0 (blue), 1 (green) and 2 (red) without ($U = 0$, dotted line) and with interaction ($U = 4$, full line) after injection of a pulse at contact 0. (b) Colormap of the electronic density at various times without (upper panels) and with (lower panels) interaction.

The current versus time at the three contacts is shown in Fig. (9.8(a)) while Fig. (9.8(b)) shows the corresponding snapshots of the excess density at various times. Without interaction, the pulse is cleanly split between the transmitted part to contact 1 and 2 indicating that the pulse amplitude is small enough for the non-linearities of the QPC to play a minor role. However, when one switches on the interaction, we observe the appearance of a small new maxima in the reflected current around $t = 350$ (Fig. 9.8(a), thin red line) which can also be seen in the lingering density in Fig. 9.8(b) panel $t = 320$. The fact that interaction effects are enhanced in the QPC region is to be expected: close to the constriction, the local Fermi energy $E_F/\gamma - V_g$ is much smaller (in fact essentially vanishes since we work in the $D_{\mathrm{QPC}} = 1/2$ regime) while the density of excess charge is essentially unaffected (due to charge conservation). Hence, the electrons are very slow at the constriction which makes the effective strength of interaction (the "local" r_s parameter, so to speak) with respect to kinetic energy much larger; non-linear effects are expected to appear. This increase of the effect of electron-electron interactions is believed to be the origin of the 0.7 anomaly observed in many different QPC devices[Bauer et al., 2013], although this phenomena is probably not captured at the level of approximation we work with. In the present numerics, this results in the mild alteration of the shape of the pulse visible in Fig. 9.8. Besides the small secondary peak, we observe a slight decrease of the width of the pulse as interaction is switched on.

9.3 Conclusion

In this chapter, we have systematically investigated the transport properties of two representative systems: a simple wire and a single quantum point contact (QPC). For both geometries, we performed DC characterization to verify the expected transmission and reflection behavior, confirming the formation of chiral edge modes in the quantum Hall regime. Subsequently, we examined the time-dependent, or AC, response by injecting voltage pulses and monitoring their propagation across the systems.

A key focus of our study was the effect of mean-field interactions. In both the wire and the QPC, interactions lead to a measurable renormalization of the pulse velocity, with stronger interactions producing faster propagation along the edge channels. In the case of the QPC, the interplay between the confinement potential and the interaction potential gives rise to slow-moving modes. Overall, our results demonstrate that time-dependent mean-field interactions affect the transient dynamics, manifesting as a renormalization of the pulse velocity.

10

Simulations of the full interferometer

We are now ready to assemble all the pieces together and perform the simulations of the full MZI device.

10.1 DC characterization

We start by checking the validity of Eq.(3) in the DC regime. In the numerics (as in actual experiments), we use a uniform magnetic field ϕ_a which enters into Eq.(3) in two vastly different scales: the flux $\mathbf{\Phi} = \phi_a N_{\mathbf{hole}}$ varies very rapidly with ϕ_a. Here, $N_{\text{hole}} \approx 10,000$ is the number of sites circonvoluted by the two interfering paths *including* the hole in the center of the sample. A variation of ϕ_a of ± 0.01 is sufficient to change the interference from fully destructive to fully constructive as shown in Fig. 10.1. The second role of the magnetic field, at a much larger scale, is to set the quantum Hall effect and hence define the width of the edge states. It follows that e.g. $D_A(\phi_a)$ and $D_B(\phi_a)$ have a slow variation with ϕ_a that sets the envelop of the interference pattern between $D_-(\phi_a)$ and $D_+(\phi_a)$ defined as,

$$\begin{aligned} D_\pm(\phi_a) = D_A D_B + (1-D_A)(1-D_B) \\ \pm 2\sqrt{D_A D_B (1-D_A)(1-D_B)} \end{aligned} \tag{1}$$

Since the QPC can be simulated separately form the full device, we can compute $D_\pm(\phi_a)$ and check that the above formula indeed correspond to the envelop of the interference pattern.

Figure (10.1(d)) shows the MZI DC transmission D^{MZI} versus ϕ_a. At this scale the interference oscillate very fast and are almost blurred but we can check that the curves $D_\pm(\phi_a)$, calculated separately, do match the envelop of the full calculation. The zoom shown in Fig. 10.1(g) also shows D_{tot} from Eq.(3) which matches the numerics precisely. However, in Fig. 10.1(d), the value of N_{hole} has been fitted to match the period of the oscillations of D_{10}^{MZI} . The obtained value of $N_{\text{hole}} \approx 10,000$ is larger than the one obtained by simply looking at the geometry of the sample $N_{\text{hole}} \approx 2,500$. This discrepancy is due to our value of $\phi_a \approx 0.44$ being too large to be fully in the continuum limit so that Peierls substitution (strictly speaking valid for $\phi_a \ll 1$) introduces some deviations. We have checked explicitly by running simulations on bigger systems (feasible in DC but not for time-dependent simulations) that this discrepancy disappears as soon as the number of sites (at fixed physical system) is made four times larger, refer to Appendix(G). Fig. 10.1((a), (b), (c) and (e), (f)) shows snapshots of the current density, injected from the different contacts (blue for contact 0, green for contact 1 and orange for contact 2)

at various values of the magnetic field corresponding to constructive, destructive and mixed interferences (blue snapshots). The entire picture is fully consistent with our understanding of this device working as an electronic Mach-Zehnder interferometer.

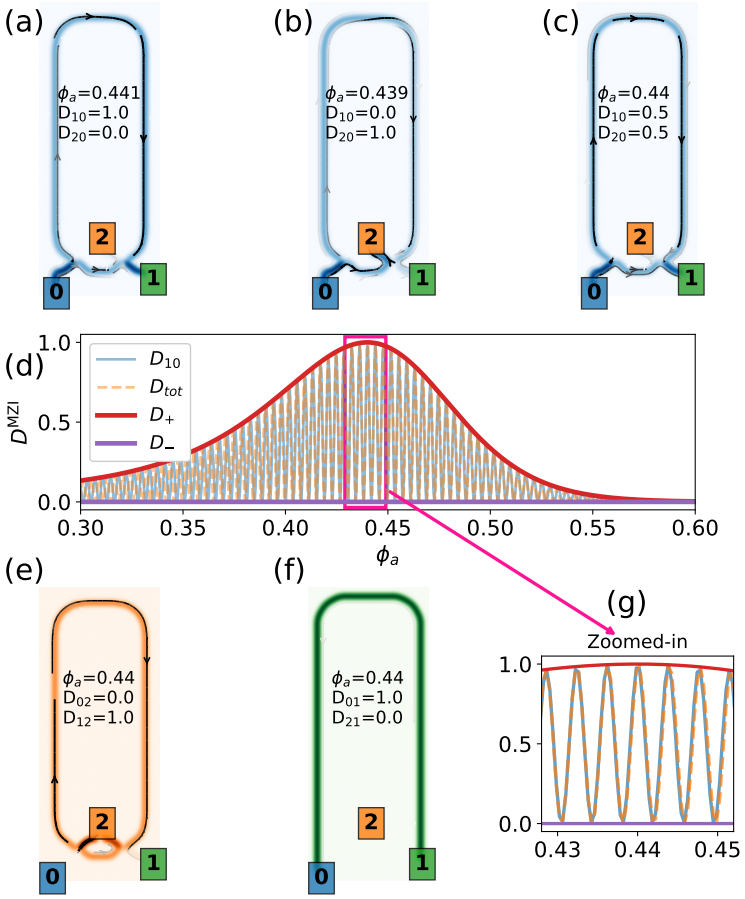

Figure 10.1: DC characterization of the MZI model. (a), (b) and (c): snapshot of the current density injected from contact 0 at slightly different magnetic fields. The different panels correspond to perfect transmission to contact 1 ($\phi_a = 0.441$, panel a), perfect transmission to contact 2 ($\phi_a = 0.439$, panel b) and half-half ($\phi_a = 0.44$, panel c). (d) Transmission D_{10} versus ϕ_a. The blue line (simulation) matches with the theory Eq.(3) (dashed orange). The two envelops D_+ (red) and D_- (purple) correspond to Eq.(1). (e) and (f) snapshot of the current density injected from contact 2 (panel e) and contact 1 (panel f). (g) Zoom of panel d. At this scale the theory Eq.(3) is indistinguishable from the numerical data.

10.2 Interferometric pulses

Establishing the results of DC characterization of the Mach–Zehnder interferometer, in this section, we investigate the propagation of a voltage pulse through the interferometer.

10.2.1 *Adiabatic switching of interaction*

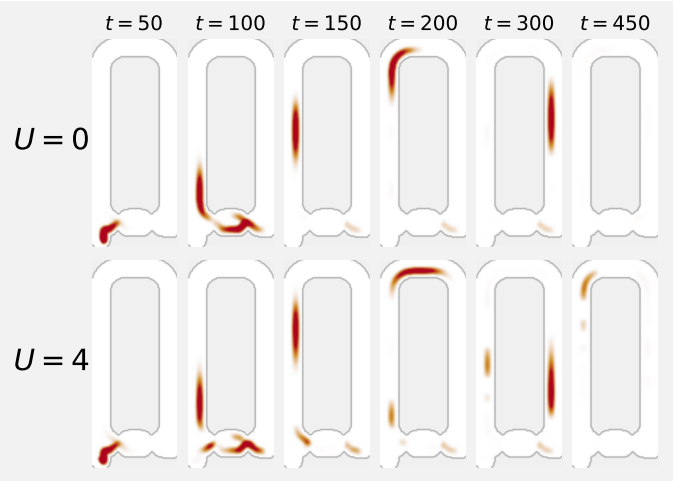

Figure 10.2: Colormap of the electronic density $\rho(x, y, t)$ within the MZI geometry after injection of a pulse at contact 0. Upper panels: $U = 0$, Lower panels: $U = 4$.

We now turn to the actual pulse propagation through the device. Snapshots of the excess density at different times are shown in Fig. 10.2 without (panel a) and with interaction (panel b, $U = 4$). We observe the propagation of the pulse in the lower and upper arms. With interaction, the situation is a little fuzzy due to the interacting effects at the QPC studied in the preceding section but global picture is the same with a long transient regime where the pulse has already gone through the lower arms but is still traveling through the upper one. At a quantitative level, the current passing through contact 1 is shown in Fig. 10.3(a). This curve has three distinctive features already present without interaction: two peaks corresponding to the arrival of the pulse through respectively the lower (marked arrival by t_a) and upper arm; a long non-zero plateau in the transient regime(marked by t_b) between these two peaks. The dynamical control of interference pattern effect, of prime interest here, is contained in this plateau. As one increases the value of the peak potential of the pulse V_P, thereby changing the total number of electrons $\bar{n}$ carried in the pulse, the value of this plateau oscillates with $\bar{n}$, as shown in Fig. 10.3(c) while the value of the peak is essentially monotonous (Fig. 10.3(b)).

10.2.2 *Interaction induced effects*

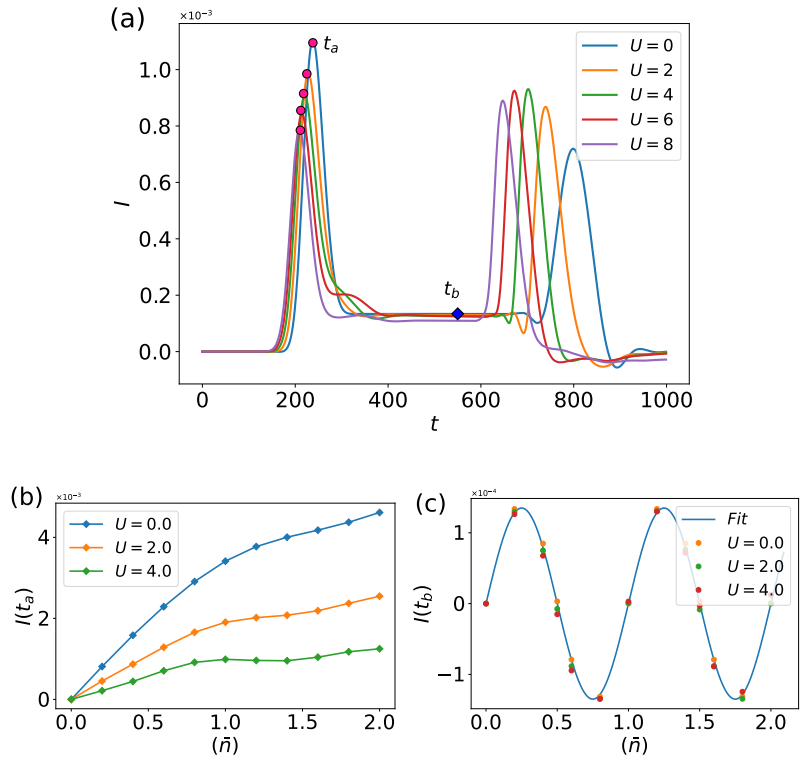

Figure 10.3: Current at contact 1 after pulse injection at contact 0 in the MZI geometry. (a) Current $I(t)$ at contact 1 versus time for different values of the interaction parameter U. The times t_a and t_b correspond respectively to the position of the first peak (arrival of the pulse through the lower arm) and the transient plateau. (b) Amplitude of the current $I(t_a)$ versus number of injected charges $\bar{n}$ (varied by changing the amplitude of the pulse VP at fixed pulse duration $\tau_P = 36/\gamma$. Different curves corresponds to different interaction strength U. (c) Same as panel b for $I(t_b)$. The solid line corresponds to a fit $I = 10^{-4}\sin(2\pi\bar{n})$.

We observe that the effect of switching on the interaction is two-folds: first, the position of the peaks is translated to the left. This is to be expected from the renormalization of the plasmon velocity discussed in section (9.1.2). Second, the shape of these peaks is modified, which is consistent with what we found at the QPC level. However, the most important feature of Fig. 10.3 is an *absence* of effect: the value of the transient plateau is unaffected by the interaction. This is relevant because this plateau corresponds to interesting new physics that one would wish to be robust to the presence of perturbations.

Figure 10.4 gathers the values of n_1 and n_2 versus $\bar{n}$, i.e. the actual observables that would be measured in an experiment. Indeed, in a typical experimental setup, one does not send a single pulse but a string of pulses separated by a period T which has to be chosen large enough for the individual pulses to be considered as independent (in practice T can be as large as 1 ns). In this setup, the DC current measured at contact 1 is en_1/T. Since DC currents are significantly easier to measure than AC ones, especially close to 1 THz, this is likely to be the first signature of dynamical interference pattern that will be measured in practice. We find that the typical oscillations of $n_1 - n_2$ that are present without interaction are barely affected by interaction (Fig. 10.4(a)). Note that these oscillating effects suppose that the pulse duration is short compared to the difference

of time of flight $(\tau_u - \tau_l)$ between the upper and lower arm. As one increases the pulse duration τ_P the effect disappear (Fig. 10.4(b)).

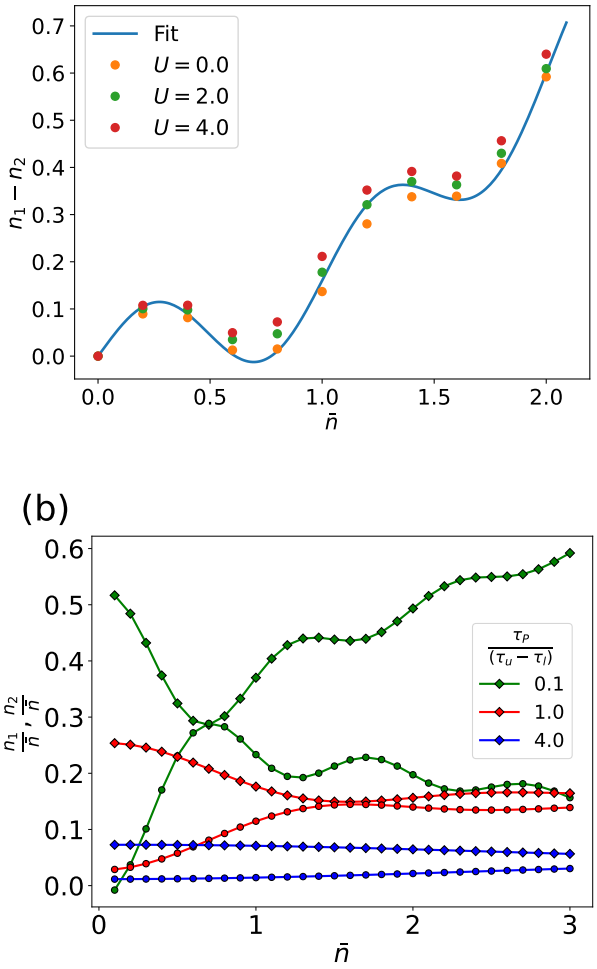

Figure 10.4: Transmitted charge versus injected charge for the full MZI. (a) Difference $(n_1 - n_2)$ between the charge collected at contact 1 and 2 versus injected charge $\bar{n}$ for different values of U. The solid line correspond to a fit. $n_1 - n_2 = 0.02\bar{n} + 0.14\bar{n}^2 + 0.10\sin(2\pi\bar{n})$. (b) Effective transmission $n_1/\bar{n}$ (diamonds) and $n_2/\bar{n}$ (circles) versus $\bar{n}$ for three different pulse durations and without interaction. The pulse duration is measured in terms of the size of the transient plateau i.e. the difference of propagation time between the lower arm τ_l and the upper arm τ_u. $\tau_P = 30/\gamma$ (green), $\tau_P = 337/\gamma$ (red) and $\tau_P = 1348/\gamma$ (blue).

10.3 Conclusion

In this part of the thesis, we have simulated the propagation of a voltage pulse through an electronic MZI of realistic characteristics taking into account the electron-electron interactions at the time-dependent mean field level. We have observed and characterized the renormalization of the plasmon velocity (extending previous works to the quantum Hall regime), identified the quantum point contacts as sources of deviations from the non-interacting limit and found that the dynamical control of interference pattern effect is robust to the presence of interactions. Overall, this study gives a rather optimistic picture that the most salient features predicted from the non-interacting theory might actually

be present in real devices. In fact, preliminary experimental results[Bäuerle, 2025] seem to indicate that it is the case.

On the theory side, much work remains to be done to arrive at the level where the simulations can have genuine predictive power. One aspect is to replace the contact interaction with the solution of the Poisson equation (in real time). This extension would make the potential seen by the electrons calculated instead of postulated which would make contact with experiments much easier. Also, effects such as edge reconstruction[Armagnat et al., 2019, Chklovskii et al., 1992] would be accounted for automatically. Such a step will be computationally expensive but should remain feasible due to the fact that the electric potential varies at a very slow time scale compared to the wave-functions. An iterative solver, that would benefit from the fact that the solution at a slightly earlier time can be used as a starting point, might be the method of choice. A second aspect is to introduce decoherence. In DC, it is known that decoherence is controlled by one particle decaying into two particles and one hole, i.e. by a second order contribution to the self energy in the strength of electron-electron interaction. Such a contribution could be calculated using e.g. tensor network approaches in the spirit of [Fernández et al., 2022]. Studying what happens to decoherence in the THz regime will be of the utmost interest and is crucial for future applications. A third extension would be the study of abelian anyons that could be done within a framework close to the present one using a composite fermion approach [Halperin et al., 1993, Halperin and Jain, 2020]. This would allow to make concrete predictions in e.g. the 1/3 fraction or even in more exotic fractions. Last, a systematic comparison between the simulations and the experiments, based on large data sets, should be performed to validate the overall approach (in the spirit of [Chatzikyriakou et al., 2022]).

Part IV

CONCLUSION AND PERSPECTIVES

This thesis has examined quantum transport phenomena in mesoscopic systems from two perspectives — the tunnelling processes in quantum Hall edge channels and the dynamic propagation of ultrafast electronic pulses in quantum Hall interferometers.

In the first part, we addressed the long-standing discrepancies between theoretical predictions and experimental observations in quantum point contacts (QPCs). We focused on the regime of integer quantum Hall effect and investigated the possible effects of energy-dependent transmission function on the QPC experiments. We have developed analytical models taking the QPC geometry into account, as well as performed numerical simulations of proper 2D samples. In both cases, we found that the resulting energy dependences of the transmission function would not produce any noticeable discrepancies in typical experiments. Our numerical investigations faithfully model the 2D system except for discarding electron-electron interactions and not including disorder. We thus conclude that these latter elements must play a significant role in the experimental observations. At the same time, we have uncovered that the standard analytical 1D approaches for modelling the QPCs disagree even with the most basic numerics that describes the full 2D system in a number of aspects (most notably, in the assumptions for the velocity dependence on energy and in the predictions for the transmission's dependence on energy). This warrants development of better analytical models in the future.

In the second part of the thesis, we shifted focus from static transport to the ultrafast, time-dependent regime, investigating the propagation of picosecond-scale charge pulses in electronic interferometers. These systems provide a promising platform for realizing "flying qubits" where coherent single-electron excitations travel along well-defined paths. Using time-dependent mean-field simulations of a Mach–Zehnder interferometer operating with ultrashort pulses, we analyzed the interplay between electron–electron interactions and its temporal dynamics. Our results show that interactions primarily manifest as a renormalization of the pulse velocity, effectively modifying the propagation speed without compromising the interference visibility.

In summary, this work investigated realistic modeling of QPC for bridging theory and tunneling experiments, as well as the ultrafast dynamics of electron wave packets in quantum Hall interferometers. Both systems are essential for mesoscopic devices and their increased understanding may be beneficial for future technologies.

Part V

APPENDICES

A

Scattering matrix coefficients in terms of transmission function

We express the following Eq.(20) as:

$$A_L^{\alpha\alpha}(\epsilon,\epsilon) = \delta_{L,\alpha}\delta_{L,\alpha} - \left[s^{L\alpha}\left(\frac{\epsilon-\mu}{\hbar v_F}\right)\right]^* \left[s^{L\alpha}\left(\frac{\epsilon-\mu}{\hbar v_F}\right)\right] \tag{1}$$

in terms of transmission $\mathcal{T}(\epsilon)$, which lands up to two possibilities:

$$A_L^{LL}(\epsilon,\epsilon) = 1 - \left[s^{LL}\left(\frac{\epsilon-\mu}{\hbar v_F}\right)\right]^* \left[s^{LL}\left(\frac{\epsilon-\mu}{\hbar v_F}\right)\right] = 1 - \left(s^{LL}\right)^2 = \mathcal{T}(\epsilon) \tag{2}$$

$$A_L^{RR}(\epsilon,\epsilon) = -\left[s^{LR}\left(\frac{\epsilon-\mu}{\hbar v_F}\right)\right]^* \left[s^{LR}\left(\frac{\epsilon-\mu}{\hbar v_F}\right)\right] = -\left(s^{LR}\right)^2 = -\mathcal{T}(\epsilon) \tag{3}$$

Note: The $1-\left(s^{LL}\right)^2 = T(\epsilon)$ and $\left(s^{LR}\right)^2 = T(\epsilon)$ follow from the unitarity of the S-matrix.

Moreover, using (20) one can also evaluate,

$$A_L^{LR}(\epsilon,\epsilon) = -\left(s^{LL}\right)^* \left(s^{LR}\right) = -\left[\mathcal{T}(1-\mathcal{T})\right]^{1/2} \tag{4}$$

$$A_L^{RL}(\epsilon,\epsilon) = -\left(s^{LR}\right)^* \left(s^{LL}\right) = -\left[\mathcal{T}(1-\mathcal{T})\right]^{1/2} \tag{5}$$

B

Transmission function for point QPC

In this Appendix, we provide the derivation of the point-QPC transmission function (10). For brevity of notation, we put $\hbar = 1$ in this section.

We start with the Hamiltonian (7-9). This yields the following equations of motion for the fields:

$$\partial_t \psi_1(x) = i[H, \psi_1(x)] = -v\partial_x \psi_1(x) - i\eta\psi_2(x)\delta(x),$$
$$\partial_t \psi_2(x) = i[H, \psi_2(x)] = v\partial_x \psi_2(x) - i\eta\psi_1(x)\delta(x).$$

Looking for solutions in the form

$$\psi_1(x) = \sum_n \hat{a}_n \phi_{n,1}(x) e^{-iE_n t}, \tag{1}$$
$$\psi_2(x) = \sum_n \hat{a}_n \phi_{n,2}(x) e^{-iE_n t}, \tag{2}$$

where $\hat{a}_n$ are the Fermionic annihilation operators, we arrive at equations for the wave functions of the system's eigenmodes:

$$E_n \phi_{n,1}(x) = -iv\partial_x \phi_{n,1}(x) + \eta\phi_{n,2}(x=0)\delta(x),$$
$$E_n \phi_{n,2}(x) = iv\partial_x \phi_{n,2}(x) + \eta\phi_{n,1}(x=0)\delta(x).$$

Integrating these equations around $x = 0$, one finds the boundary condition enforced by the delta function:

$$\phi_1(0^+) - \phi_1(0^-) = -\frac{i\eta}{v}\phi_2(x=0), \tag{3}$$
$$\phi_2(0^+) - \phi_2(0^-) = \frac{i\eta}{v}\phi_1(x=0). \tag{4}$$

Equations (3-4) away from $x = 0$ are solved by,

$$\phi_1(x) = \begin{cases} He^{\left(i\frac{Ex}{v}\right)} & \text{for } x > 0 \\ Ae^{\left(i\frac{Ex}{v}\right)} & \text{for } x < 0 \end{cases}, \tag{5}$$

$$\phi_2(x) = \begin{cases} Ge^{\left(-i\frac{Ex}{v}\right)} & \text{for } x > 0 \\ Be^{\left(-i\frac{Ex}{v}\right)} & \text{for } x < 0 \end{cases}. \tag{6}$$

The boundary conditions (3-4) then yields,

$$H - A = -\frac{i\eta}{v}\left(\frac{B+G}{2}\right),$$
$$G - B = +\frac{i\eta}{v}\left(\frac{A+H}{2}\right)$$

leading to the solution

$$H = -\frac{iG}{\left(\frac{v}{\eta}+\frac{\eta}{4v}\right)} + \frac{A\left(\frac{v}{\eta}-\frac{\eta}{4v}\right)}{\left(\frac{v}{\eta}+\frac{\eta}{4v}\right)},$$
$$B = -\frac{iA}{\left(\frac{v}{\eta}+\frac{\eta}{4v}\right)} + \frac{G\left(\frac{v}{\eta}-\frac{\eta}{4v}\right)}{\left(\frac{v}{\eta}+\frac{\eta}{4v}\right)}.$$

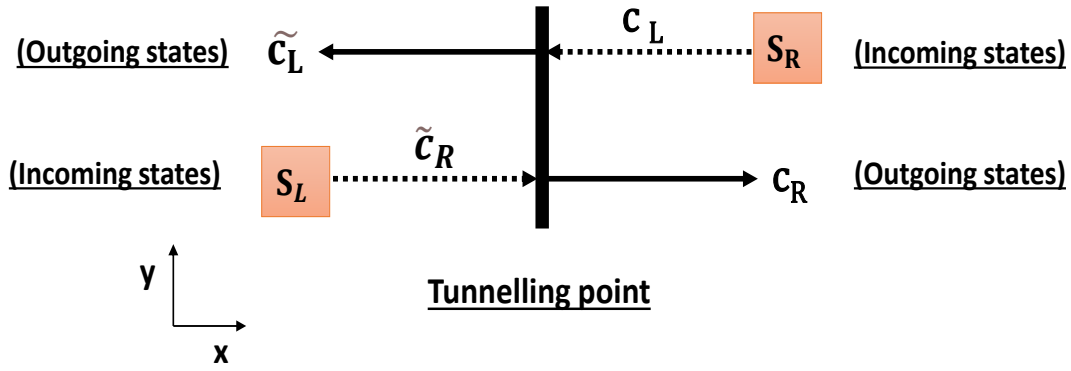

Figure B.1: **Scattering point of view on the QPC physics.** The sketch represents the QPC setup of Fig. [fig:1_QPC_experiment_scheme] with explicit connection to the wave function in Eqs. (3-4). S_L and S_R are the sources on the left and the right side of the QPC. The dotted lines represent the incoming edge states while the dark lines are the outgoing edge states.

Identifying A and G with the amplitudes of the incoming states, and H and B with those of outgoing states (cf. Fig. B.1), one can infer the transmission and reflection amplitudes.

Setting $G = 0$ (S_R is off), one finds

$$t_L = \frac{H}{A} = \frac{\left(\frac{v}{\eta}-\frac{\eta}{4v}\right)}{\left(\frac{v}{\eta}+\frac{\eta}{4v}\right)} = \frac{\left(1-\frac{\eta^2}{4v^2}\right)}{\left(1+\frac{\eta^2}{4v^2}\right)}, \tag{7}$$
$$r_L = \frac{B}{A} = \frac{-i}{\left(\frac{v}{\eta}+\frac{\eta}{4v}\right)}. \tag{8}$$

Similarly, setting $A = 0$ (S_L is off) leads to

$$t_R = \frac{B}{G} = \frac{\left(\frac{v}{\eta} - \frac{\eta}{4v}\right)}{\left(\frac{v}{\eta} + \frac{\eta}{4v}\right)} = \frac{\left(1 - \frac{\eta^2}{4v^2}\right)}{\left(1 + \frac{\eta^2}{4v^2}\right)}, \tag{9}$$

$$r_R = \frac{H}{G} = \frac{-i}{\left(\frac{v}{\eta} + \frac{\eta}{4v}\right)}. \tag{10}$$

One readily checks the unitarity of the scattering matrix $\mathcal{S}$ (1):

$$\mathcal{S}\mathcal{S}^\dagger = \mathcal{S}^\dagger\mathcal{S} = I,$$

where, I is the identity matrix. The transmission function

$$\mathcal{T}_{\text{pqpc}}(E) = |t_L|^2$$

is then given by Eq.(10).

C

Transmission function for wide QPC

Here we derive the transmission function for the wide-QPC model (Fig. 5.4), which is defined through Eqs. (11-13). Before providing the derivation in Sec. C, we discuss the properties of the extended region that features tunneling processes. For brevity of notation, we put $\hbar = 1$ in this section.

1. The properties of the region with tunneling

In order to understand the properties of the extended region that features tunneling processes, it is instructive to consider Hamiltonian

$$H = \int_{-\infty}^{+\infty} dx \left(-i\psi_1^\dagger v\partial_x\psi_1 + i\psi_2^\dagger v\partial_x\psi_2\right) + \zeta\int_{-\infty}^{+\infty} dx \left(\psi_1^\dagger(x)\,\psi_2(x) + \psi_2^\dagger(x)\,\psi_1(x)\right). \tag{1}$$

Compared to Eqs. (11-13), we have taken the tunneling region to be infinite.

Since the system is translationally invariant, one can represent the solution to the equations of motion

$$\partial_t\psi_1(x) = i\left[H,\psi_1(x)\right] = -v\partial_x\psi_1(x) - i\zeta\psi_2(x),$$
$$\partial_t\psi_2(x) = i\left[H,\psi_2(x)\right] = v\partial_x\psi_2(x) - i\zeta\psi_1(x),$$

in the form,

$$\psi_1(x) = \sum_k \hat{a}_k A_1 e^{ikx - iE_k t},$$
$$\psi_2(x) = \sum_k \hat{a}_k A_2 e^{ikx - iE_k t},$$

where, $\hat{a}_k$ are the fermionic annihilation operators. The equations of motion then yield

$$\begin{pmatrix} vk & \zeta \\ \zeta & -vk \end{pmatrix}\begin{pmatrix} A_1 \\ A_2 \end{pmatrix} = E_k \begin{pmatrix} A_1 \\ A_2 \end{pmatrix}$$

The solution of this equation for eigenmodes leads to the spectrum $E_k = \pm\sqrt{(vk)^2 + \zeta^2}$. We thus see that the region with tunneling features an energy gap of the size 2ζ (cf. Fig. C.1), which serves as an extended tunneling barrier in the wide-QPC model.

Note that the long-QPC model, cf. Fig. 5.6 and Eqs. (15-17), features the same Hamiltonian as the wide-QPC one — up to renaming $x \to y$, $\zeta \to \Delta$, and $W \to L$. The interpretation of the long-QPC model is very different, though. The tunneling region in the long-QPC model is designed to mimic the bulk of the system. Therefore, 2Δ is natural

to identify with the bulk gap. This was used to estimate the realistic model parameters in Sec. 5.3.

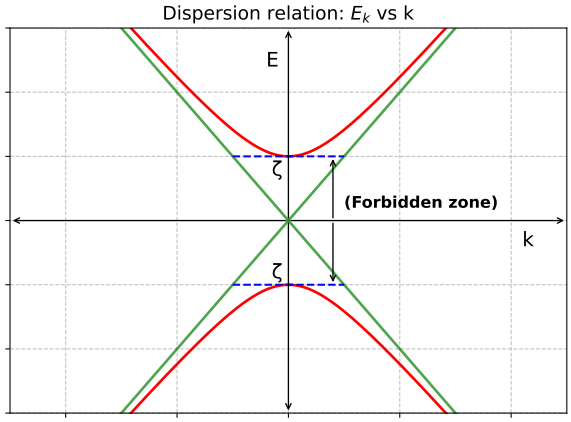

Figure C.1: Dispersion relation of the fermions in an infinite tunneling region, cf. Eq.(1). The dispersion relation of edges without tunneling $E_k = \pm vk$ is shown in green. In the presence of tunneling, $E_k = \pm\sqrt{(vk)^2 + \zeta^2}$ (red), exhibiting a forbidden zone of size 2ζ .
F

2. The transmission function

Now that we understand the effect of an extended region with tunneling, we are in position to derive the transmission function for the wide-QPC model. Starting from Eqs. (11-13), one obtains the equations of motion for the right-moving edge:

$$\partial_t \psi_1(x) = i\left[H, \psi_1(x)\right] = \begin{cases} -v\partial_x \psi_1(x), & x \notin (0, W), \\ -v\partial_x \psi_1(x) - i\zeta\psi_2(x), & x \in (0, W). \end{cases}$$

Similarly, for the left-moving edge:

$$\partial_t \psi_2(x) = i\left[H, \psi_2(x)\right] = \begin{cases} v\partial_x \psi_2(x), & x \notin (0, W), \\ v\partial_x \psi_2(x) - i\zeta\psi_1(x), & x \in (0, W). \end{cases}$$

Looking for the solution in the form (1-2), we find,

$$\frac{d}{dx}\begin{pmatrix} \phi_1(x) \\ \phi_2(x) \end{pmatrix} = \frac{i}{v}\begin{pmatrix} E & 0 \\ 0 & -E \end{pmatrix}\begin{pmatrix} \phi_1(x) \\ \phi_2(x) \end{pmatrix} \quad \text{for } x \in (0, W),$$

and

$$\frac{d}{dx}\begin{pmatrix} \phi_1(x) \\ \phi_2(x) \end{pmatrix} = \frac{i}{v}\begin{pmatrix} E & -\zeta \\ \zeta & -E \end{pmatrix}\begin{pmatrix} \phi_1(x) \\ \phi_2(x) \end{pmatrix} \quad \text{for } x \notin (0, W).$$

The wave function $\Phi(x) = (\phi_1(x), \phi_2(x))^{\mathrm{T}}$ can thus be expressed in three regions:

$$\Phi(x) = \begin{cases} \Phi_{\mathrm{I}} = \begin{pmatrix} Ae^{-iEx/v} \\ Be^{iEx/v} \end{pmatrix} = \begin{pmatrix} Ae^{-ikx} \\ Be^{ikx} \end{pmatrix}, & x < 0, \\ \Phi_{\mathrm{II}} = \frac{C}{\sqrt{2E(E+i\kappa v)}} \begin{pmatrix} E+i\kappa v \\ \zeta \end{pmatrix} e^{-\kappa x} + \frac{D}{\sqrt{2E(E+i\kappa v)}} \begin{pmatrix} \zeta \\ E+i\kappa v \end{pmatrix} e^{\kappa x}, & 0 < x < W, \\ \Phi_{\mathrm{III}} = \begin{pmatrix} He^{-iEx/v} \\ Ge^{iEx/v} \end{pmatrix} = \begin{pmatrix} He^{-ikx} \\ Ge^{ikx} \end{pmatrix}, & x > W. \end{cases} \tag{2}$$

Here $k = E/v$ and $\kappa = \sqrt{\zeta^2 - E^2}/v$.

The boundary conditions at $x = 0$ and $x = W$, enable expressing A, C, D, and G in terms of C and D.

$$\Phi_{\mathrm{I}}(x=0) = \Phi_{\mathrm{II}}(x=0)$$
$$\implies \begin{pmatrix} A \\ B \end{pmatrix} = \frac{C}{\sqrt{2E(E+i\kappa v)}} \begin{pmatrix} E+i\kappa v \\ \zeta \end{pmatrix} + \frac{D}{\sqrt{2E(E+i\kappa v)}} \begin{pmatrix} \zeta \\ E+i\kappa v \end{pmatrix}, \tag{3}$$

$$\Phi_{\mathrm{II}}(x=W) = \Phi_{\mathrm{III}}(x=W) \tag{4}$$
$$\implies \frac{C}{\sqrt{2E(E+i\kappa v)}} \begin{pmatrix} E+i\kappa v \\ \zeta \end{pmatrix} e^{-\kappa W} + \frac{D}{\sqrt{2E(E+i\kappa v)}} \begin{pmatrix} \zeta \\ E+i\kappa v \end{pmatrix} e^{\kappa W} = \begin{pmatrix} He^{-ikW} \\ Ge^{ikW} \end{pmatrix}.$$

Denoting

$$\alpha = E + i\kappa v, \beta = \zeta, \gamma = \sqrt{2E(E+i\kappa v)},$$
$$\text{and } e^{\pm\kappa W} = \cosh(\kappa W) \pm \sinh(\kappa W)$$

one can write

$$\gamma A = \alpha C + \beta D,\ \gamma B = \alpha D + \beta C, \tag{5}$$
$$\gamma H = e^{ikW}\left[\alpha C e^{-\kappa W} + \beta D e^{\kappa W}\right],\ \gamma G = e^{-ikW}\left[\beta C e^{-\kappa W} + \alpha D e^{\kappa W}\right]. \tag{6}$$

Conversely,

$$C = \frac{\gamma(\alpha A - \beta B)}{(\alpha^2 - \beta^2)}, \quad D = \frac{\gamma(\alpha B - \beta A)}{(\alpha^2 - \beta^2)},$$

which enables one to find H and G in terms of A and B:

$$H = e^{ikW}\left[\left(\cosh(\kappa W) + \left(\frac{iE}{\kappa v}\right)\sinh(\kappa W)\right)A - \left(\frac{i\zeta}{\kappa v}\right)\sinh(\kappa W)\,B\right],$$
$$G = e^{-ikW}\left[\left(\cosh(\kappa W) - \left(\frac{iE}{\kappa v}\right)\sinh(\kappa W)\right)B + \left(\frac{i\zeta}{\kappa v}\right)\sinh(\kappa W)\,A\right].$$

Here we used relations

$$\frac{\alpha^2 + \beta^2}{\alpha^2 - \beta^2} = \frac{-iE}{\kappa v}, \quad \frac{2\alpha\beta}{\alpha^2 - \beta^2} = \frac{-i\zeta}{\kappa v}.$$

Similarly to the consideration in Appendix B, one can find the transmission and reflection amplitudes. Setting $A = 0$ (switching off S_L) leads to

$$t_R = \frac{B}{G} = \frac{(\kappa v)\, e^{ikW}}{(\kappa v)\cosh(\kappa W) - iE\sinh(\kappa W)}, \tag{7}$$

$$r_R = \frac{H}{G} = -\frac{i\zeta \sinh(\kappa W)\, e^{2ikW}}{(\kappa v)\cosh(\kappa W) - iE\sinh(\kappa W)} \tag{8}$$

Setting $G = 0$ (switching off S_R), one gets

$$t_L = \frac{H}{A} = \frac{(\kappa v)\, e^{ikW}}{(\kappa v)\cosh(\kappa W) - iE\sinh(\kappa W)}, \tag{9}$$

$$r_L = \frac{B}{A} = -\frac{i\zeta \sinh(\kappa W)}{(\kappa v)\cosh(\kappa W) - iE\sinh(\kappa W)}. \tag{10}$$

One checks that the unitarity of the $\mathcal{S}$-matrix is satisfied. The transmission function

$$\mathcal{T}_{\text{wqpc}}(E) = |t_L|^2 = \left(1 + \zeta^2 \sinh^2(\kappa W) \,/\, (\kappa v)^2\right)^{-1}$$

can be represented as Eq.(14).

D

Point limit of transmission function in conventional quantum mechanics

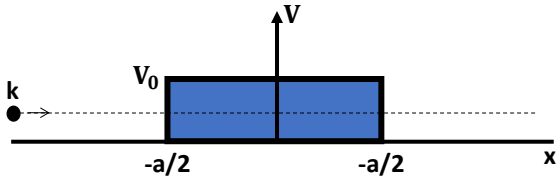

Figure D.1: Rectangular potential barrier.

Here we discuss the point limit of a rectangular barrier for a conventional quantum particle with dispersion relation $p^2/(2m)$. For brevity of notation, we put $\hbar = 1$ in this section.

Consider Hamiltonian

$$H = \int_{-\infty}^{+\infty} dx \left(-\psi^\dagger(x) \frac{\partial_x^2}{2m} \psi(x) + V(x) \psi^\dagger(x) \psi(x) \right),$$

where the potential

$$V(x) = \begin{cases} V_0, & |x| < \frac{a}{2}, \\ 0, & |x| > \frac{a}{2}. \end{cases}$$

For energies $E \leq V_0$ this potential represents a potential barrier for a quantum particle, cf. Fig. D.1. The probability for a particle to be transmitted through the barrier is given by ([Band and Avishai, 2013, Section 1.3.11])

$$\mathcal{T}_{\text{rect}}(E) = \left(1 + \frac{\sinh^2(\kappa a)}{4} \left[\frac{\kappa^2 + k^2}{k\kappa} \right]^2 \right)^{-1},$$

where$k = \sqrt{2mE}$, and $\kappa = \sqrt{2m(V_0 - E)}$.

Putting $V_0 = \alpha/a$ and taking the limit a\rightarrow0 makes the potential a delta-function barrier: $V(x) = \alpha\delta(x)$. The transmission probability for the delta potential is given by ([Band and Avishai, 2013, Section 1.3.12])

$$\mathcal{T}_{\text{delta}}(E) = \left(1 + [m\alpha/k]^2 \right)^{-1}.$$

This expression can be reproduced by taking the limit of $\mathcal{T}_{\text{rect}}(E)$. Indeed, in the limit $V_0 = \alpha/a$, $a \to 0$,

$$\kappa \approx \sqrt{2mV_0} = \sqrt{2m\alpha/a} \to \infty,$$
$$\kappa a \approx \sqrt{2m\alpha a} \to 0, \sinh(\kappa a) \approx \kappa a,$$

so that

$$\frac{\sinh^2(\kappa a)}{4}\left[\frac{\kappa^2+k^2}{k\kappa}\right]^2 \approx \frac{(\kappa a)^2}{4}\left[\frac{\kappa}{k}\right]^2 = \left[\frac{\kappa^2 a}{2k}\right]^2 = \left[\frac{m\alpha}{k}\right]^2.$$

Therefore,

$$\lim_{a\to 0,\, V_0=\alpha/a} \mathcal{T}_{\text{rect}}(E) = \mathcal{T}_{\text{delta}}(E).$$

This consideration shows that in the conventional quantum-mechanical problem with dispersion relation $p^2/(2m)$, the properties of a delta-barrier can be obtained from the properties of the narrow and high rectangular potential. Contrast this to the consideration of Sec. (5.2)the transmission function $\mathcal{T}_{\text{pqpc}}(E)$ obtained from the point-QPC model (which corresponds to delta-tunneling at $x = 0$) does not coincide with the point limit of the transmission functions obtained from the wide-QPC and long-QPC models ($\mathcal{T}_{\text{wqpc}}(E)$ and $\mathcal{T}_{\text{lqpc}}(E)$). It would be interesting to check whether taking a non-linear edge dispersion in the point-, wide-, and long-QPC models would fix this discrepancy.

E

The role of edge velocity

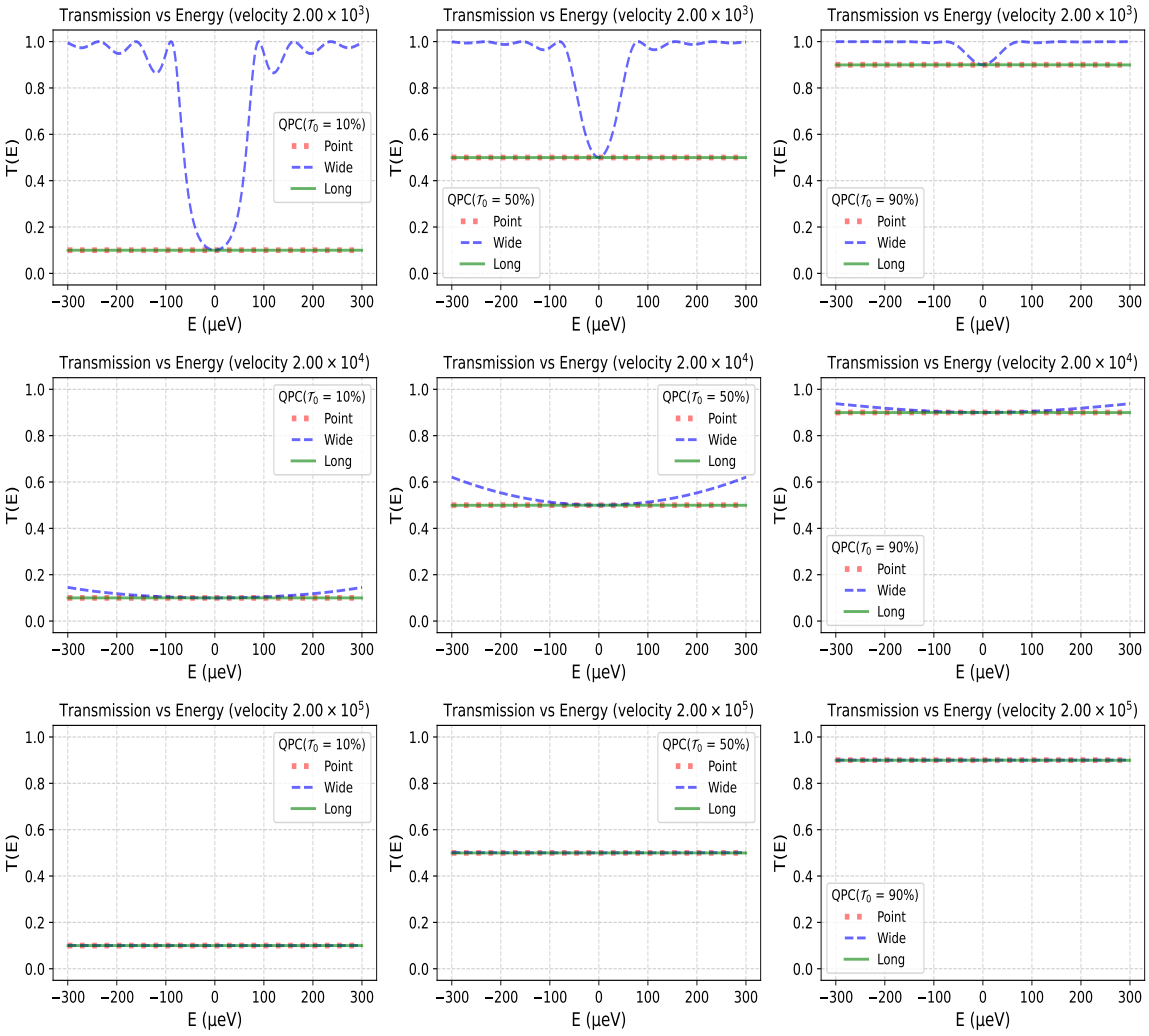

Figure E.1: Comparative study of the transmission characteristics for three different velocities. The characteristics display a clear dependence on the velocity as a parameter.

In the main text (cf. Fig. 5.8), we have discussed the results for the transmission function behavior when using realistic parameters. We chose the value of velocity $v = 2 \times 10^4$ m/s for consideration there. Here we demonstrate the effect of velocity value. In experiments, values in the range of $v = 10^4$–10^6 m/s have been reported ([McClure et al., 2009, Gurman et al., 2016, Kamata et al., 2010, Kumada et al., 2011, Kataoka et al., 2016, Nakamura et al., 2019, 2020, Weldeyesus et al., 2025])

We take the same parameters as in the main text and plot the transmission function for $v = 2 \times 10^3, 2 \times 10^4$, and 2×10^5 m/s. The results are presented in Fig. (5.8). One observes that velocity strongly affects the predictions of the wide-QPC model for all values of $\mathcal{T}_0$. The point-QPC prediction is unaffected as it is equal to $\mathcal{T}_0$ for all energies. Similarly, the long-QPC model is also hardly affected since its transmission function is fully determined by $\mathcal{T}_0$ when $E \ll \Delta$. This shows that whenever energy dependence of the transmission function is significant, the edge state velocity is an important factor.

F

Noise calculations for four-terminal device

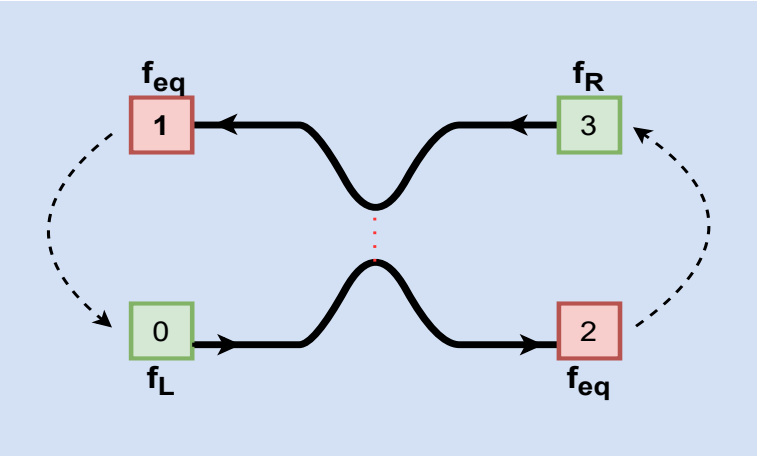

Figure F.1: **Schematic for four-terminal setup**. The f_L and f_R are the left and the right Fermi-distribution respectively. The f_{eq} is the equilibrium distribution at the $\mu = 0$.

For the above setup (1), the corresponding S-matrix is:

$$S_{\alpha\beta} = \begin{bmatrix} 0 & 1 & 0 & 0 \\ r & 0 & 0 & t \\ t & 0 & 0 & -r \\ 0 & 0 & 1 & 0 \end{bmatrix} \tag{1}$$

One can verify the unitary of the above matrix as $S^\dagger S = I$. The noise is of two possible kind: auto-correlation and cross-correlation. We derive below the auto-correlated

noise at terminal which corresponds to the indices $\alpha = \beta = 2$. Thus, Eq.(24) gives the following expression,

$$\begin{aligned} S_{22} = \frac{e^2}{\pi\hbar}\int dE \left[s_{20}^{\dagger}s_{20}\right]\left[s_{20}^{\dagger}s_{20}\right]\{f_0\left(1-f_0\right)+f_0\left(1-f_0\right)\} \\ +\left[s_{21}^{\dagger}s_{20}\right]\left[s_{21}^{\dagger}s_{20}\right]\{f_0\left(1-f_1\right)+f_1\left(1-f_0\right)\}+ \\ ...+\left[s_{23}^{\dagger}s_{20}\right]\left[s_{23}^{\dagger}s_{20}\right]\{f_3\left(1-f_0\right)+f_0\left(1-f_3\right)\} \\ +\left[1-s_{22}^{\dagger}s_{22}\right]\left[s_{22}^{\dagger}s_{22}\right]\{f_2\left(1-f_2\right)+f_2\left(1-f_2\right)\}+ \\ ...+\left[s_{20}^{\dagger}s_{23}\right]\left[s_{20}^{\dagger}s_{23}\right]\{f_0\left(1-f_3\right)+f_3\left(1-f_0\right)\}...+ \\ \left[s_{23}^{\dagger}s_{23}\right]\left[s_{23}^{\dagger}s_{23}\right]\{f_3\left(1-f_3\right)+f_3\left(1-f_3\right)\} \end{aligned} \quad (2)$$

Matching the corresponding elements from the above S-matrix(1) and since matrix elements being real, it imposes $s_{\alpha\beta}^{\dagger} = s_{\alpha\beta}^{*}$:

$$\begin{aligned} S_{22} = \frac{e^2}{\pi\hbar}\int dE\Big[2r^2r^{*2}\left(1-f_3\right)f_3+2rtr^*t^*\left\{\left(1-f_0\right)f_3+\left(1-f_3\right)f_0\right\} \\ +2t^2t^{*2}\left(1-f_0\right)f_0+2\left(1-f_2\right)f_2\Big] \end{aligned} \quad (3)$$

With $1-|r|^2 = |t|^2 = \mathcal{T}$, one evaluates the auto-correlated shot noise:

$$\begin{aligned} S_{22} = \frac{2e^2}{\pi\hbar}\int dE\Big[\left(1-\mathcal{T}\right)^2\left(1-f_R\right)f_R \\ +\left(1-\mathcal{T}\right)\mathcal{T}\left\{\left(1-f_L\right)f_R+\left(1-f_R\right)f_L\right\}+\mathcal{T}^2\left(1-f_L\right)f_L+\left(1-f_{eq}\right)f_{eq}\Big] \end{aligned} \quad (4)$$

Taking the contributions from all energies, the total shot noise is,

$$S_{22} = \int_{-\infty}^{\infty} dE\left(S_1+S_2+S_3+S_4\right)$$

where,

$$S = \begin{cases} S_1 & = \left(1-\mathcal{T}\right)^2\left(1-f_R\right)f_R \\ S_2 & = \left(1-\mathcal{T}\right)\mathcal{T}\left\{\left(1-f_L\right)f_R+\left(1-f_R\right)f_L\right\} \\ S_3 & = \mathcal{T}^2\left(1-f_L\right)f_L \\ S_4 & = 2\left(1-f_{eq}\right)f_{eq} \end{cases} \quad (5)$$

For the constant transmission $\mathcal{T} = \bar{\mathcal{T}}$:

$$S_1 = \left(1-\bar{\mathcal{T}}\right)^2\int_{-\infty}^{\infty} dE\left(1-f_R\right)f_R = k_BT\left(1-\bar{\mathcal{T}}\right)^2 \quad (6)$$

$$S_2 = \bar{\mathcal{T}}\left(1-\bar{\mathcal{T}}\right)\int_{-\infty}^{\infty} dE\left[\left(1-f_L\right)f_R+\left(1-f_R\right)f_L\right] \quad (7)$$

$$S_3 = \left(\bar{\mathcal{T}}\right)^2\int_{-\infty}^{\infty} dE\left(1-f_L\right)f_L = k_BT\left(\bar{\mathcal{T}}\right)^2 \quad (8)$$

On computing the above integrals, one obtains the final expression for the **four-terminal shot noise at constant transmission** $\bar{\mathcal{T}}$ as,

$$S_{22} = 4k_BTg_0 + 2eVg_0\left[\coth\left(\frac{eV}{2k_BT}\right) - \frac{2k_BT}{eV}\right]\bar{\mathcal{T}}\left(1-\bar{\mathcal{T}}\right), \text{ where } g_0 = \frac{e^2}{\pi\hbar} \quad (9)$$

G

DC Mach-Zehnder Interferometer

1. *Semi-analytical transmission formula for DC Mach-Zehnder Interferometer*

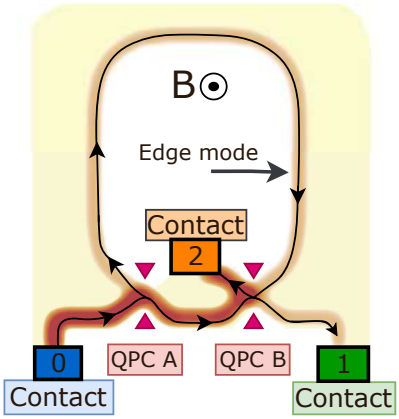

Figure G.1: The Mach-Zehnder interferometer.

Consider a beam of electrons coming form the left side and split into two parts by the application of the splitter (QPCs), with r_{A} (reflection) and the t_{A} (transmission) coefficients. Similarly, the reflected beam passed from QPC A split at QPC B into two beams with the coefficients r_{B} as reflection and t_{B} as transmission coefficients respectively. Now, at each beam splitting points:

$$|r_A|^2 + |d_A|^2 = 1$$
$$t_{\mathrm{total}} = t_B t_A + e^{-i\Phi} r_A r_B$$

where, $\Phi = \frac{B.S}{\hbar/e}$. Here, B is the external magnetic field and S is the area of interference loop by the two respective arms of the interferometer.

Now, the total transmission,

$$D_{\mathrm{tot}} = |d_{\mathrm{tot}}|^2 = |d_B d_A|^2 + |e^{-\iota\Phi} r_A r_B|^2 + 2|d_A d_B r_A r_B e^{-i\Phi}|$$

Assuming the following convention:

$$D_A = |d_A|^2 \text{ and } D_B = |d_B|^2,$$

$$D_{tot} = D_A D_B + (1 - D_A)(1 - D_B) + 2\cos(\Phi)\sqrt{D_A D_B (1 - D_A)(1 - D_B)} \quad (1)$$

2. Discretisation effect

We saw the convergence of the true area with the fit area of the loop as one increases the sample length. For the smaller sample the gained phase over the arms is way bigger than lattice discretisation and thus one needs larger sample size to tune the Hofstadter's physics right and gain appropriately smaller phase across the arms. A comparative studies with simple length and fit is presented in Fig. (G.2).

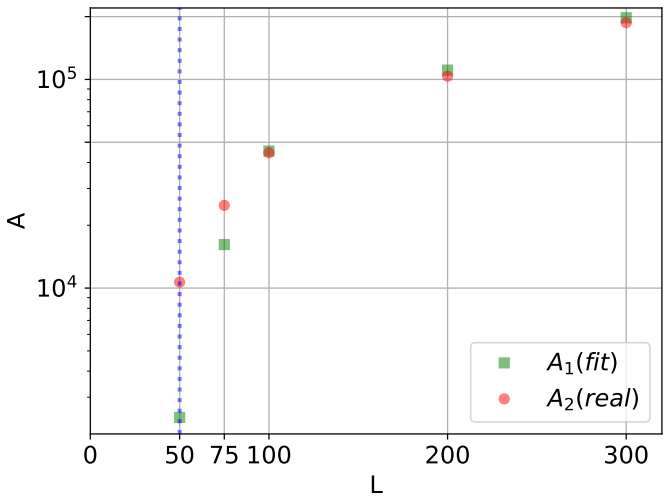

Figure G.2: True versus fit area convergence with increase in sample length sample length.

Part VI

BIBLIOGRAPHY

Bibliography

P. W. Anderson. More is different. *Science*, 177:393–396, 8 1972. ISSN 0036-8075. doi: 10.1126/science.177.4047.393.

Pacome Armagnat, A. Lacerda-Santos, Benoit Rossignol, Christoph Groth, and Xavier Waintal. The self-consistent quantum-electrostatic problem in strongly non-linear regime. *SciPost Physics*, 7:031, 9 2019. ISSN 2542-4653. doi: 10.21468/SciPostPhys.7.3.031.

Yehuda B. Band and Yshai Avishai. *Electronic Properties of Solids*, pages 381–544. Elsevier, 2013. ISBN 9780444537874. doi: 10.1016/B978-0-444-53786-7.00009-5. URL https://linkinghub.elsevier.com/retrieve/pii/B9780444537867000095.

H. Bartolomei, M. Kumar, R. Bisognin, A. Marguerite, J.-M. Berroir, E. Bocquillon, B. Plaçais, A. Cavanna, Q. Dong, U. Gennser, Y. Jin, and G. Fève. Fractional statistics in anyon collisions. *Science*, 368:173–177, 4 2020. ISSN 0036-8075. doi: 10.1126/science.aaz5601.

Florian Bauer, Jan Heyder, Enrico Schubert, David Borowsky, Daniela Taubert, Benedikt Bruognolo, Dieter Schuh, Werner Wegscheider, Jan von Delft, and Stefan Ludwig. Microscopic origin of the '0.7-anomaly' in quantum point contacts. *Nature*, 501:73–78, 9 2013. ISSN 0028-0836. doi: 10.1038/nature12421.

Ya.M. Blanter and M. Büttiker. Shot noise in mesoscopic conductors. *Physics Reports*, 336:1–166, 9 2000. ISSN 03701573. doi: 10.1016/S0370-1573(99)00123-4.

M Buttiker. Capacitance, admittance, and rectification properties of small conductors. *Journal of Physics: Condensed Matter*, 5:9361–9378, 12 1993. ISSN 0953-8984. doi: 10.1088/0953-8984/5/50/017.

Chris Bäuerle. Private communication, 2025. From private communication with Chris Bäuerle.

Christopher Bäuerle, D Christian Glattli, Tristan Meunier, Fabien Portier, Patrice Roche, Preden Roulleau, Shintaro Takada, and Xavier Waintal. Coherent control of single electrons: a review of current progress. *Reports on Progress in Physics*, 81:056503, 5 2018. ISSN 0034-4885. doi: 10.1088/1361-6633/aaa98a.

M. Büttiker. Absence of backscattering in the quantum hall effect in multiprobe conductors. *Physical Review B*, 38:9375–9389, 11 1988. ISSN 0163-1829. doi: 10.1103/PhysRevB.38.9375.

M. Büttiker. Time-dependent current partition in mesoscopic conductors. *Il Nuovo Cimento B*, 110:509–522, 5 1995. ISSN 1826-9877. doi: 10.1007/BF02741461.

Eleni Chatzikyriakou, Junliang Wang, Lucas Mazzella, Antonio Lacerda-Santos, Maria Cecilia da Silva Figueira, Alex Trellakis, Stefan Birner, Thomas Grange, Christopher Bäuerle, and Xavier Waintal. Unveiling the charge distribution of a gaas-based nanoelectronic device: A large experimental dataset approach. *Physical Review Research*, 4: 043163, 12 2022. ISSN 2643-1564. doi: 10.1103/PhysRevResearch.4.043163.

D. B. Chklovskii, B. I. Shklovskii, and L. I. Glazman. Electrostatics of edge channels. *Physical Review B*, 46:4026–4034, 8 1992. ISSN 0163-1829. doi: 10.1103/PhysRevB.46.4026.

Y. C. Chung, M. Heiblum, and V. Umansky. Scattering of bunched fractionally charged quasiparticles. *Physical Review Letters*, 91:216804, 11 2003. ISSN 0031-9007. doi: 10.1103/PhysRevLett.91.216804.

R. de Picciotto, M. Reznikov, M. Heiblum, V. Umansky, G. Bunin, and D. Mahalu. Direct observation of a fractional charge. *Nature*, 389:162–164, 9 1997. ISSN 0028-0836. doi: 10.1038/38241.

R. Dingle, H. L. Störmer, A. C. Gossard, and W. Wiegmann. Electron mobilities in modulation-doped semiconductor heterojunction superlattices. *Applied Physics Letters*, 33:665–667, 10 1978. ISSN 0003-6951. doi: 10.1063/1.90457.

M. Dolev, M. Heiblum, V. Umansky, Ady Stern, and D. Mahalu. Observation of a quarter of an electron charge at the $\nu = 5/2$ quantum hall state. *Nature*, 452:829–834, 4 2008. ISSN 0028-0836. doi: 10.1038/nature06855.

Hermann Edlbauer, Junliang Wang, Thierry Crozes, Pierre Perrier, Seddik Ouacel, Clément Geffroy, Giorgos Georgiou, Eleni Chatzikyriakou, Antonio Lacerda-Santos, Xavier Waintal, D. Christian Glattli, Preden Roulleau, Jayshankar Nath, Masaya Kataoka, Janine Splettstoesser, Matteo Acciai, Maria Cecilia da Silva Figueira, Kemal Öztas, Alex Trellakis, Thomas Grange, Oleg M. Yevtushenko, Stefan Birner, and Christopher Bäuerle. Semiconductor-based electron flying qubits: review on recent progress accelerated by numerical modelling. *EPJ Quantum Technology*, 9(1):21, 2022. ISSN 2196-0763. doi: 10.1140/epjqt/s40507-022-00139-w. URL https://doi.org/10.1140/epjqt/s40507-022-00139-w.

Joseph Falson, Daniela Tabrea, Ding Zhang, Inti Sodemann, Yusuke Kozuka, Atsushi Tsukazaki, Masashi Kawasaki, Klaus von Klitzing, and Jurgen H. Smet. A cascade of phase transitions in an orbitally mixed half-filled landau level. *Science Advances*, 4, 9 2018. ISSN 2375-2548. doi: 10.1126/sciadv.aat8742.

G. Fano, F. Ortolani, and E. Colombo. Configuration-interaction calculations on the fractional quantum hall effect. *Physical Review B*, 34:2670–2680, 8 1986. ISSN 0163-1829. doi: 10.1103/PhysRevB.34.2670.

P Fendley, A W W Ludwig, and H Saleur. Exact nonequilibrium transport through point contacts in quantum wires and fractional quantum hall devices. *Physical Review B*, 52: 8934–8950, 1995a. URL http://link.aps.org/doi/10.1103/PhysRevB.52.8934.

P Fendley, A W W Ludwig, and H Saleur. Exact nonequilibrium dc shot noise in luttinger liquids and fractional quantum hall devices. *Physical Review Letters*, 75:2196, 1995b. URL http://dx.doi.org/10.1103/PhysRevLett.75.2196.

Yuriel Núñez Fernández, Matthieu Jeannin, Philipp T. Dumitrescu, Thomas Kloss, Jason Kaye, Olivier Parcollet, and Xavier Waintal. Learning feynman diagrams with tensor trains. *Physical Review X*, 12:041018, 11 2022. ISSN 2160-3308. doi: 10.1103/PhysRevX.12.041018.

Michele Filippone and Piet W. Brouwer. Tunneling into quantum wires: Regularization of the tunneling hamiltonian and consistency between free and bosonized fermions. *Physical Review B*, 94:235426, 12 2016. ISSN 2469-9950. doi: 10.1103/PhysRevB.94.235426. URL http://arxiv.org/abs/1606.03465http://dx.doi.org/10.1103/PhysRevB.94.235426https://link.aps.org/doi/10.1103/PhysRevB.94.235426.

Benoit Gaury and Xavier Waintal. Dynamical control of interference using voltage pulses in the quantum regime. *Nature Communications*, 5:3844, 5 2014. ISSN 2041-1723. doi: 10.1038/ncomms4844. URL https://www.nature.com/articles/ncomms4844.

Benoit Gaury, Joseph Weston, and Xavier Waintal. Stopping electrons with radio-frequency pulses in the quantum hall regime. *Physical Review B*, 90:161305, 10 2014. ISSN 1098-0121. doi: 10.1103/PhysRevB.90.161305. URL https://link.aps.org/doi/10.1103/PhysRevB.90.161305.

Benoit Gaury, Joseph Weston, and Xavier Waintal. The a.c. josephson effect without superconductivity. *Nature Communications*, 6:6524, 3 2015. ISSN 2041-1723. doi: 10.1038/ncomms7524. URL https://www.nature.com/articles/ncomms7524.

Steven M. Girvin and Kun Yang. *Modern Condensed Matter Physics*. Cambridge University Press, 2 2019. ISBN 9781316480649. doi: 10.1017/9781316480649.

Christoph W Groth, Michael Wimmer, Anton R Akhmerov, and Xavier Waintal. Kwant: a software package for quantum transport. *New Journal of Physics*, 16:063065, 6 2014. ISSN 1367-2630. doi: 10.1088/1367-2630/16/6/063065.

Itamar Gurman, Ron Sabo, Moty Heiblum, Vladimir Umansky, and Diana Mahalu. Dephasing of an electronic two-path interferometer. *Physical Review B*, 93:121412(R), 2 2016. doi: 10.1103/PhysRevB.93.121412. URL http://link.aps.org/doi/10.1103/PhysRevB.93.121412http://arxiv.org/abs/1602.01586.

Geraldine Haack, Michael Moskalets, Janine Splettstoesser, and Markus Buttiker. Coherence of single-electron sources from mach-zehnder interferometry. *Phys. Rev. B*, 84:081303, Aug 2011. doi: 10.1103/PhysRevB.84.081303. URL https://link.aps.org/doi/10.1103/PhysRevB.84.081303.

B. I. Halperin, Patrick A. Lee, and Nicholas Read. Theory of the half-filled landau level. *Physical Review B*, 47:7312–7343, 3 1993. ISSN 0163-1829. doi: 10.1103/PhysRevB.47.7312.

Bertrand I Halperin and Jainendra K Jain. *Fractional Quantum Hall Effects*. WORLD SCIENTIFIC, 6 2020. ISBN 978-981-12-1748-7. doi: 10.1142/11751.

R. J. Haug, A. H. MacDonald, P. Streda, and K. von Klitzing. Quantized multichannel magnetotransport through a barrier in two dimensions. *Physical Review Letters*, 61: 2797–2800, 12 1988. ISSN 0031-9007. doi: 10.1103/PhysRevLett.61.2797.

O Heinonen. *Composite Fermions*. WORLD SCIENTIFIC, 10 1998. ISBN 978-981-02-3592-5. doi: 10.1142/3894.

Douglas R. Hofstadter. Energy levels and wave functions of bloch electrons in rational and irrational magnetic fields. *Physical Review B*, 14:2239–2249, 9 1976. ISSN 0556-2805. doi: 10.1103/PhysRevB.14.2239.

J. K. Jain and R. K. Kamilla. Quantitative study of large composite-fermion systems. *Physical Review B*, 55:R4895–R4898, 2 1997. ISSN 0163-1829. doi: 10.1103/PhysRevB.55.R4895.

Yang Ji, Yunchul Chung, D. Sprinzak, M. Heiblum, D. Mahalu, and Hadas Shtrikman. An electronic mach–zehnder interferometer. *Nature*, 422:415–418, 3 2003. ISSN 0028-0836. doi: 10.1038/nature01503. URL https://www.nature.com/articles/nature01503.

Dawon Kahng. Electric field controlled semiconductor device, 8 1963.

H. Kamata, T. Ota, K. Muraki, and T. Fujisawa. Voltage-controlled group velocity of edge magnetoplasmon in the quantum hall regime. *Physical Review B*, 81:085329, 2 2010. ISSN 1098-0121. doi: 10.1103/PhysRevB.81.085329. URL https://link.aps.org/doi/10.1103/PhysRevB.81.085329.

M. Kataoka, N. Johnson, C. Emary, P. See, J. P. Griffiths, G. A. C. Jones, I. Farrer, D. A. Ritchie, M. Pepper, and T. J. B. M. Janssen. Time-of-flight measurements of single-electron wave packets in quantum hall edge states. *Physical Review Letters*, 116:126803, 3 2016. ISSN 0031-9007. doi: 10.1103/PhysRevLett.116.126803. URL https://link.aps.org/doi/10.1103/PhysRevLett.116.126803.

Thomas Kloss, Joseph Weston, and Xavier Waintal. Transient and sharvin resistances of luttinger liquids. *Physical Review B*, 97:165134, 4 2018. ISSN 2469-9950. doi: 10.1103/PhysRevB.97.165134. URL https://link.aps.org/doi/10.1103/PhysRevB.97.165134.

Thomas Kloss, Joseph Weston, Benoit Gaury, Benoit Rossignol, Christoph Groth, and Xavier Waintal. Tkwant: a software package for time-dependent quantum transport. *New Journal of Physics*, 23:023025, 2 2021. ISSN 1367-2630. doi: 10.1088/1367-2630/abddf7.

J M Kosterlitz and D J Thouless. Ordering, metastability and phase transitions in two-dimensional systems. *Journal of Physics C: Solid State Physics*, 6:1181–1203, 4 1973. ISSN 0022-3719. doi: 10.1088/0022-3719/6/7/010.

N. Kumada, H. Kamata, and T. Fujisawa. Edge magnetoplasmon transport in gated and ungated quantum hall systems. *Physical Review B*, 84:045314, 7 2011. ISSN 1098-0121. doi: 10.1103/PhysRevB.84.045314. URL https://link.aps.org/doi/10.1103/PhysRevB.84.045314.

Landau L. *ON THE THEORY OF PHASE TRANSITIONS*, pages 193–216. Elsevier, 1965. doi: 10.1016/B978-0-08-010586-4.50034-1.

Pui K. Lam and S. M. Girvin. Liquid-solid transition and the fractional quantum-hall effect. *Physical Review B*, 30:473–475, 7 1984. ISSN 0163-1829. doi: 10.1103/PhysRevB.30.473.

R. B. Laughlin. Anomalous quantum hall effect: An incompressible quantum fluid with fractionally charged excitations. *Physical Review Letters*, 50:1395–1398, 5 1983. ISSN 0031-9007. doi: 10.1103/PhysRevLett.50.1395.

Robert B. Laughlin. *Elementary Theory: the Incompressible Quantum Fluid*, pages 233–301. 1990. doi: 10.1007/978-1-4612-3350-3_7. URL http://link.springer.com/10.1007/978-1-4612-3350-3_7.

Ivan Levkivskyi. *Mesoscopic Quantum Hall Effect*. Springer Berlin Heidelberg, 2012. ISBN 978-3-642-30498-9. doi: 10.1007/978-3-642-30499-6. URL https://link.springer.com/10.1007/978-3-642-30499-6.

R. C. Liu, B. Odom, Y. Yamamoto, and S. Tarucha. Quantum interference in electron collision. *Nature*, 391:263–265, 1 1998. ISSN 0028-0836. doi: 10.1038/34611.

Th Martin and R Landauer. Wave-packet approach to noise in multichannel mesoscopic systems. *Physical Review B*, 45:1742–1755, 1992. URL http://link.aps.org/doi/10.1103/PhysRevB.45.1742.

K. A. Matveev and L. I. Glazman. Coulomb blockade of tunneling into a quasi-one-dimensional wire. *Physical Review Letters*, 70:990–993, 2 1993. ISSN 0031-9007. doi: 10.1103/PhysRevLett.70.990. URL https://link.aps.org/doi/10.1103/PhysRevLett.70.990.

D. T. McClure, Yiming Zhang, B. Rosenow, E. M. Levenson-Falk, C. M. Marcus, L. N. Pfeiffer, and K. W. West. Edge-state velocity and coherence in a quantum hall fabry-perot interferometer. *Physical Review Letters*, 103:206806, 11 2009. ISSN 0031-9007. doi: 10.1103/PhysRevLett.103.206806. URL https://link.aps.org/doi/10.1103/PhysRevLett.103.206806.

Maciej Misiorny, Gwendal Fève, and Janine Splettstoesser. Shaping charge excitations in chiral edge states with a time-dependent gate voltage. *Phys. Rev. B*, 97:075426, Feb 2018. doi: 10.1103/PhysRevB.97.075426. URL https://link.aps.org/doi/10.1103/PhysRevB.97.075426.

Gregory Moore and Nicholas Read. Nonabelions in the fractional quantum hall effect. *Nuclear Physics B*, 360:362–396, 8 1991. ISSN 05503213. doi: 10.1016/0550-3213(91)90407-O.

Michael V Moskalets. *Scattering Matrix Approach to Non-Stationary Quantum Transport*. IMPERIAL COLLEGE PRESS, 9 2011. ISBN 978-1-84816-834-3. doi: 10.1142/p822.

J. Nakamura, S. Fallahi, H. Sahasrabudhe, R. Rahman, S. Liang, G. C. Gardner, and M. J. Manfra. Aharonov–bohm interference of fractional quantum hall edge modes. *Nature Physics*, 15:563–569, 6 2019. ISSN 1745-2473. doi: 10.1038/s41567-019-0441-8. URL https://www.nature.com/articles/s41567-019-0441-8.

J. Nakamura, S. Liang, G. C. Gardner, and M. J. Manfra. Direct observation of anyonic braiding statistics. *Nature Physics*, 16:931–936, 9 2020. ISSN 1745-2473. doi: 10.1038/s41567-020-1019-1. URL https://www.nature.com/articles/s41567-020-1019-1.

J. Nakamura, S. Liang, G. C. Gardner, and M. J. Manfra. Impact of bulk-edge coupling on observation of anyonic braiding statistics in quantum hall interferometers. *Nature Communications*, 13:344, 1 2022. ISSN 2041-1723. doi: 10.1038/s41467-022-27958-w.

Yuli V. Nazarov and Yaroslav M. Blanter. *Quantum Transport*. Cambridge University Press, 5 2009. ISBN 9780521832465. doi: 10.1017/CBO9780511626906.

John W. Negele and Henri Orland. *Quantum Many-Particle Systems*. CRC Press, 3 2018. ISBN 9780429497926. doi: 10.1201/9780429497926.

M. Reznikov, R. de Picciotto, T. G. Griffiths, M. Heiblum, and V. Umansky. Observation of quasiparticles with one-fifth of an electron's charge. *Nature*, 399:238–241, 5 1999. ISSN 0028-0836. doi: 10.1038/20384.

Preden Roulleau, F. Portier, P. Roche, A. Cavanna, G. Faini, U. Gennser, and D. Mailly. Direct measurement of the coherence length of edge states in the integer quantum hall regime. *Physical Review Letters*, 100:126802, 3 2008. ISSN 0031-9007. doi: 10.1103/PhysRevLett.100.126802. URL https://link.aps.org/doi/10.1103/PhysRevLett.100.126802.

Gregoire Roussely, Everton Arrighi, Giorgos Georgiou, Shintaro Takada, Martin Schalk, Matias Urdampilleta, Arne Ludwig, Andreas D. Wieck, Pacome Armagnat, Thomas Kloss, Xavier Waintal, Tristan Meunier, and Christopher Bauerle. Unveiling the bosonic nature of an ultrashort few-electron pulse. 10 2016.

L. Saminadayar, D. C. Glattli, Y. Jin, and B. Etienne. Observation of the e/3 fractionally charged laughlin quasiparticle. *Physical Review Letters*, 79:2526–2529, 9 1997. ISSN 0031-9007. doi: 10.1103/PhysRevLett.79.2526. URL https://link.aps.org/doi/10.1103/PhysRevLett.79.2526.

Noam Schiller, Tomer Alkalay, Changki Hong, Vladimir Umansky, Moty Heiblum, Yuval Oreg, and Kyrylo Snizhko. Scaling tunnelling noise in the fractional quantum hall effect tells about renormalization and breakdown of chiral luttinger liquid, 3 2024.

W. Schottky. Über spontane stromschwankungen in verschiedenen elektrizitätsleitern. *Annalen der Physik*, 362:541–567, 1 1918. ISSN 0003-3804. doi: 10.1002/andp.19183622304.

Rabindranath Tagore. Baba pustak likhte rahte hai. URL https://youtu.be/uIGvsWIirBs. YouTube video.

Jeffrey C. Y. Teo and C. L. Kane. From luttinger liquid to non-abelian quantum hall states. *Physical Review B*, 89:085101, 2 2014. ISSN 1098-0121. doi: 10.1103/PhysRevB.89.085101.

D. J. Thouless, M. Kohmoto, M. P. Nightingale, and M. den Nijs. Quantized hall conductance in a two-dimensional periodic potential. *Physical Review Letters*, 49:405–408, 8 1982. ISSN 0031-9007. doi: 10.1103/PhysRevLett.49.405.

V. Umansky, M. Heiblum, Y. Levinson, J. Smet, J. Nübler, and M. Dolev. Mbe growth of ultra-low disorder 2deg with mobility exceeding 35×10^6 cm^2/v s. *Journal of Crystal Growth*, 311(7):1658–1661, 2009. doi: 10.1016/j.jcrysgro.2008.11.063.

B. J. van Wees, H. van Houten, C. W. J. Beenakker, J. G. Williamson, L. P. Kouwenhoven, D. van der Marel, and C. T. Foxon. Quantized conductance of point contacts in a two-dimensional electron gas. *Physical Review Letters*, 60:848–850, 2 1988. ISSN 0031-9007. doi: 10.1103/PhysRevLett.60.848.

Xavier Waintal, Michael Wimmer, Anton Akhmerov, Christoph Groth, Branislav K. Nikolic, Mathieu Istas, Tómas Örn Rosdahl, and Daniel Varjas. Computational quantum transport. *https://doi.org/10.48550/arXiv.2407.16257*, 7 2024.

Henok Weldeyesus, Taras Patlatiuk, Qianqian Chen, Christian P. Scheller, Amir Yacoby, Loren N. Pfeiffer, Ken W. West, and Dominik M. Zumbuhl. Edge state selective measurement of quantum hall dispersions. 7 2025. URL http://arxiv.org/abs/2507.07905.

X G Wen. *Quantum Field Theory of Many-Body Systems:From the Origin of Sound to an Origin of Light and Electrons: From the Origin of Sound to an Origin of Light and Electrons*. OUP Oxford, 2004. ISBN 9780198530947. URL https://books.google.co.il/books?id=llnlrfdR4YgC.

Xiao-Gang Wen. Edge transport properties of the fractional quantum hall states and weak-impurity scattering of a one-dimensional charge-density wave. *Physical Review B*, 44:5708, 9 1991. ISSN 0163-1829. doi: 10.1103/PhysRevB.44.5708. URL https://link.aps.org/doi/10.1103/PhysRevB.44.5708.

D A Wharam, T J Thornton, R Newbury, M Pepper, H Ahmed, J E F Frost, D G Hasko, D C Peacock, D A Ritchie, and G A C Jones. One-dimensional transport and the quantisation of the ballistic resistance. *Journal of Physics C: Solid State Physics*, 21:L209–L214, 3 1988. ISSN 0022-3719. doi: 10.1088/0022-3719/21/8/002.

F Wilczek and A Shapere. *Geometric Phases in Physics*, volume 5. WORLD SCIENTIFIC, 7 1989. ISBN 978-9971-5-0621-6. doi: 10.1142/0613.

R. Willett, J. P. Eisenstein, H. L. Störmer, D. C. Tsui, A. C. Gossard, and J. H. English. Observation of an even-denominator quantum number in the fractional quantum hall effect. *Physical Review Letters*, 59:1776–1779, 10 1987. ISSN 0031-9007. doi: 10.1103/PhysRevLett.59.1776.

Michihisa Yamamoto, Shintaro Takada, Christopher Bäuerle, Kenta Watanabe, Andreas D. Wieck, and Seigo Tarucha. Electrical control of a solid-state flying qubit. *Nature Nanotechnology*, 7:247–251, 4 2012. ISSN 1748-3387. doi: 10.1038/nnano.2012.28. URL https://www.nature.com/articles/nnano.2012.28.